UNIVERSIDADE FEDERAL DE MINAS GERAIS

Graduate Program in Chemical Engineering

Laboratory of Ceramic Materials

MASTERS DISSERTATION

Granulation and mechanic strength evaluation of nanomaterials with high potential as adsorbents and desiccants

Student: Gabriela Oliveira de Magalhães

Advisor: Prof. Dr. Wander Luiz Vasconcelos

Co-advisor: Daniela Cordeiro Leite Vasconcelos

Belo Horizonte, 2018

Magalhães, Gabriela Oliveira de.
M188g Granulation and mechanic strength evaluation of nanomaterials with high potential as adsorbents and desiccants [manuscrito] / Gabriela Oliveira de Magalhães. - 2018.
xvii, 88 f., enc.: il.

Orientador: Wander Luiz Vasconcelos.
Coorientador: Daniela Cordeiro Leite Vasconcelos

Dissertação (mestrado) - Universidade Federal de Minas Gerais, Escola de Engenharia.

Anexos: f. 74-88.

Bibliografia: f. 69-73.

1. Engenharia química - Teses. 2. Sílica - Teses. 3. Granulação - Teses. I. Vasconcelos, Wander Luiz. II. Vasconcelos, Daniela Cordeiro Leite. III. Universidade Federal de Minas Gerais. Escola de Engenharia. IV. Título.

CDU: 66.0(043)

UNIVERSIDADE FEDERAL DE MINAS GERAIS

Graduate Program in Chemical Engineering

Gabriela Oliveira de Magalhães

Granulation and mechanic strength evaluation of nanomaterials with high potential as adsorbents and desiccants.

Masters dissertation submitted in partial fulfilment of the requirements for the Masters degree in Chemical Engineering of the Federal University of Minas Gerais.

Area of concentration: Materials

Advisor: Prof. Dr. Wander Luiz Vasconcelos

Belo Horizonte

Escola de Engenharia da UFMG

2018

"A vitória mais bela que se pode alcançar é vencer-se a si mesmo."

Alípio de Oliveira (avô)

I dedicate this work to my dear father João Magalhães.

Acknowledgements

Immensurable appreciations to the people who helped and supported me bring this study into reality.

I would like to acknowledge the vital role of my family's support, namely parents, João and Rosângela, for being my inspiration and for always being by my side, to my brothers Júlio and Rafael, for giving me the emotional support, to my dear grandmother Iêda, for always praying for me, and finally to Isabel, for her patience and kindness helping me to finish this essay.

Additionally, I would like to express my profound gratitude to my advisor, Wander Luiz Vaconcelos, who let me join his research group and whose expertise and knowledge guided me through the challenges faced during this project.

I would also like to extend my appreciation to LMC members, especially to Daniela Vasconcelos and Jéssica Notório, for constant discussions and advices, and to Diana and Mr. Eurias, for helping me with the experimental part. I would like to thank all my laboratory colleagues, for their friendship. Moreover, thanks to Natanael (from Civil Laboratory at UFMG), who helped me with the mechanical analysis. In addition, I would to express my gratitude to Statoil, in special to Peter Derks for the support and advices, to Chemical Engineering Graduate Program of UFMG, for the opportunity to join the master program.

Finally, thanks to all my friends who supported me and cheered for me during this time.

List of Figures

List of Tables

Summary

Abstract

As an alternative to zeolites, mesoporous silica materials became spotlighted as competitive adsorbent and catalyst in different areas, due to their ordered and uniform porous structures and high surface area. In order to increase the availability of these materials, the need to granulate them becomes vital for efficient performance in industrial units. This study reports the production and characterization of clay-free granules of fumed silica and Santa Barbara Amorphous-15 (SBA-15) mesoporous silica, by applying extrusion-spheronisation technique. The traditional granulation process uses inorganic binders to ensure the mechanical strength of the final granules, but they fill the voids and pores of the material decreasing its adsorbance capacity. The main objective is to produce silica granules which can hold their features with the necessary mechanical strength and can be efficiently used as adsorbents and desiccants. The methodology suggested uses a methylcellulose polymer (methocel) as organic binder, which is removed after calcination. The effects of the granulation process, geometry, adsorbent capacity and mechanical performance were evaluated and discussed based on thermogravimetry, Fourier-transform infrared spectroscopy, nitrogen adsorption, water adsorption, axial and diametrical crushing tests, bulk crush test and microtomograph images. The granulation process was successfully achieved and produced millimetre sized pure granules of silica. Granules prepared with 20 % of methocel and calcinated at 800 °C had high mechanical strength, i.e. 8.3 MPa for SBA-15 mesoporous silica and 4.9 MPa for fumed silica (by axial crushing test). The surface area and pore volume of SBA-15 granules (calcinated at 800 °C) were around 392 m^2/g and 0.53 cm^3/g, respectively. The decrease of surface area, pore volume and water sorption capacity were observed for SBA-15 granules, calcinated at 800 °C, in comparison to the ones calcinated at 500°C. This can be explained by the fact that high calcination temperatures decrease the concentration of -OH groups on the surface of the material, reducing the number of micropores and enlarging some mesoporous pores.

Keywords: mesoporous materials, fumed silica, SBA-15, granulation, extrusion-spheronization

Resumo

Como uma alternativa às zeólitas, a sílica mesoporosa tornou-se um competidor em potencial como adsorvente e catalisador em diferentes áreas, devido principalmente à sua estrutura porosa uniforme e ordenada, e sua elevada área de superficial. Para aumentar a viabilidade dos materiais mesoporosos, a necessidade de granulação torna-se vital para uma eficiente aplicação nas unidades industriais. Este estudo relata a produção e caracterização de grânulos puros, sem a presença de argila, da sílica fumed e da sílica mesoporosa Santa Barbara Amorphou-15 (SBA-15), aplicando a técnica de extrusão-esferonização. O processo de granulação tradicional utiliza ligantes inorgânicos para garantir a resistência mecânica dos grânulos finais, todavia, esses ligantes preenchem muitas vezes os vazios e os poros do material diminuindo sua capacidade de adsorção. O objetivo principal é produzir grânulos puros de sílica que podem manter suas características, com uma apropriada resistência mecânica, para serem utilizados como adsorventes e dessecantes. A metodologia sugerida utiliza um metilcelulose (metocel) como ligante orgânico, que é removido após a calcinação. Os efeitos do processo de granulação, geometria, capacidade de adsorção e desempenho mecânico foram avaliados e discutidos com base nas análises de termogravimetria, espectroscopia do infravermelho, adsorção de nitrogênio, adsorção de água, testes de compressão axial e diametral, teste de compressao de leito e imagens de microtomografia. O processo de granulação foi realizado com sucesso, produzindo grânulos puros de sílica, em tamanho de milímetros. Os grânulos preparados com 20% em massa de methocel e calcinados a 800 °C apresentaram alta resistência mecânica, isto é, 8.3 MPa para sílica mesoporosa SBA-15 e 4,9 MPa para sílica fumed (pelo teste de compressão axial). A área superficial e o volume de poros dos grânulos de SBA-15 (calcinados a 800 °C) foram aproximadamente de 392 m2 / g e 0,53 cm^3 / g, respectivamente. Observou-se uma diminuição da área superficial, do volume de poros e da capacidade de adsorção de água para os grânulos de sílica mesoporosa SBA-15 calcinados a 800 °C, em comparação com os calcinados a 500 °C. Isso pode ser explicado pelo fato de que em temperaturas elevadas de calcinação, há uma redução da concentração de grupos -OH presentes na superfície do material, uma eliminação de alguns microporos e um crescimento de tamanho de alguns mesoporos.

Palavras-chave: materiais mesoporosos, silica fumed, SBA-15, granulação, extrusão-esferonização

1. INTRODUCTION AND MOTIVATION

The disclosure of mesoporous materials has gained world attention in different areas of chemistry and material science due to their exceptional characteristics such as large surface area (about ~3036 m^2 /g in mesoporous activated carbons), which is principally contributed from the presence of microporous and small and large mesoporous, high volume of uniform pore structure, narrow pore size distribution and considerable thermal and hydrothermal stability (1–3). Mesoporous silica has promising properties as adsorbents and catalysts and can be good competitors to commercial zeolites, in which the presence of micropores limits their catalytic performance in some applications.

Zeolites have many functions in natural oil and gas industries, including the use as desiccants to remove the water vapour from natural gas. Water vapour promotes the formation of hydrates and hereafter corrosion of equipment. The overall cost related to constant replacement and regeneration of zeolites is very high (4). As an alternative new materials have been developed. One promising material to replace or to add to zeolites is the highly ordered hexagonal mesoporous silica structure called Santa Barbara Amorphous-15 (SBA-15) with pore size between 2 and 30 nm (5). Due to their physicochemical properties and tunable pore structure, they are able to interact with atoms, ions and molecules on the surface and inside their nanoporous. SBA-15 has a structure with thermal, hydrothermal and mechanical stability. Recently, our group could develop different nanomaterials with potential application in gas treatment. Additionally, several promising studies are underway at the Laboratório de Materiais Cerâmicos at UFMG (6).

Mesoporous materials are known for their impressive properties. Nevertheless, in order to enhance their final properties and applications, one should have these materials granulated. Among many granulation processes, the extrusion-spheronization method has shown successful results shaping mesoporous silica into extrudates bodies (7). The objective in this dissertation was to granulate free powders of nanomaterials into rigid monoliths holding their characteristics properties and performance. This topic was accessed using different approaches, i.e. generating granules of nanomaterials without the use of inorganic binders, evaluating the mechanical strength on different granules' geometry, and finally by exploring the adsorption ability of mesoporous materials when they are conformed into pellets.

Therefore, free powders of fumed silica and mesoporous silica SBA-15 were shaped into spherical and cylindrical extrudates in order to carry out the measurements.

2. LITERATURE REVIEW

2.1. Overview of mesoporous materials

To start with, microporous and mesoporous materials play an important role in different industries, e.g. chemical, petrochemical, pharmaceutical, biotechnological, optics, electronic and gas separation industries. Due to their regular pore structure and high internal surface area, these materials are very suitable for catalysis, filtration and potentially in gas separation (8). The efficiency of structured adsorbents and catalysts is based on their porous structure and different parameters, namely mass and transfer properties, gas diffusion kinetics, pressure drop across the adsorbent, mechanical and chemical stability (9).

According to the literature, porous materials can be classified into three categories according to their pore diameter, i.e. microporous (pore diameters smaller than 2 nm), mesoporous (pore diameters between 2 nm and 50 nm) and macroporous (pore diameter is greater than 50 nm) (10). Even though all porous materials could be referred as nanoporous, because the size of their pores ranges between 1 to 100 nm, usually in literature, the term nanoporous material refers to mesoporous or/and microporous materials. In addition, although some structures would have pores lengths larger than 50 nm, if the pore width is in mesopore range, the material is still classified as mesoporous. Figure 1 illustrates pore size distribution of some porous materials.

Microporous and mesoporous materials have high volume of porosity and large surface area, making them excellent adsorbents, catalysts, ion-exchange agents and mesoreactors. The pores can have different shapes such as spherical (a), cylindrical (e), ink-bottle (c) or slit type (f) as shown in Figure 2 and they can be arranged in specific structures, e.g. layered, hexagonal or cubic (11) as shown in Figure 3. The concentration of “closed” pores influences the final mechanical strength, apparent density and thermal conductivity of the material, while “open” pores have a large impact on the sorption process.

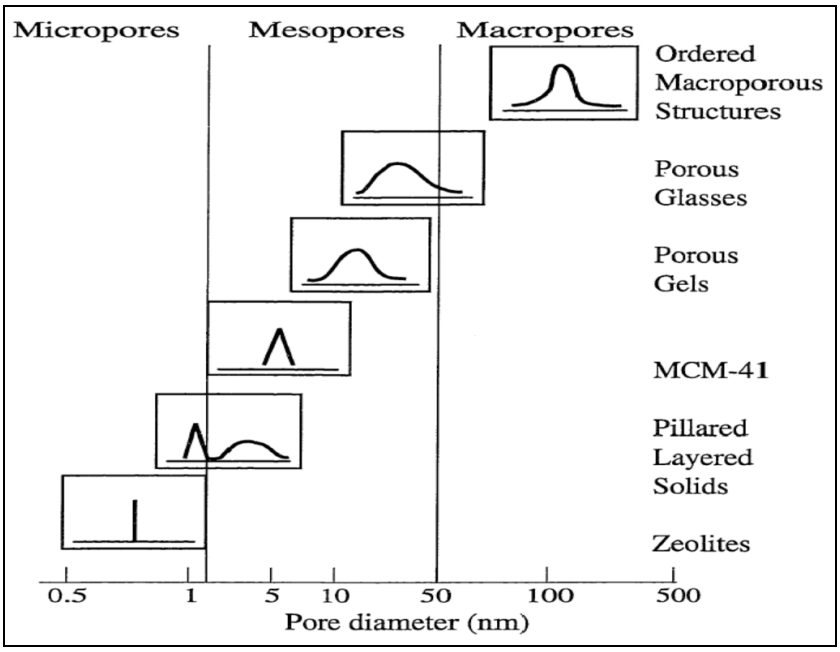

Figure 1: Schematic pore size distribution of some porous materials (11)**.**

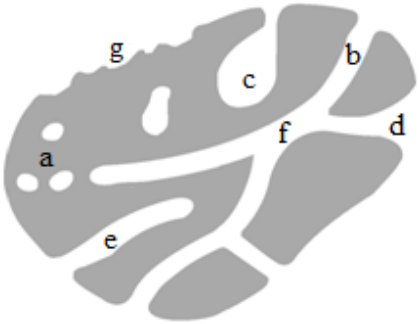

Figure 2: A schematic cross-section of a porous solid material, adapted from Avnir (12)**, which illustrates some closed pores (a), open pores (b-f-d), blind pores (c, e) and roughness (g).**

Figure 3: Different pore structures of mesoporous materials, MCM-50 (layered), MCM-41 (hexagonal) and MCM-48 (Cubic) (11)**.**

Mesoporous materials contain voids, channels and interstices which allow liquid and gas molecules to pass through them. The filling pore's mechanisms depend on the pore shape, adsorptive properties and adsorbent-adsorbate interactions, resulting in monolayer adsorption, in multilayer adsorption and capillary condensation (Figure 4). In the first case, it assumes that all the adsorbed molecules are adhered onto the surface layer of the adsorbent, while in a multilayer adsorption not all the adsorbed molecules are in a direct contact with the surface layer. Regarding capillarity condensation, the gas condensates into a liquid state in the residual pores where the pore pressure p is smaller than saturation pressure p_o. This capillarity phenomenon generally occurs after multilayer adsorption has occurred, and for mesoporous materials it can be identified by the presence of hysteresis in adsorption-desorption isotherms of gas when the temperature is lower than the critical hysteresis temperature (10,13).

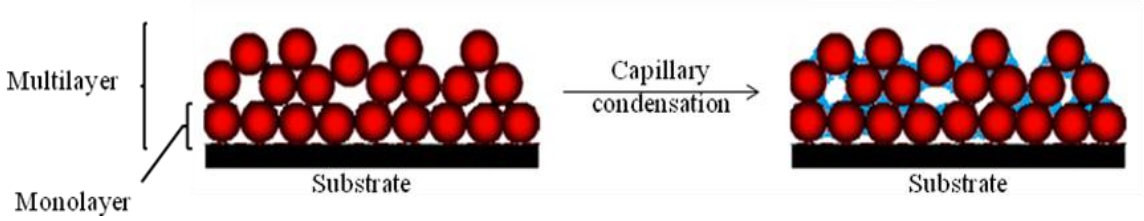

Figure 4: Scheme portraying capillary condensation.

Mesoporous materials can be produced in an ordered or disordered structure and they will yield different properties and applications. Besides the fact that mesoporous materials have large pore volume, good interconnectivity, high surface area, they hold thermal stability, in which they can be calcinated up to 850 °C, depending on their composition. Some of mesoporous materials have been tested in solar cells (14–16). It is believed that the thermal stability is related to the thickness of the pore walls, i.e. the thicker the higher stability. In addition, controlling the pore structure order improves the thermal conductivity of the mesoporous materials.

The continuous discoveries in this field, increases the availability of surfactants and sol-gel chemistry. Mesoporous materials can be synthesized with a wide range of compositions and with a highly controllable pore geometry and narrow pore size distribution, resulting in different structural properties. The nature of precursor, temperature and pH values of the media are other key factors for the synthesis. Moreover, the introduction of heteroatoms, such as Cu, Zn, Al, B, Fe, Cr and Ti, and organic functional groups, e.g. amides or amines, inside of mesoporous materials increases their functional applications (17). The majority of

mesoporous materials are consisted of oxides, e.g. SiO_2, Al_2O_3, TiO_2, ZnO_2, Fe_2O_3 ZrO_2, Nb_2O_5, Ta_2O_5, SnO_2, combinations of metal oxides, for example $SiAlO_{3.5}$, $SiTiO_4$, $ZrTiO_4$, Al_2TiO_5 and ZrW_2O_8 (18), and also can be made of carbon (19,20). Most commonly, the ordered mesoporous materials are produced by a liquid-crystal template mechanism, in which the oxide material forms inorganic walls around long array ordered surfactant micelles (8). This method is known as soft-templating mechanism, and the organic template molecules are named as structure-directing agents (SDAs). Alternatively, there is another mechanism called hard-templating. In this case, a preformed mesoporous template is used to grow another type of mesoporous material inside it. This method is often used for mesoporous carbon synthesis (21). Via calcination in both methods, the template is removed leaving the mesoporous network. These two mechanisms are also known as endotemplating and exotemplating, respectively and are illustrated in Figure 5.

These initial findings generated great interest and effort worldwide. It resulted in tremendous expansion of knowledge and skills with many additional discoveries that established a new knowledge area of ordered mesoporous materials.

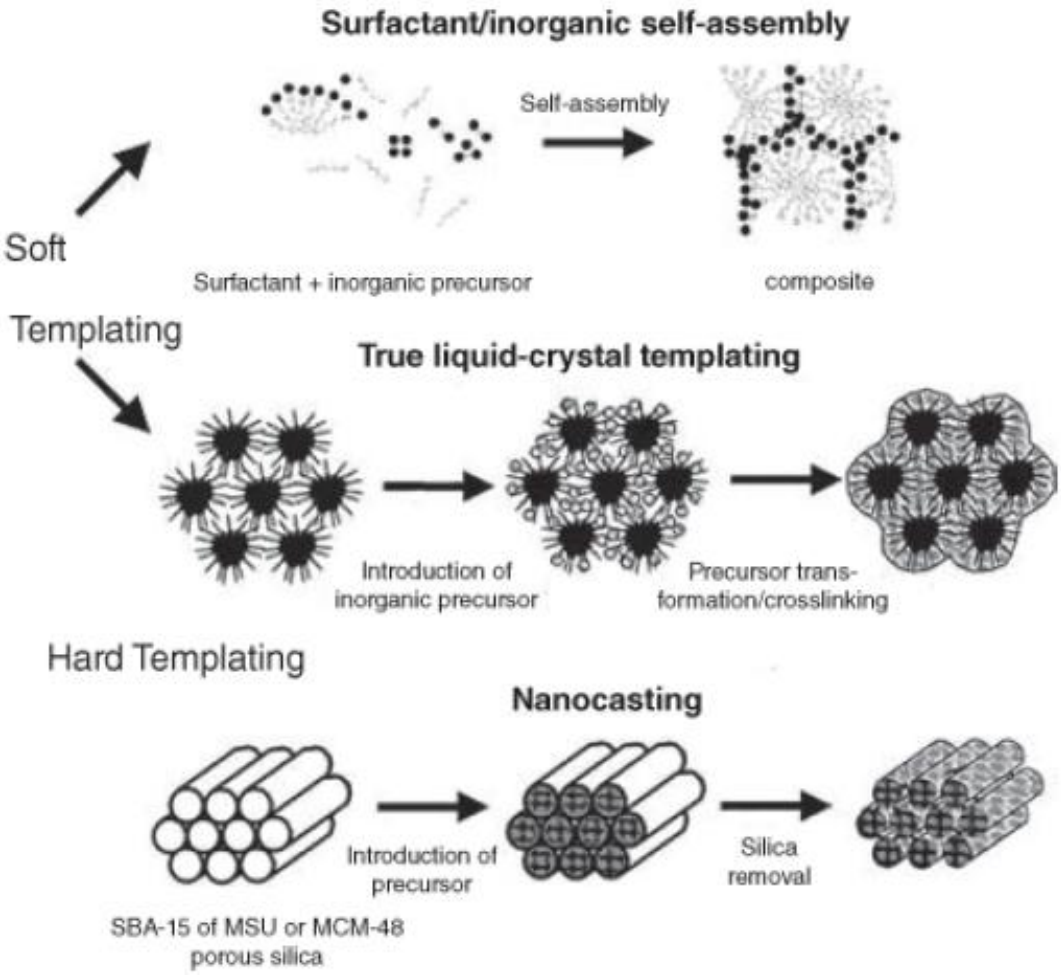

Figure 5: Schematic synthesis for ordered mesoporous materials: soft-templating and hard-templating methods (22)**.**

2.2. Zeolites

The term zeolite was first used in 1756 by Cronstedt while describing the material stilbite, a mineral which released water upon heating, but could recover it reversibly at low temperatures (23). Therefore, this material was named "zeolites", which derives from the greek words zein (to boil) and lithos (stone) (24). Nowadays, zeolites represent a large family of crystalline solids.

Zeolites are the most representative microporous materials with many applications as adsorbents and catalysts in industrial processes and in control of environmental pollution. Their surface negatively charged promotes an easier proton and cation-exchange, making the zeolites extensively used in cracking crude oil process in petrochemical industry.

Additionally, zeolites are also employed as water-softeners removing heavy metal cations from groundwater and radioactive Cs^{+} and Sr^{2+} cations from liquid nuclear. With a previous functionalization with some cations, e.g. Ag^{+} and Pb^{2+}, zeolites can absorb toxic anions, e.g. CrO_4^{2-} and radioactive iodide, and organic pollutants (25). Due to their ability to select molecules by size and shape, zeolites are called "molecular sieves" and they are widely used in (bio)chemical industries and gas separation process. Moreover, zeolites have been employed in dehydration of natural gas processing, as they are a good water adsorbent.

Furthermore, zeolites are composed of regular arrays of uniform channels, similar to the format of honeycomb structure, with pores dimensions smaller than 1.3 nm and a surface area bigger than 1000 m^2/g (26). Zeolites have a crystalline aluminosilicates with three-dimensional framework structures and normally, single organic molecules are used as a template for their synthesis. Common zeolites are constructed by four-connected covalent bonds in a 3D tetrahedron (TO_4) network, where T is replaced by Si or Al atoms (8). One can observe the basic chemical structure of zeolites in Figure 6. The pore size can be varied by changing surfactants, auxiliary chemicals and the synthesis procedure. Therefore, each pore system can be designed to perform specific task.

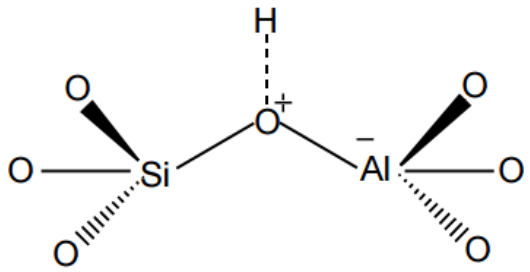

Figure 6: Generic structure of a zeolites, cations of silicon Si^{+4} and aluminium Al^{+3} are tetrahedrally coordinated by four oxygen anions (O^{-2}) forming a three dimensional framework structure (24,27)**.**

Natural zeolites arose from chemical reactions between volcanic ashes and alkaline salt water and they are often found out in mountainous regions with volcanic history, e.g. Caucasus, Balkans and Himalayas. Nevertheless, it is rare to find natural zeolites pure, as they are usually contaminated by other minerals, elements or other zeolites. Thus, most zeolites used commercially are produced synthetically. Along the improvement of technology and techniques, a better control of synthesis parameters was achieved, e.g. polarity, acidity, composition, purity, and hydrophobicity of the structure. Nowadays, there are about 40 different types of natural zeolites identified, and around another 190 have been artificially

synthesised (28). Some of the common natural zeolites are: analcime, chabazite, natrolite, and stilbite, illustrated in Figure 7. In 2015, according to U.S. Geological Survey (USGS) (29), the world production of natural zeolites was estimated to be 2.8 million metric tons, with China accounting for more than 70 percent of production. Unfortunately, large tonnages of natural zeolites are typically used in low-value applications, especially in constructions and downhole cement by the drilling industry.

Figure 7: Pictures of common natural zeolites. A - Natrolite, frequent in India; B - Analcime, in Scotland; C - Chabazite, in Scotland; D - Stilbite (exceptionally coloured) typical in India (30)**.**

The purity and uniform micropore structure are essential for many vital applications. Some advantages of zeolites over conventional catalysts are the less or lack corrosion, lack of disposal problems, easiness to set-up and high thermostability (31). Nowadays, zeolites are synthesized on large scale with different structure properties. Zeolites are known as "molecular sieves", due to their ability to select molecules based on their sizes. The dimensions of the channels control the maximum size of the molecular or ionic species that can pass through the pores. However, as a consequence of the micropore sizes, the applications of zeolites are limited, especially when it involves transfer and conversion of

macromolecules (22) or when it involves irreversible adsorption or the blockage of the channels by secondary products that reduce the material life (31). Therefore, the development of mesoporous materials has become an important branch in high-performance of the catalysis and adsorbents, notably the mesoporous silica materials (MSNs).

2.3. Mesoporous silicas

New strategies, techniques and technologies have increased the popularity and the use of mesoporous silica materials (MSNs) in different field applications, including adsorption, separation, catalysis, sensors, drug delivery and optical devices. This worldwide success is due to their outstanding intrinsic features; such as high specific surface area (about 1600 m^2/g) combined with a well-defined pore structure, good biocompatibility and easy surface modification. Moreover, the porosity can be as high as 80% of their total volume. Different applications can be achieved by modifying structural properties (pore size) and surface properties (surface polarity), during the synthesis. Notably, the disclosure of mesoporous silicas' properties extended to the mesopore range the concept of molecular sieving, which was limited before to zeolites (11,32–34).

In 1992, Mobil Oil Corporation (Mobil) scientists first reported the successful synthesis of ordered pore arrays of mesoporous silica materials (M41S series), combing knowledge of sol-gel science and surfactant science. Long-chain cationic surfactants were used as a soft template to synthesize ordered mesoporous aluminiosilicate materials. The removal of template by calcination gave rise to mesoporosity. The structure of organic template molecules, also called as structure-directing agent (SDA), is critical for the formation and stability of mesostructure (8,22).

In other words, the synthesis of mesoporous silicate materials can be explained by a liquid-crystal 'templating' (LCT) mechanism (a sol-gel route), in which hydrolysis and condensation reactions of the silicate material occur, allowing the formation of colloidal solution (sol) and subsequently the formation of the three-dimensional network (gel), building inorganic walls between ordered micelles of the surfactants (22). The porosity is afterwards created by removing the template by calcination.

The reactions conditions are dependent of the nature of silicon source, which can be nonmolecular or molecular and can be catalysed by acid or basic mediums. There are two classes for nonmolecular silica source: salt (such as chlorides, nitrates, sulphates) and alkoxide. TMOS and TEOS are the most convenient and efficient tetrafunctional silicon alkoxide precursors in synthesis of mesoporous silicates. With equations, it is possible to exemplify their polymerization in mainly two steps. First, the formation of silanol group by hydrolysis of silicon alkoxide precursors in water, represented in equation 2.1. Then, the silanol groups undergo self-condensation or condensation with another alkoxysilane molecule producing siloxane bonds (Si-O-Si) and alcohol (equation 2.2) or water (equation 2.3). It is important to take note that each step is strongly depended on pH, temperature, concentration, co-solvent effects, nature and concentration of catalysts (35).

$$\equiv Si - OR + H_2O \xrightarrow{\text{hydrolysis}} \equiv Si - OH + ROH \qquad \text{(Eq. 2.1)}$$

$$\equiv Si - OR + HO - Si \equiv \longrightarrow \equiv Si - O - Si \equiv + ROH \qquad \text{(Eq. 2.2)}$$

$$\equiv Si - OH + HO - Si \equiv \longrightarrow \equiv Si - O - Si \equiv + H_2O \qquad \text{(Eq. 2.3)}$$

In addition, based on Mobile Crystalline Materials (MCM), three different pore structures for ordered mesoporous materials have been identified: lamellar (MCM-50), hexagonal (MCM-41) and cubic (MCM-48). A hexagonal pore structure of MSNs possesses highly regular arrays of uniform-sized channels and it has its synthesis illustrated in Figure 8.

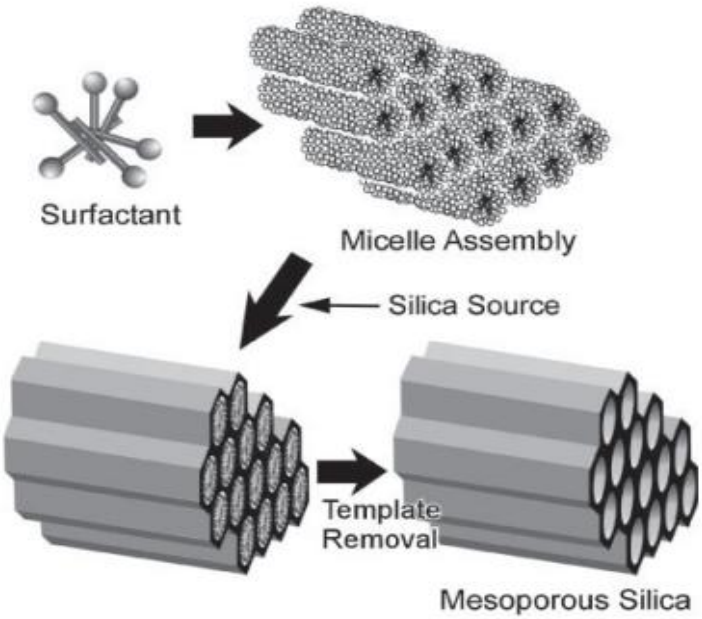

Figure 8: Illustration of the synthetic procedure for typical mesoporous silica with hexagonal pore structure (17)**.**

The success of the final pore structure and morphology is based on the right selection of precursors, surfactants, auxiliary chemicals and reaction conditions during the synthesis and post-synthesis functionalization. For example, the pore structure mainly depends on the strength, size and self-assembly of hydrophobic tail and hydrophilic head parts of the surfactants (Figure 9). In low concentration, surfactants obtain micelles, while at high surfactant concentration, a liquid-crystal phase is generated in order to decrease the system entropy (Figure 10). The threshold concentration to form isotropic micelles is called the critical micellization concentration (CMC). Therefore, precise control of micellar construction is one of the main challenges, because it is necessary to find out the optimized pH, ionic strength of the solution, surfactant effects and temperature.

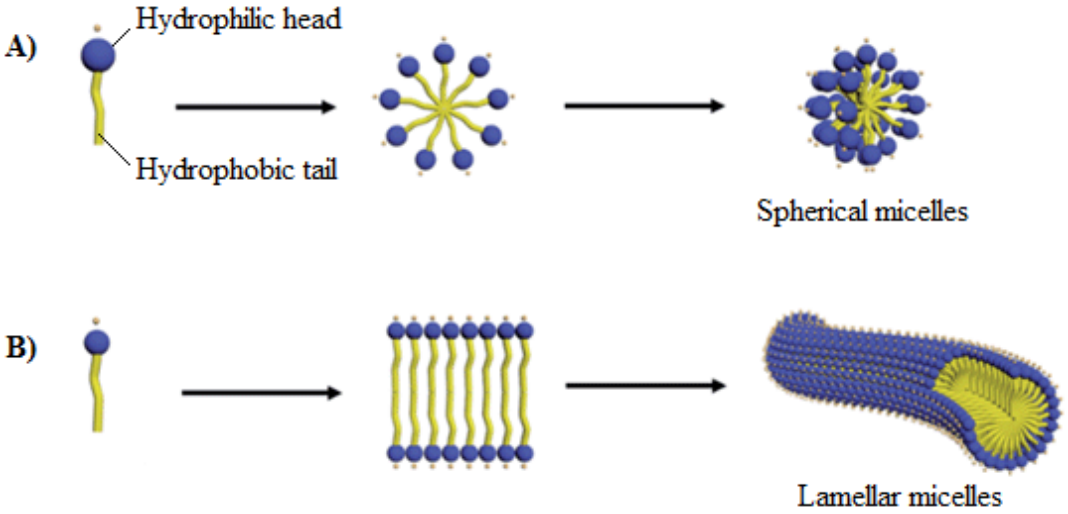

Figure 9: Picture adapted of the growth of micelles (36)**. A) Surfactants with large head polar group promote large surface curvature, generating spherical aggregates. B) Surfactants with large lipophilic tail and relatively small head group generate small surface curvature, creating lamellar micelles.**

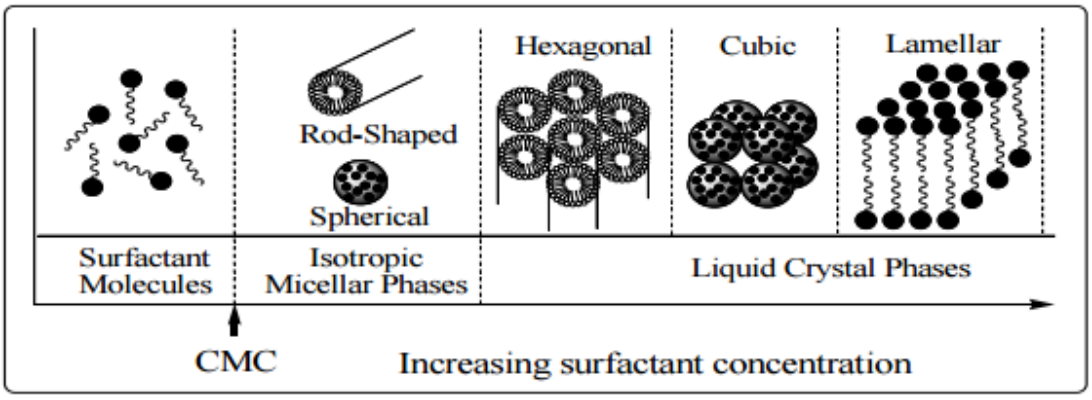

Figure 10: Schematic of phase sequence of surfactant-water system, in which CMC means critical micellization concentration.

Another attractive advantage of MSNs is the high density of silanol groups (-Si-OH) around external surface. Opposed to zeolites, not all SiO_4 units in mesoporous silicates are four-connected, which generates a hydrophilic surface with higher presence of hydroxyl groups (22). These hydroxyls contribute to water adsorption and can be modified by loading a wide range of organic functional groups inside of mesoporous materials. The introduction of amines group inside the material, increases the adsorption volume of CO_2 in gas separation process (37). Pure mesoporous silica presents higher capacity of adsorption at high pressures (38).

2.3.1. SBA-15 silica

Due to the research growth focused on mesoporous molecular sieves, another significant family of mesoporous silica was produced, in 1998, named Santa Barbara Amorphous (SBA), which has exclusive and important properties. The most known is the SBA-15, which has an uniform hexagonal array of pores like Mobile Crystalline Materials-41 (MCM-41), but with larger pore size from 4.6 to 30 nm (39). The tunable pore diameters favour the functionalization of further groups that enhance and optimize SBA's catalytic activity. The organic functional groups may adjust the hydrophilic-hydrophobic character of silica surface to improve sorbent chemical selectivity for specific atoms, molecules or ions (40), not only on the surface but also inside the nanoporous.

Despite size pores, the amorphous pore walls are thicker (about 3.1 to 6.4 nm), which gives SBA-15 thermal, mechanical and chemical resistance properties. In addition, its high internal surface area around 400 to 900 m^2/g makes SBA-15 a well suited material for different applications (41), e.g. catalysis, drug delivery and CO_2 adsorption. Figure 11 was extracted and adapted from the literature (42) showing the Transmission Electron Microscopy (TEM) analysis of SBA-15 material, in which it is highlighted its cylindrical and uniform pores, ordered in an hexagonal structure, with mean pore diameter of approximately 10 nm. Additionally, in Figure 11-b, one can observe nanochannels (microporous), called coronas which are responsible for interconnectivity between the cylindrical pores.

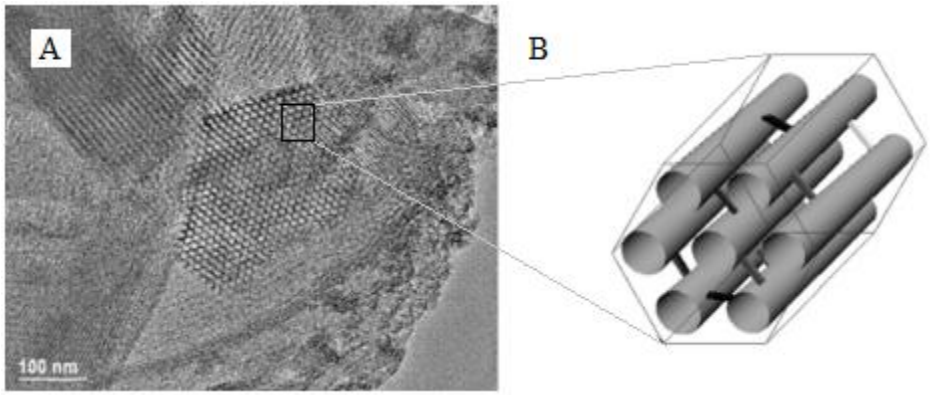

Figure 11: SBA-15. (A) Transmission Electron Microscopy (TEM) image of Mesoporous nanostructured SBA-15, showing the ordered porous structure of SBA-15. (B) Schematic model for cylindrical pores arranged in an hexagonal structure interconnected by nanochannels (42)**.**

SBA-15 is generally obtained by hydrothermal synthesis, which is synthesized in acidic media in the presence of triblock copolymer surfactant, e.g. Poly(ethylene glycol)-block-poly(propylene glycol)-block-poly(ethylene glycol) (Pluronic P123, $OE_{20}OP_{70}OE_{20}$), and silicon source, normally tetraethyl orthosilicate (TEOS, $Si(OC_2H_5)_4$) or tetramethyl orthosilicate (TMOS, $Si(OCH_3)_4$. The solution is mixed for 2-22 h at 40 °C and then heated up to 80-130 °C for 24-72h. Finally, the product is filtrated, dried and calcinated at 550 °C to remove the surfactant (template) (6)

The final product is mesoporous silica with parallel pores and highly ordered hexagonal arrangement. The microporous surround mesopores are created by the penetration of the hydrophobic surfactant chain in the silica walls (43). The combination of micro and mesoporosity is responsible for the high surface area of SBA-15.

Among various mesoporous material, SBA-15 is a very suitable candidate for applications in treatments of gases containing water vapour, due to its high hydrothermal stability, which therefore characterises SBA-15 material as "water-tolerant adsorbents" (44).

2.4. Fumed silica

Fumed silica is also known as synthetic amorphous or pyrogenic (fumed) silica, because it is generally produced in a flame via pyrolysis of silicon tetrachloride or from quartz sand vaporized in the range of 1100 °C to 3000 ° C electric arc. First, molecules of SiO_2 are formed when silicon tetrachloride is burned in the flame of hydrogen and oxygen (Equation 2.4).

$$SiCl_4 + 2H_2 + O_2 \rightarrow SiO_2 + 4HCl \qquad \text{(Eq. 2.4)}$$

Then, SiO_2 molecules increase size until forming molten spheres of fumed silica, called primary particles. Collisions and fusion between them result in a formation of three-dimensional chainlike secondary particles named aggregate. Even though the flame temperature decreases, the particle collisions continue, thus, the secondary particles are aggregated building up the tertiary particles, known as agglomerates. Those agglomerates are therefore collected. The production of fumed silica is illustrated in Figure 12. As the result of the brief residence time in the flame, there is a lack of time to build up a crystalline structure of silica. The final product is a fluffy white powder of amorphous silica structure,

characterized by nanoparticles size, low bulk density, spherical morphology, large surface area (50-380 m^2/g) and high purity. Primary particle size can vary from 7 to 40 nm, according to the ratio of the reactants and setting system. Similar to other mesoporous silicas, fumed silicas are characterized by the strong presence of silanol groups (Si-OH) around the surface (approximately density of 1-4 $SiOH/nm^2$). It is possible to modify the surface properties, replacing these silanol groups or by altering the flame process (45,46).

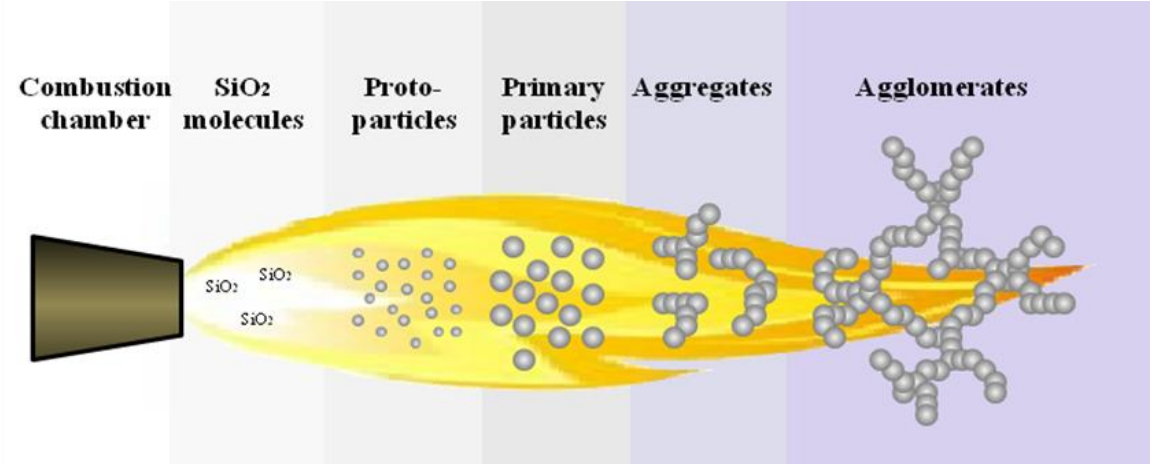

Figure 12: Illustration of production of fumed silica the flame.

Commercially, there are three main classes available of fumed silicas: hydrophilic silicas, hydrophobic silicas and mixed oxides. Hydrophilic silicas are produced during the normal flame hydrolysis of silicon tetrachloride as described before. Some of their applicability allows the reinforcement silicone elastomers, thickening of non-polar liquids and rheology control of greases and lubricants. They also have excellent insulation properties, even at high temperatures, making them very popular in high technology fields, e.g. electronics and optical fibers industries. Hydrophobic silicas are produced through a chemical treatment of hydrophilic silica with organosilanes. Moreover, they are characterized by a low moisture adsorption, excellent dispersibility and the ability to control the rheology behaviour even for polar systems. At the same, mixed oxides are obtained when a volatile compound such as aluminium chloride or boron chloride is added to the flame process. They are often used as catalyst supports, rheology control and they have strong thickening effect in polar media (47).

Fumed silicas are applied in different fields, due to their chemistry and physical properties. Some general applications of fumed silica, extracted from the *Handbook of Fillers For Plastics* (46), can be founded in Table 1

Table 1: General applications of fumed silica.

Function	Application area
Reinforcement	Natural and synthetic rubber, polymers and plastics
Thixotrope	Unsaturated polyester, epoxy and PVC dispersion resins
Thickening	Paints, inks, coatings, wire cable jacketing
Rheology control	Cosmetics, pharmaceuticals, toothpaste
Matting	Paints, coatings, PVC and plastics
Dry-up liquids	Flavour, fragrances, foods, cosmetics
Filler	Plastics
Plate-out	Thermoplastics
Anti-blocking	Foods, plastics, resins
Abrasive and polishing agent	Toothpaste

Despite advantages listed above, it is often difficult to deal, store and transport fumed silica material, due to its fine particles. To overcome some of these difficulties, one could granulate these fine powders, which would then improve the flow and minimized the fine losses.

2.5. Granulation

As important as all the outstanding properties of mesoporous materials previously described, it is important to work with them in formats of granules or pellets to increase its adsorbent's efficiency. Due to small grain size and low density, part of powdered raw material may be lost during the air pollutant treatment process, being difficult to be recovered (7).

Granulation technology has been widely used by different industries, such as chemical, pharmaceutical, coal, mining, metallurgy, ceramic, and agrochemical. There are several reasons that make agglomeration process particularly appropriate to industry. It is very important to produce useful structural forms, decrease dust generation, provide easier handling, reduce caking and lump formation, increase bulk density, control porosity, prevent the segregation of the constituents of powders mix and enhance the material's ultimate utility. In addition, granulation is responsible for improving flowability, uniformity and increasing mechanic properties of the raw materials.

According to Perry's Chemical Engineer Handbook (48), "size enlargement is any process whereby small particles are agglomerated, compacted, or otherwise brought together into larger, relatively permanent masses in which the original particles can still be distinguished".

In granulation, process variables and formulation properties interact to give the final particle design. Clays, plasticisers and surfactants can be added to the formulation to help achieve a homogeneous and plastic wet mass. Moreover, additional binders can improve mechanical strength of final granules, facilitating transportation and the application of these materials in industry units. The final particle size and porosity are dependent on operations conditions and formulation. (49).

Basically, there are two main types of granulation technologies: dry granulation and wet granulation (Figure 13).

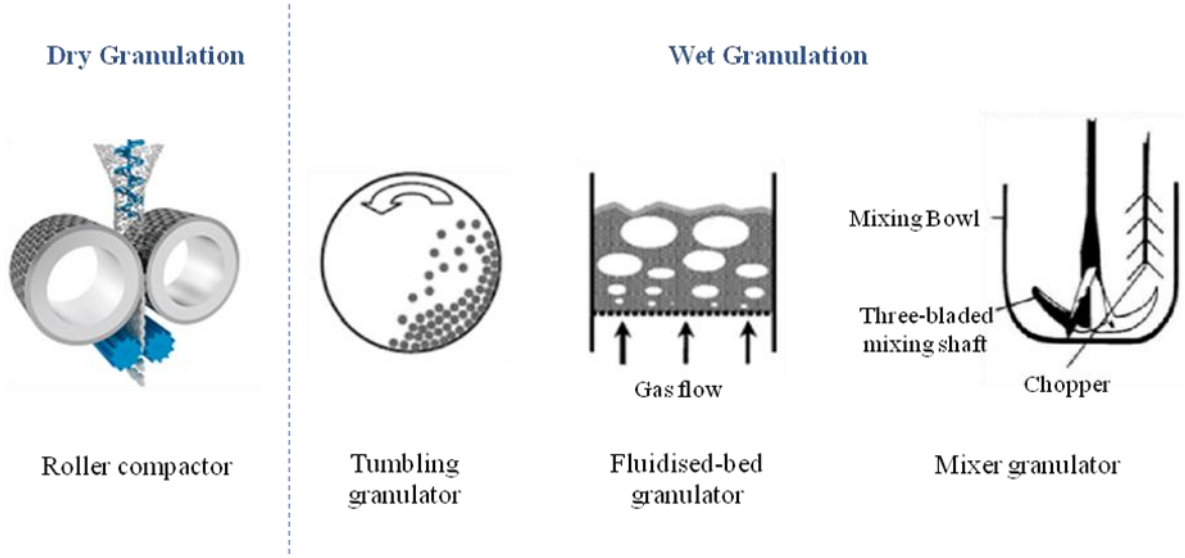

Figure 13: Typical granulation methods (49,50)**.**

2.5.1. Dry granulation

In the dry granulation process, the granules are normally produced without adding a liquid solution. First, powder particles are intensively mixed and then they are aggregated under high pressure to promote interparticle bonds, resulting in a considerable size enlargement. These compacted bodies are called briquettes, flakes or ribbons. Common equipments used in dry granulation are roller compactors, cone mills and extruders. This method is often applied to increase bulk density of powders and decrease segregation of the constituents. Dry granulators are especially employed by pharmaceutical industries while manufacturing drugs that are sensitive to heat and moisture. Furthermore, dry granulation is a continuous process and requires low cost equipment and maintenance (51).

2.5.2. Wet granulation

The wet granulation process is performed by adding a liquid (with or without binder) onto the particles to form interparticle bonds while they are mixed to promote liquid dispersion and granule growth. Moreover, the liquid binds the particles together by a combination of capillary and viscous forces until more stronger and permanent bonds are formed by subsequent drying and sintering (52). The general mechanism involves three phases. The first involves wetting, nucleation and binder distribution, the second is related to the consolidation and growth of the granules and the third phase involves attrition and breakage. Commercially, there are different types of wet-agitated granulation equipments and they are classified by the way the material is agitated, such as tumbling drum granulators, fluidized-bed granulators and mixer granulators.

Tumbling granulators include discs, drums or pans. Basically, the particles are set in motion by the combination of gravity and centrifugal forces while a liquid is sprayed onto the tumbling bed via nozzles or distributor pipe system. The average product granule size is between 2 to 20 mm, making them ideal to produce high density balls or pellets, being extensively used in mineral processing and fertilizer granulation (53). Even though tumbling granulators are more sensitive to operating conditions than the others granulators, they are able to operate with continuous feed and sometimes with very high recycle ratios.

Fluidised bed granulation involves several processes like wetting, drying, size enlargement, shaping and homogenisation or separation into a single step, at the same equipment, by using high heat and mass transfer. In these granulators, the particles are set in motion by air, rather than by mechanical agitation. A packed bed is flowed upwards from below at a certain gas velocity, causing a solid/fluid mixture to behave as a fluid. Normally, the granulation of particles in fluidised beds involves different kinetic equations, many variables and correlations such as a correlation between Reynolds number and Archimedes number, which are derived from a force balance (lifting force, gravity force, drag force and accelerating force) around a floating single particle. The equipment can be designed in different ways with different complexities. Additionally, this technique is applied for coating particles or production of spherical granules by single-stage or multi-stage batch processes in different fields, e.g. pharmaceutics, fertilisers, mineral processing and special chemicals. The process is controlled by moisture content of the bed, i.e. high moisture content defluidises the bed

whereas at low moisture the agglomeration does not occur. One characteristic of this equipment is that the granules obtained are generally more porous than those obtained from others. The main disadvantages of this granulation are related to the high operating costs involved for air handling and the poor operation with fine cohesive powders (49,54).

Mixer granulators or high shear granulators use impeller to vigorously agitate the powder (between 100 to 1500 rpm) on either a vertical or horizontal axis and produce high-density granules. In high shear granulators, it is common to have an additional small impeller, called a chopper, which rotates at higher speeds (around 1500 rpm) and it is responsible for increasing the homogeneity and reducing the fines of the granulation. They have a wide range of applications in pharmaceutical, agrochemical and detergent industries, due to their ability to handle difficult feedstocks, including viscous binder fluids and fine cohesive powders. Some advantages over other granulators are related to the ability to process wet and sticky materials and to spread high viscous binders (55).

Concerning the wet granulation process, the final granules properties are affected by the different operating conditions, i.e. varying from system to system and from material to material used. Due to this reason, several parameters have to be set experimentally, which include:

- The amount of binder added (liquid to solid ratio), i.e. normally a larger amount of liquid results in a larger average granule size, respecting a critical saturation level to avoid over-wetting.
- The method of binder addition, i.e. the binder can be added by pouring, melting and spraying.
- The agitation speed determines the amount of energy input into the system based on how the granules will respond, i.e. the increase in impact energy, results in more deformation of the granules.
- The process time, i.e. the granule size distribution usually becomes narrower afterwards, however increasing process time thus not always result in larger granules.
- The choice of binder is related to its properties (viscosity, surface tension and contact angle) and may affect the granule-granule interactions, consequently the behaviour of the granulation system.

- Amount of material to be granulated.

Despite these parameters, other operating conditions such as temperature, humidity and even feedstock loading can affect the final properties (55). Based on this, it is hard to generalize the relationship between feed material properties and granulation behaviour.

2.5.3. Extrusion-spheronisation

Another granulation technique widely adopted is the extrusion-spheronisation method, which has the objective to achieve spherical or cylindrical pellets, commonly termed extrudates. This process requires at least four unit operations (56): (i) combination, (ii) extrusion, (iii) spheronisation and (iv) drying. Combination step involves the preparation of wet mass with plasticity and deformation characteristics, i.e. adding the liquid phase into the dry powder mixture under agitation. In the extrusion step, wet mass is compressed through a single die (or multi-holed screen) and shaped into cylinders extrudates, as illustrated in Figure 14. It is known that an axial screw extruder produces a more dense material than to a radial screw extruder. Concerning extrusion stage, it is required a pre intensive mixing of water-solids to ensure homogeneity and consistency, avoiding further phase migration. Regards to the spheronization stage, the extrudates bodies are broken up and then get rounded by the motion of a rotating friction plate. Finally, the granules are dried to remove the granulation liquid. The final granules should have low friability and good integrity. When optimised, the process yields dense and quite spherical granules with narrow particle size distribution. In some cases, if the final desired product shape is a cylindrical pellet, then the spheronisation step is omitted and the extrudates are cut into small rods with the required size (57). Extrusion-spheronisation granulation is often employed by pharmaceutical, polymers, fertilizers and herbicides industries.

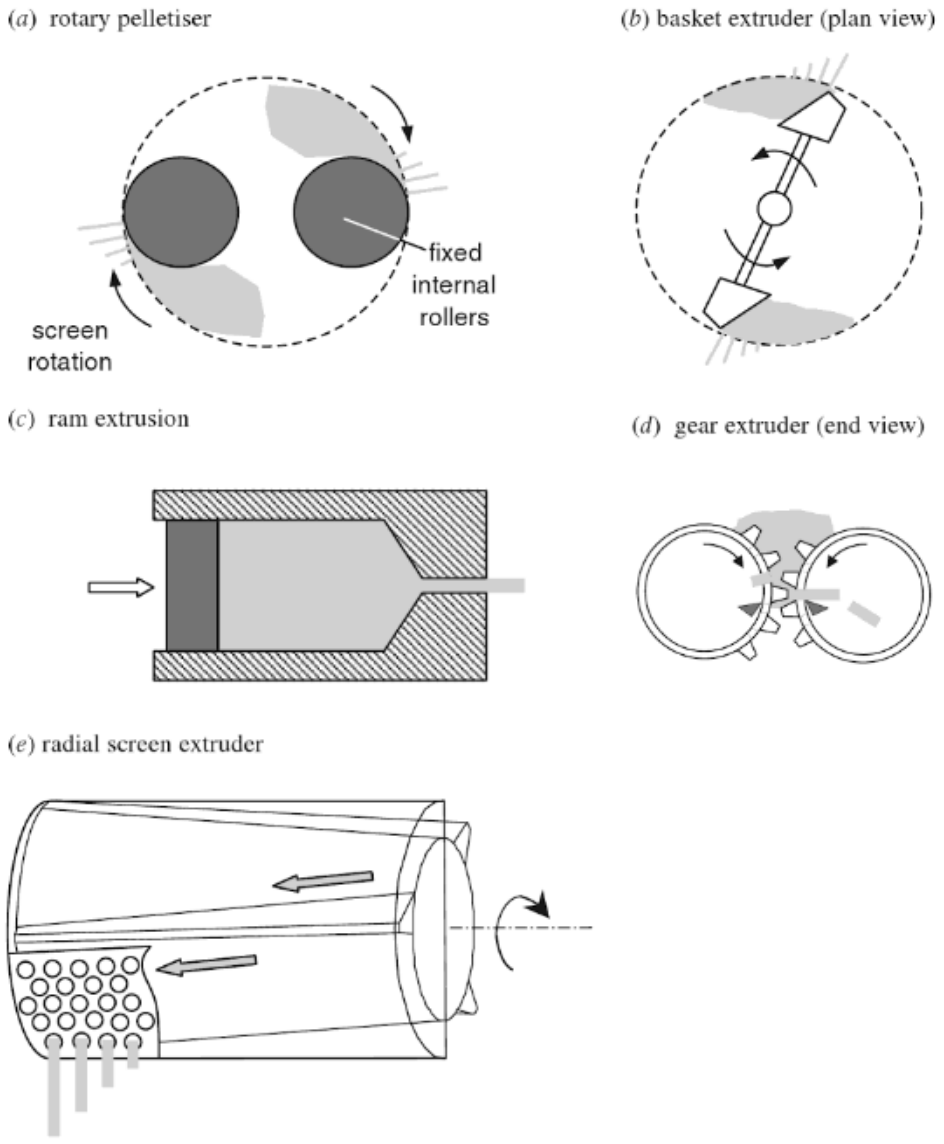

Figure 14: Action of different extruders (57)**.**

The focus of this study is the ram extruder (explored in that), which tends to produce more dense material than the others, since it requires a higher extrusion pressure. The quality of the extrudate bodies are highly dependent on extrusion velocity and die geometry. The die length *L* / die diameter *D* ratio is an important parameter to avoid fractures and get smooth surface. Low values of L/D, produces rough and loosely bound extrudate due to the low extrusion pressure applied, while higher L/D can produce well-bound extrudates with better densification (56). Figure 15 illustrates some of the effects promoted by extrusion velocity (V) and die length (L) in ram extrusion. At low extrusion velocities, it is increased the likelihood of liquid-phase migration, because the liquid has time to redistribute, whereas at

higher velocities can promote surface fracture. Short dies (small L/D) require lower extrusion pressures, but promote fractures on the extrudate surface. Large L/D values often generate smooth and rigid extrudates, but the process requires higher extrusion pressures. The extrusion process has a direct impact on the subsequent spheronisation stage, e.g. extrusion defects, liquid-phase migration and extrudate homogeneity (57).

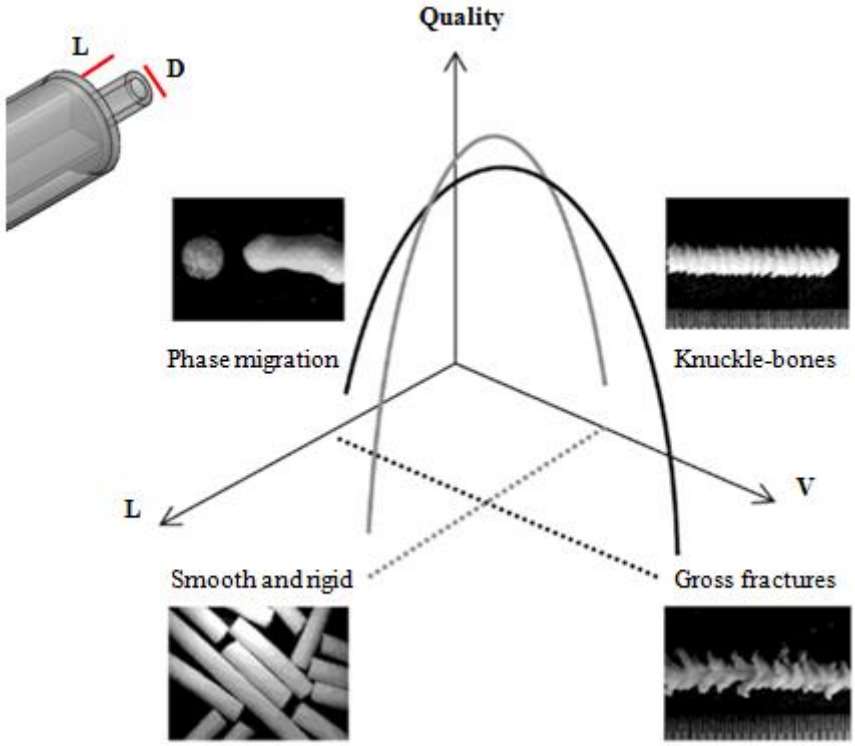

Figure 15: Effects of operating conditions of extrusion prior to spheronisation, which L is the die length and V the extrusion velocity (57).

For a successful spheronisation, the extrudates body have to hold enough mechanical strength to retain their own structure, but at the same time be brittle enough to break into short rods on the spheroniser plate. They should have enough plasticity in order to transform rods into spheres in good quality, and they have to be non-adhesive to avoid that the spheres agglomerate or stick to the spheroniser.

There are different spheronisation mechanisms explaining the transformation of cylindrical rods into spheres, and some of them are illustrated in Figure 16. In 1985, Rowe (58) describes that the short rods with lengths approximately equal to their diameters have their edges rounded off and their overall shape changes from rounded rods to dumb-bells to ellipsoids and are finally transformed into spheres. In 1993, Baert (59) proposed a different mechanism

which includes a second breakage step (D). The dumb-bell is twisted and broken in two pieces at the weakest point (in the centre) and the both parts are rounded into spheres overtime (C – E). In 2007, Liew's mechanism considered the effect of agglomeration of fines (60). Fine particles from previous breakage step get attached to the pellets surface and form a spherical pellet (ii - iv). Recently, in 2013, Krueger explained another mechanism that the long extrudates bodies break into different particle sizes while generating fine fractions (61).

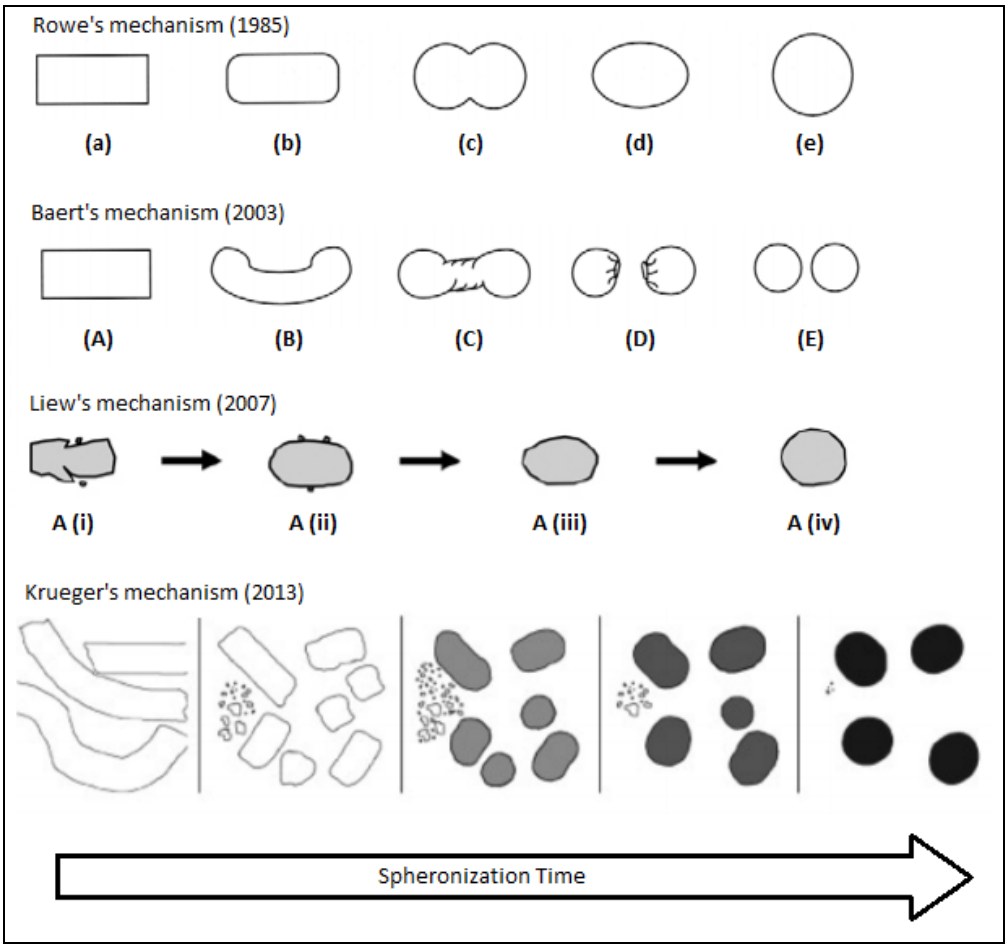

Figure 16: Spheronization mechanism according to Rowe (1985), Baert (2003), Liew (2007) and Krueger (2013) (60–63)**.**

All particles get deformed due to the collisions and smaller particles get milled down and agglomerate on bigger particles. It is difficult to predict spheronisation performance simply from monitoring the extrudate quality, as not all smooth and well-compacted extrudates give good spheres.

Figure 17 shows a schematic spheroniser, which features a friction plate rotating at a controlled speed inside cylindrical bowl. The splitting and subsequent rounding of cylindrical

extrudates on the spheroniser plate is a random process. The frictional base plate has a characteristic grooved surface to increase friction. The two most common geometric patterns of grooves are cross-hatched (Figure 18-a) and radial patter (Figure 18-a), but the first are more used due to its more economical production (64).

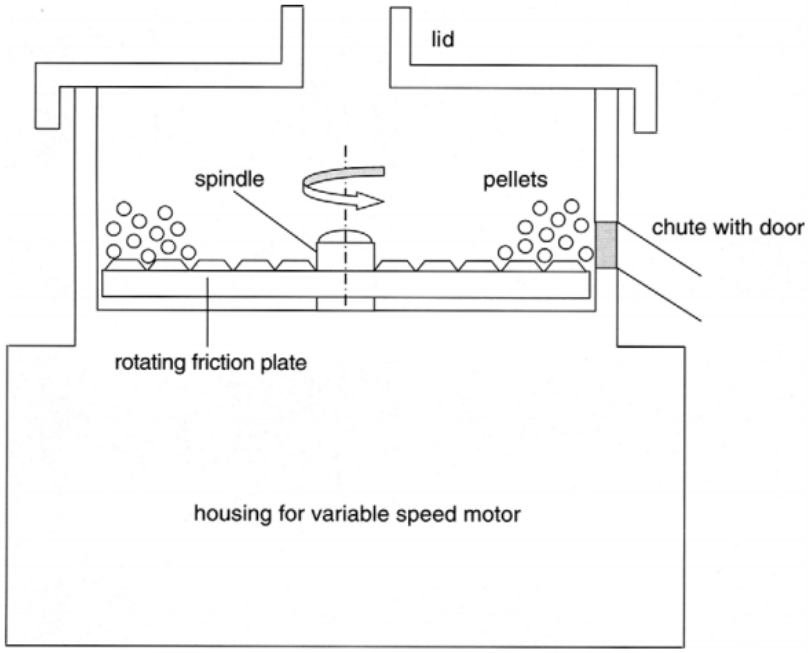

Figure 17: Schematic of spheroniser (57)**.**

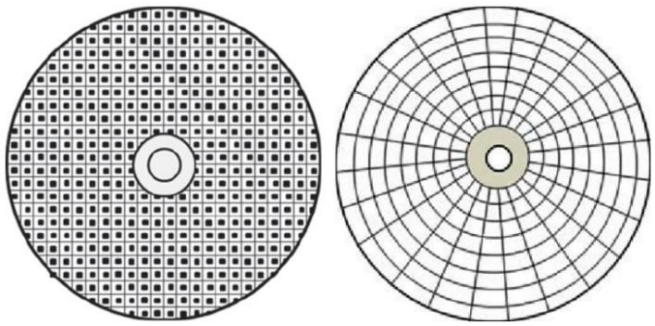

Figure 18: Diagrams depicting frictional base plates employed in the spheroniser; (A) cross-hatched pattern, and (B) radial pattern (64)**.**

It is important to keep in mind that a formulation which operates satisfactory in one extruder type, will not necessary work properly on the others, neither that will be successfully spheronised. Concerning the extrusion-spheronisation process, water is the most common liquid phase used. It acts as glitant (lubricator) during extrusion stage. To reduce surface defects and power consumption, surfactants and lubricants can be also added. Based on this,

one important parameter in developing formulations is the solids/liquid ratio, which affects in the rheology of the wet mass. Low liquid contents require higher force to extrude and generate noticeable fractions of dust. Furthermore, the drier extrudates might not be able to deform properly in the spheroniser afterwards. On the other hand, high liquid contents result in an over-wetted mass when extruded, which can cause uncontrolled agglomeration in the spheroniser. The moisture content of the extrudate ultimately has the greatest effect of the pellet size and shape, regardless of the type of granulator used (57).

To summarize, agglomeration through extrusion and spheronisation has been used as successful techniques for manufacturing pellets. A valuable contribution by shaping mesoporous silica into cylindrical extrudates, by compounding with organic and inorganic binders, via wet granulation process, was presented by Choi (7) and Chandrasekar (1). However, due the use of inorganic or organic binders to granulize the mesoporous materials, pores of the mesoporous materials may be occluded. Unfortunately, in this case, the porous characteristic of the absorbent may be degraded (7). Organic granulation binders are commonly used in pharmaceutical industry, because they yield good binding properties, provide plasticity and mechanical strengths to the green bodies extrudates without addition of inorganic binder. The most popular binders for extrusion include methylcellulose, hydroxipropyl methylcellulose, poly(ethylene oxide), poly(vinyl alcohol), sodium carboxymethylcellulose, alginates and ethyl cellulose (65). In addition, a potential binder is the Methocel A4M, which is a medium viscous methylcellulose, soluble in water, offers binding and adhesive properties as well hardness, and it has been used successfully in wet granulation process (66).

Therefore, it is necessary to select the best binder and control the granulation process parameters to develop the preparation method for granular silica, which is able to hold the superior mesoporous characteristics and can be efficiently used for air pollutant treatment processes.

3. OBJECTIVES

3.1. Main objectives

The purpose of this work was to study and to develop a granulation process for nanomaterials with high potential adsorptive and desiccant properties. Finally, another main objective was to evaluate the mechanical strength of the final granules.

3.2. Specific objectives

The first part of this work consisted of developing a granulation process of fumed silica and then applying the method to SBA-15 mesoporous silica. The following objectives were respected:

- Elaborate a granulation process for nanomaterials.
- Design an extruder and a spheroniser equipments, capable of working with a small amount of material to produce cylinder pellets and spherical granules; Additionally, set up operational conditions (L/D ratio of extruder equipment, liquid content, speed of rotational friction plate in the spheroniser equipment);
- Obtain cylindrical rods and spherical granules of fumed silica and SBA-15 silica, via wet granulation and applying the extrusion-spheroniser technique.

The second part involved the mechanical and adsorption capacity evaluation of the granules, obtained from the first stage. The listed aims below were respected:

- Evaluate the mechanical strength through uniaxial compression test, Brazilian test, bulk crush strength test;
- Design an apparatus to perform the bulk crush strength test, adapted from ASTM D7084-04 standard;
- Analyse the effect of the granule's geometry, the calcination temperature and the amount of binder on mechanical strength and adsorption performance.

4. MATERIALS AND METHODS

4.1. Materials

This section relates to the description of the materials used in the development of this work. The Fumed silica was manufactured by Aldrich Chemical Company while methocel A4M was manufactured by Dow Chemical Company. Additionally, the SBA-15 silica was synthesized in LMC/UFMG laboratory (6).

4.2. Preparation of fumed silica and SBA-15 granules

Due to the absence of the conventional granulators equipments in the LMC Laboratory to work with small amount of material (maximum 5 g), it was necessary to develop new apparatus for granulation. In order to obtain uniform granules, it was necessary to use the conventional wet granulation method and applying extrusion-spheronisation techniques, to produce cylindrical pellets and spherical granules of fumed silica and SBA-15 silica.

The methodology was divided into two stages. The first step was to prepare the spherical and cylindrical pellets for the different formulations of fumed silica. Then, the SBA-15 extrudates were prepared as well.

Moreover, the steps involved in the preparation of cylindrical extrudates (A) and spherical particles (B) are schematically shown in Figure 19. The final cylindrical extrudates were obtained by mixing intensively the dry components (powder + binder) and then by adding a minimum amount of deionized water into the dry mixture (approximately 3.6 mL of water / 1 g of fumed silica and approximately 4 mL of water / 1 g of SBA-15) until the uniform and consistent paste was formed; this can be seen in Figure 20. The Methocel A4M was used as plasticiser (to enhance the viscosity of the paste during extrusion), as the organic binder (to increase the mechanical strength of green bodies), and as macropore builder. Opposed to inorganic binders, which remain in the structure, the methocel, when used as an organic binder, is removed through the calcination process after the powdered silica has been granulized, thus, working also as a macropore builder. The wet paste was then transferred into

an adapted metal screw extruder (Figure 21), with 3.8 mm diameter circular cross sectional die. Based on Figure 15, different die lengths to diameter ratios (*L/D*) were experimentally tested until smooth cylindrical extrudates were produce. The optimal die length encountered was 128 mm. Furthermore, the extrusion was achieved by constantly moving the screw manually, to obtain smooth extrudates. Extrudates of 6 mm length were cut by a sharp nickel coated knife, as illustrated in Figure 22. The wet extrudates were dried at 60 °C.

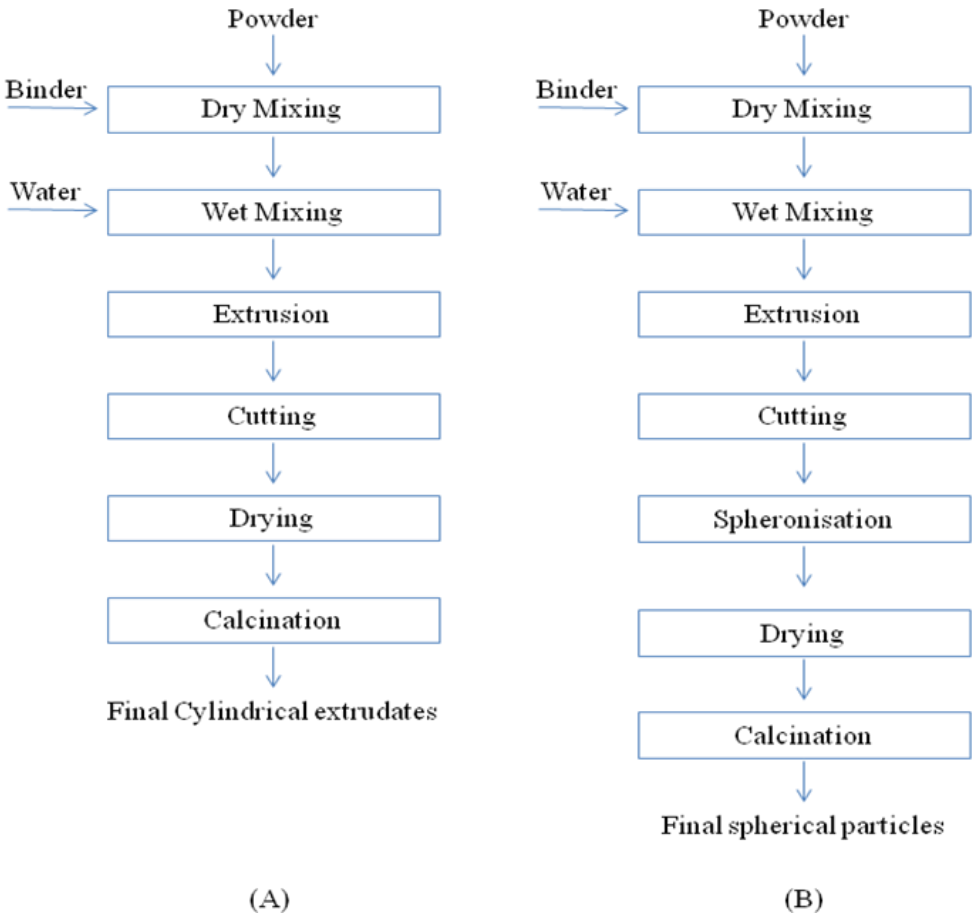

Figure 19: Steps involved in the granulation process.

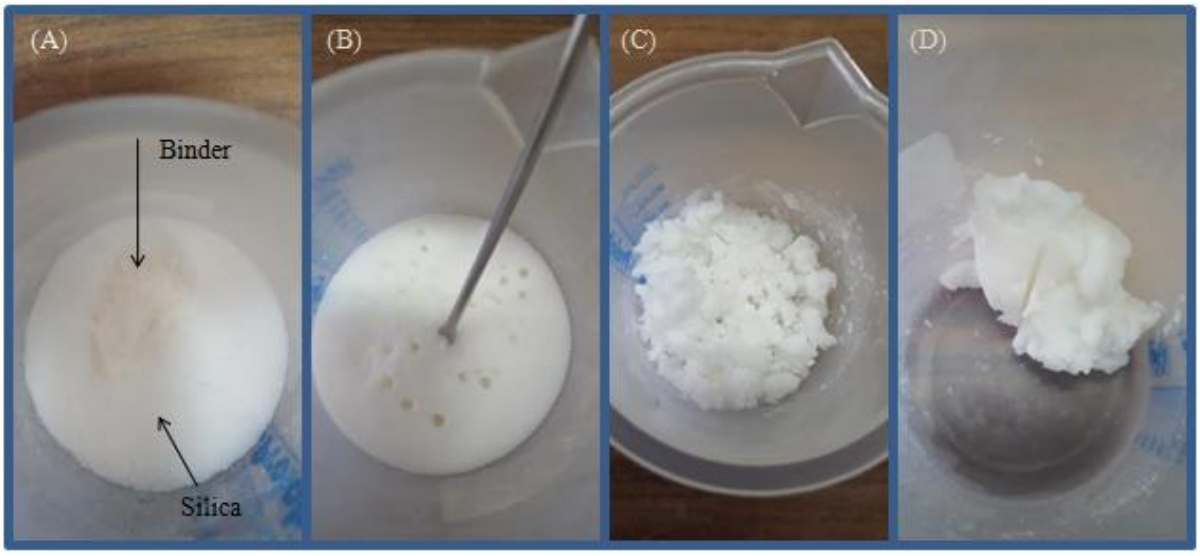

Figure 20: Wet mass preparation.

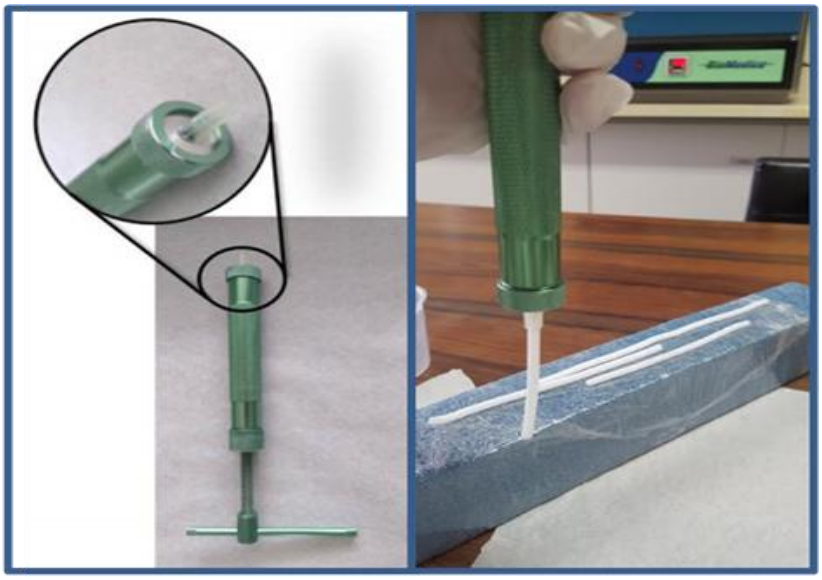

Figure 21: Metal screw extruder used to produce cylindrical extrudates.

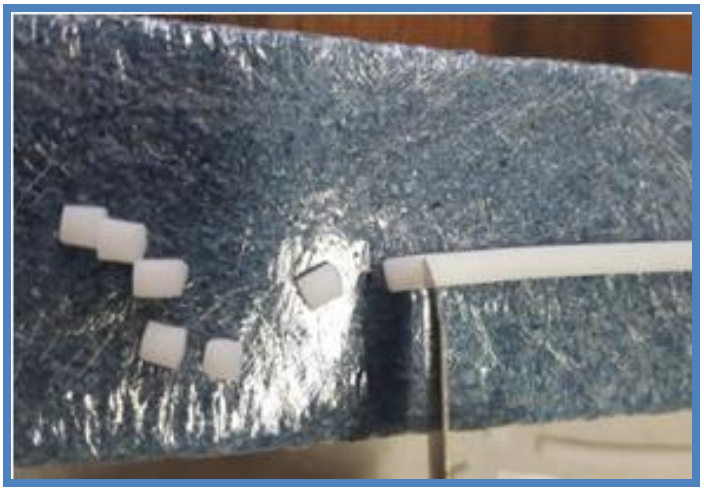

Figure 22: Wet extrudates in the sectioning procedure.

Due to lack of binder after calcination process, the increase of mechanical strength was performed increasing the calcination temperature. The heat treatment was first performed at 500 °C and at 800 °C for fumed silica samples to confirm the increase of the resistance with the increase of temperature, and then, the SBA-15 sample was calcinated at 800 °C. In order to avoid the elimination of the mesoporous inside the material and maintain their integrity, the heat program was calculated based on the time that the samples would spend at and above 500°C. Therefore, for the same rate of 1 °C/min, the sample at 800 °C remained only 1 h to compensate the time to reach 800 °C and then return to 500 °C. Thus, the fumed silica extrudates were calcinated at a rate of 1 °C/min from room temperature to 500 °C for 6 h or 800 °C for 1 h, and the SBA-15 cylindrical extrudates were calcinated at a rate of 1 °C/min from room temperature to 800 °C for 1 h.

Concerning the spheronisation process, the spheroniser equipment was built in the LMC Laboratory. It consists of a fixed aluminum bowl of 900 mL, with a spinning friction plate (covered by rough iron sandpaper number p36) at the base and attached to a motor. One can observe the spheroniser design in Figure 23. The final spheres granules of fumed silica were obtained following the same procedure as the cylindrical extrudates until the extrudate body was produced. Thus, the cylindrical extrudates were cut (4 mm length) and put in the spheroniser for approximately 10 minutes at low speed (adjusted from 6.5 to 14.3 revolutions / second), to avoid breakage of the granules.

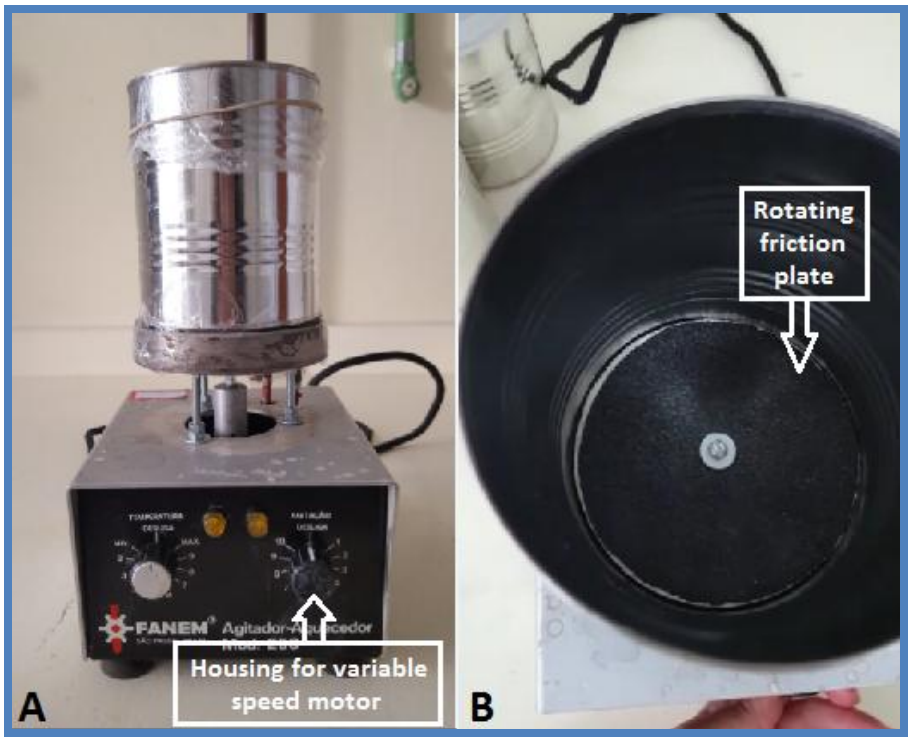

Figure 23: Photographs of front view (A) and top view (B) of the spheroniser built in the LMC Laboratory.

The names of the samples produced in this work are listed in Table 2.

Table 2: Designations adopted for the samples in this work.

Sample	Silica Source	Binder content (%wt)	Final body shape	Calcination Temperature (°C)
FS_20%A4M_800°C	Fumed Silica	20	Cylindrical	800
FS_15%A4M_800°C	Fumed Silica	15	Cylindrical	800
FS_20%A4M_500°C	Fumed Silica	20	Cylindrical	500
FS-sph_20%A4M_800°C	Fumed Silica	20	Spherical	800
FS-sph_15%A4M_800°C	Fumed Silica	15	Spherical	800
SBA15_20%A4M_800°C	SBA-15 silica	20	Cylindrical	800

4.3. Characterisation

In order to determine the specific surface area and specific pore volume, it was necessary to perform N_2 adsorption tests (Quantachrome Autosorb 1C) on the samples (refered to TABLE

2). The absence of methocel in the final compositions, after calcination process, was demonstrated by Fourier Transform Infrared Spectroscopy (FTIR – Perkin Elmer Frontier) and by thermogravimetry analysis. In addition, 2D images by the SkyScan 1172 microtomograph were obtained to analyse the morphology of the samples. Moreover, Image-J computation software was used to evaluate qualitatively the geometry and sphericity of the granules. In order to investigate the mechanical properties of the granules, it was performed diametrical and axial compression tests using the SkyScan 1172 microtomograph and bulk crushing test using the Instron - 5900 equipment.

4.3.1. Thermogravimetry

The TG and DTG analysis were performed with a Perkin-Elmer STA-6000. These tests were conducted using a heating rate of 5 °C/min and under synthetic air flow (20 mL/min).

4.3.2. Fourier Transform Infrared Spectroscopy (FTIR)

FTIR samples were prepared as pellets with KBr and examined in a Perkin-Elmer Frontier spectrometer. The spectra were taken from 4000 cm^{-1} to 400 cm^{-1}, with a resolution of 2 cm^{-1} and 64 scans. The collected spectra were normalized using the band at 1080 cm^{-1} as reference.

4.4. Performance evaluation

4.4.1. Mechanical strength measurements

Axial and diametrical (Brazilian test) compression tests were performed for different compositions of fumed silica extrudates and SBA-15 silica extrudates. The tests were performed using the SkyScan 1172 microtomograph.

To perform the bulk crush strength test it was necessary to build an apparatus to perform the test. In an attempt to work with a small amount of material, the support size described in the ASTM D7084-04 standard was reduced by half. Figure 24 shows the measurements of the

support used to measure the volume of particles to be tested, while Figure 25 portrays the newly designed apparatus.

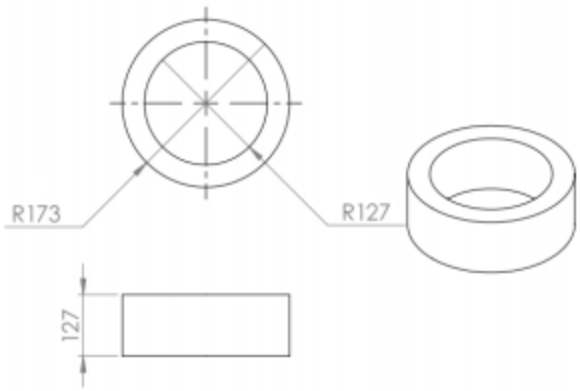

Figure 24: Description of the support measurements in mm.

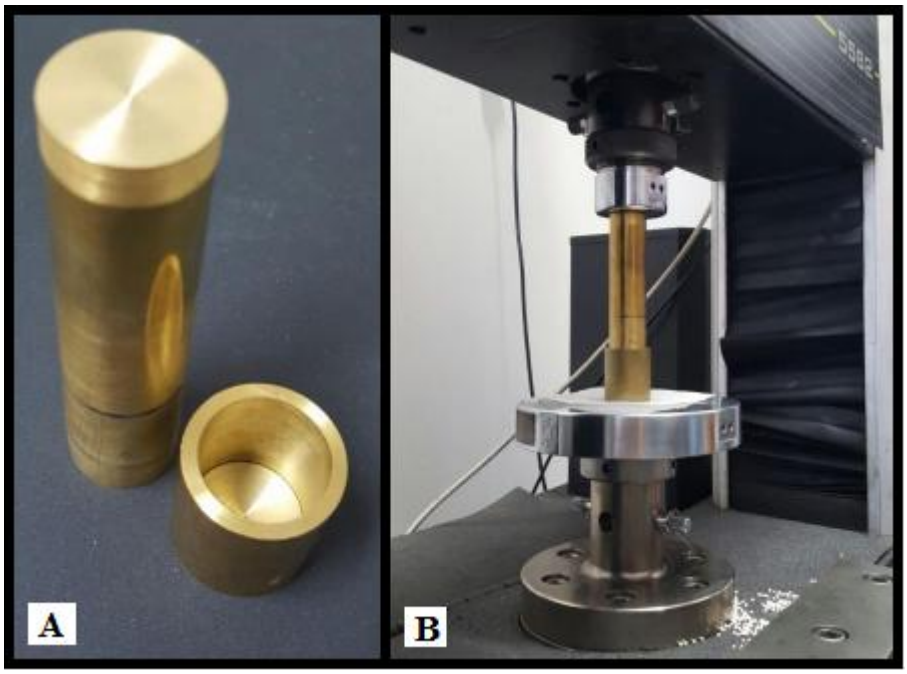

Figure 25: (A) Apparatus built to perform bulk crush strength test in conventional compression equipments. (B) Illustration of the bulk crush strength test.

4.4.2. Nitrogen adsorption

The nitrogen adsorption tests were carried out in a Micromeritics ASAP 2020 apparatus (at room temperature of 25 °C), using SBA-15 silica samples previously degassed at 200 °C for up to 24 hours under vacuum. The specific surface area and the pore size distribution were obtained by

applying the BET method and the NLDFT method, respectively. The fumed silica was not analysed because it is an amorphous samples.

4.4.3. Water sorption

The water sorption performance tests were carried out in the Micromeritics ASAP 2020 apparatus, using SBA-15 silica samples (previously degassed at 200 °C for 2 h under vacuum). The fumed silica was not analysed because it is an amorphous samples.

5. RESULTS AND DISCUSSION

Pastes prepared in this work were carried out by mixing commercial fumed silica or SBA-15 silica, previous synthesised in LMC Laboratory, with different amounts of methocel A4M (15 and 20 % wt) and with addition of a minimum amount of water. As expected, the addition of water to the powder mixture was a critical step in the extrusion process. To obtain a firm extrudate body with a smooth surface, the necessary water was added by trial and error. Approximately, for each batch of fumed silica paste, it was used 1g of fumed silica powder per 3.6 mL of deionized water. Regarding the SBA-15 mesoporous silica samples, a slight higher amount of water was added to the mixture, i.e. approximately 4 mL of water / 1g of SBA-15 silica.

Figure 26 shows two failed attempts, when the added water was less than the necessary to get a good paste consistence, thus, illustrating the vital role of having the right water content. These attempts were carried out by mixing fumed silica powder with 20 % wt of methocel. In the first case (A), it is possible to see the breakage of the extrudate body while it was being cut into rods. In the second case (B), the surface of the green body extrudates were irregular. Both cases were rejected due to the presence of cracks on the green bodies, which increase their fragility.

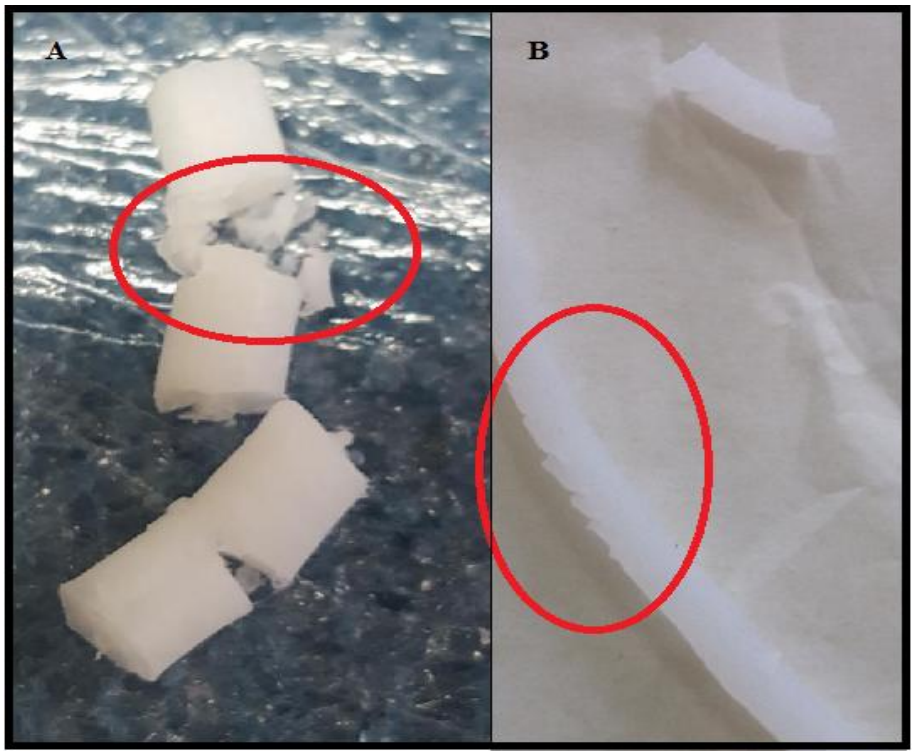

Figure 26: Fragile fumed silica rods (lacking water content).

On other hand, one can observe a successful amount of water added to the dry mixture of fumed silica powder with 20 % wt of methocel in Figure 27. The rods' surface appeared regular and smooth, without major defects. Therefore, the key to achieve a good consistence paste is to constantly stir the mixture while the water is added gradually.

Figure 27: Desirable fumed silica paste.

In addition, another improvement to the extrusion process was to increase the methocel content, consequently increasing the viscosity of the paste, due to its high viscosity (3000-5500 mPa.s, 2% in H_2O °C (67)). Therefore, the paste became thicker and harder to extrude. Methocel A4M proved to be very effective in providing strength to the green body, which offered binding and adhesive properties, during wet granulation process. Thus, the fumed silica green body extrudates obtained the desired consistency and plasticity, as illustrated in Figure 28, and then, were cut into small pellets (approximately 4 cm length).

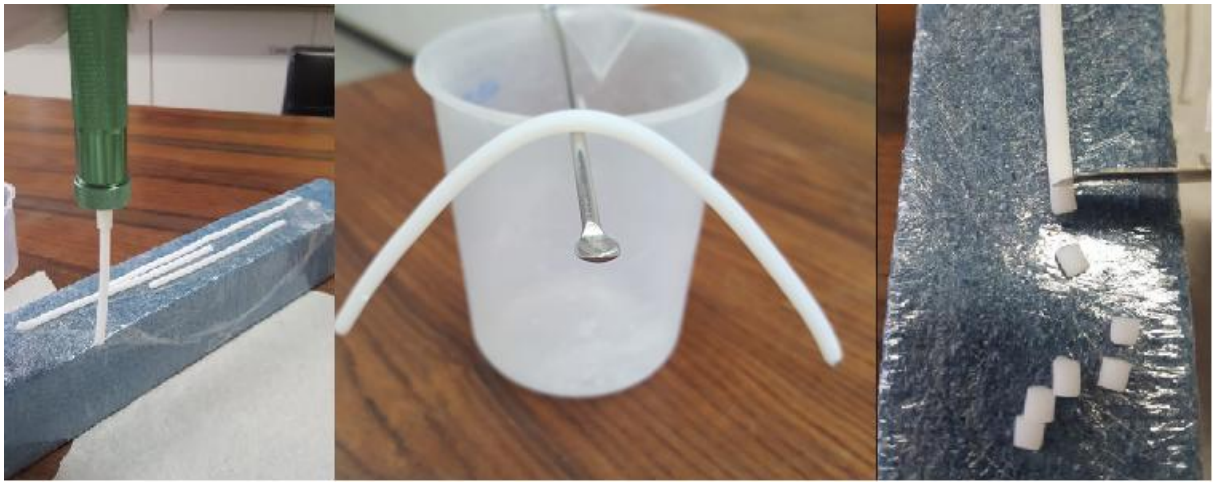

Figure 28: Fumed silica green body extrudates prepared with 20 % of methocel.

Another important concern regarding the extrusion process is how to fill the extruder properly with the paste, avoiding the formation of bubbles. One can observe a surface defect, highlighted in Figure 29, caused by the presence of macro bubbles inside the extruder. To overcome this difficulty, the ideal extruder should work under vacuum condition, so micro and macro bubbles would be prevented from forming. Bubbles inside the material increase the local surface tensions, and could therefore, be responsible for future cracking of the material. Regarding the procedure of loading the material into the extruder, to avoid the formation of macro bubbles, paste was previously shaped into a cylinder (with a diameter slightly smaller than the one of the extruder).

Figure 29: Appearance of defect on the surface of the green body extruder due to presence of bubbles inside the extruder.

Concerning the SBA-15 silica, the methocel proved very effective in providing strength to the green body, as it can be seen in Figure 30. Nevertheless, the SBA-15 silica paste dried faster than the fumed silica paste. A possible explanation for this event is the fact that SBA-15 mesoporous silica works better as an adsorbent and desiccant than fumed silica, due to its features. Therefore, the SBA-15 silica rods were cut even more carefully.

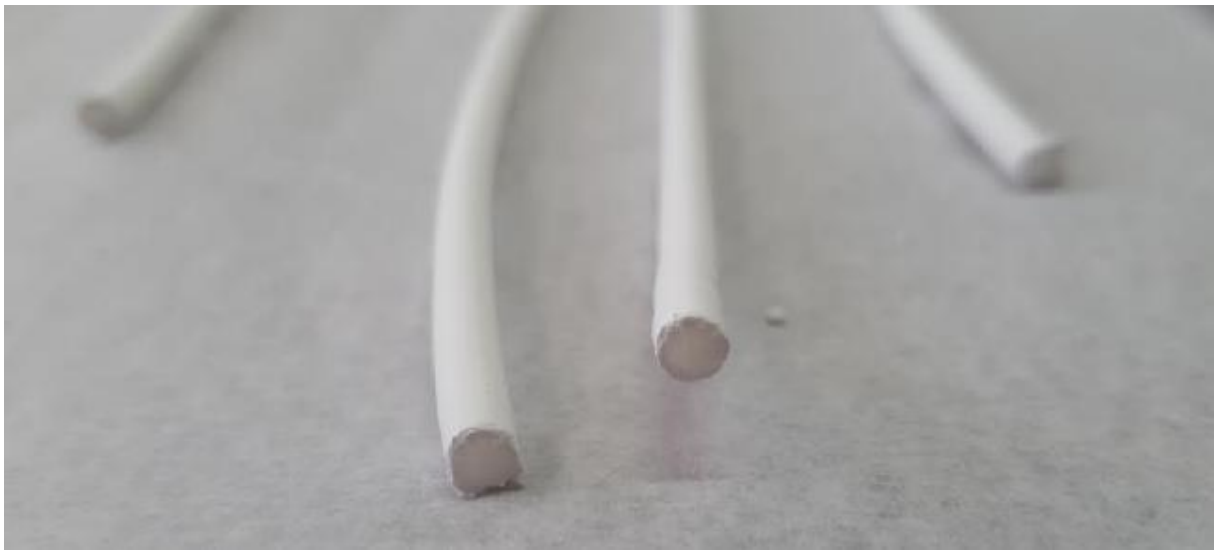

Figure 30: SBA-15 silica green body extrudates prepared with 20 % of methocel.

Concerning the production of spherical granules, the extrudate pellets were transferred to the spheroniser to be reshaped (round). It was difficult to define a specific rotation speed for the spheroniser, because it depends on the amount and the moisture content of the material loaded onto the frictional plate, and the amount of fines generated. These fines came from the breakage of the rods and they dropped down or accumulated in the space between the plate and the wall of the bowl, increasing the frictional force, and consequently, reducing the rotation speed of the plate. The rotational speed range used in the spheronisation process was adjusted as necessary from 6.5 to 14.3 revolutions / second. In addition, it was noticed that pellets with a lower content of binder were easier to be rounded. It could be related to the fact that fumed silica pellets containing 15% wt of methocel took longer to dry at room temperature than the others containing 20% wt. Therefore, the pellets containing less binder had enough time to get round at a low speed and produced less fines.

Moreover, Figure 31 shows the fumed silica sample containing 20% wt of methocel, before and after the spheronization step. The experiments showed that at a low speed, a smaller amount of loss of fine particles was generated. In addition, different sizes of pellets require different times for granulation and speed of rotation. Because the tendency of the granules is to get dried afterwards, some of them were removed before breaking, and thus, not achieving the spherical shape desired, as highlighted in Figure 32. The main spheronisation mechanism identified in this process is the one explained by Rowe (58), in which pellets with lengths approximately equal to their diameters had their edges rounded off and their overall shape changed from rods to dumb-bells and then to ellipsoids and finally got transformed into spheres. The Krueger's mechanism (61) was also noticed, explaining the generation of fines during the spheronisation process, and the agglomerated part of them onto the surface of the granules.

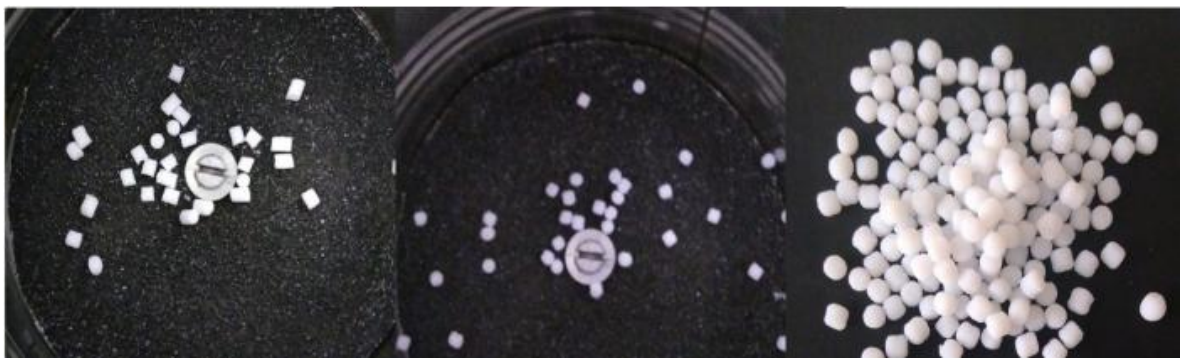

Figure 31: Photograph of the spheronisation process that shaped small rods of fumed silica, containing 20 % wt of methocel into round particles.

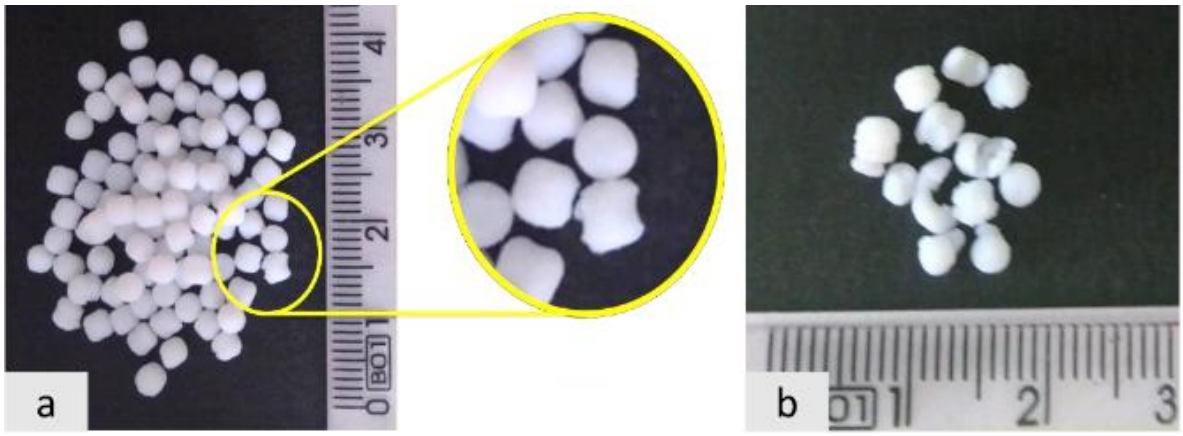

Figure 32: Defective granules obtained from the spheronisation process of the fumed silica, prepared with 15% wt: A - non-spherical granules due to lack of time in the spheroniser equipment. B – Broken granules exceeded the time required to get rounded.

Concerning the mesoporous silica SBA-15, previously synthesised at LMC Laboratory, the material was resistant to reshaping (into spheres). Despite the fact that the paste obtained an ideal consistency, the rods showed to be adhesive and sticky to the base and the wall of the spheroniser. Therefore, the rods had a tendency to stick together, creating large agglomerates. In other to overcome this event, several attempts were made, e.g decreasing the moisture content, waiting more time for the rods to get dry (before being loaded into the spheroniser) and testing different rotational speeds. Unfortunately, all these attempts failed to effectively reduce the stickiness of the material. Only when a small amount of rods (5 units maximum) was loaded into the spheroniser, working at low speed, it was possible to get the edges rounded. Even then, the SBA-15 rods broke before they turned into spheres. Therefore, SBA-15 silica was granulised by the extrusion process only. Due to the small amount available of SBA-15 silica, it was preferred to conform it into pellets to avoid wasting material during the spheronisation step. The SBA-15 green body extrudates obtained desired consistency and plasticity to be cut into small pellets with approximately 4 cm length, as shown in Figure 33.

Figure 33: SBA-15 green body pellets prepared with 20 % of methocel.

All the wet extrudate samples were dried over night (at temperature of 60 °C), and then, it was observed that the dried bodies became whiter and more rigid. After the calcination step, the volume of the final pellets (of all samples) decreased. This was already expected, because the surfactant, the water and the binder present in the mixture, were eliminated during the heat treatment, i.e. reducing the volume of the final body.

The photographs of the final bodies obtained in this work are shown in Figure 34. This illustrates a successful production of free-clay solid bodies, in size of millimetres, using methocel as the organic binder.

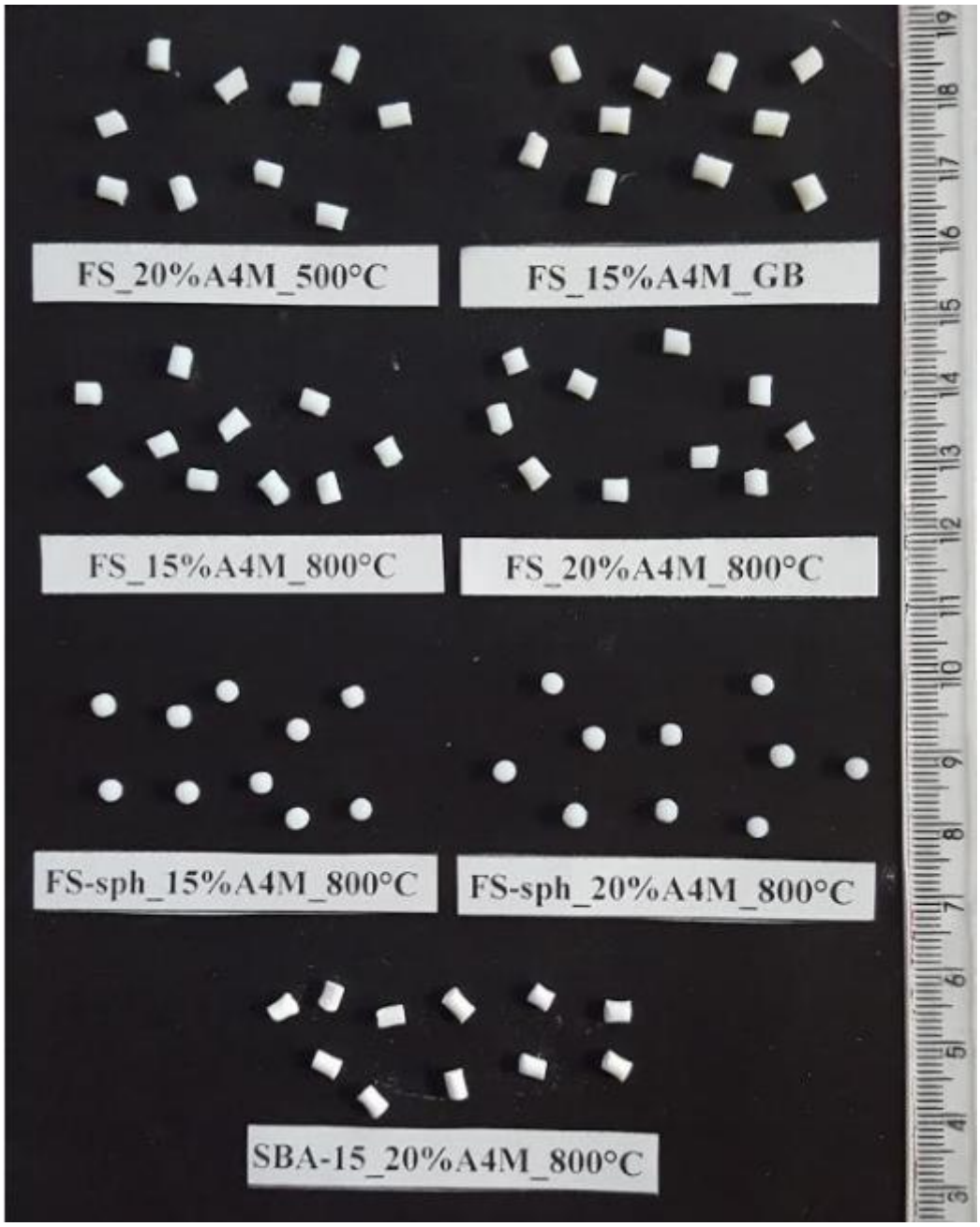

Figure 34: Photograph of the final bodies from extrusion and spheronization processes for samples FS_20%A4M_500°C, FS_15%A4M_GB, FS_15%A4M_800°C, FS_20%A4M_800°C, FS-sph_15%A4M_800°C, FS-sph_20%A4M_800°C, SBA-15_20%A4M_800°C.

By Image-J software analysis, it was obtained the average diameter and sphericity for spherical granules of fumed silica and SBA-15 mesoporous silica (prepared with 20 % wt of binder and calcinated at 800 °C), and for commercial zeolites. From each sample, 50 granules were analysed, and the main results are presented in Table 3. Furthermore, the Image-J results are presented in APPENDIX I. When analysing the results, one noticed that the average diameter of silica spherical granules produced (in this work) is approximately 1 mm bigger

than commercial zeolite average diameter (Figure 35), but the roundness of all samples were almost the same. The standard deviation for all roundness measurements was less than 10 %, indicating a satisfactory quality of spheronisation process. Additionally, even though the fumed silica granules (prepared in this work) showed bigger diameters than the commercial zeolites, they presented a lower standard deviation, which indicates a better size uniformity among the granules produced (Figure 36).

Table 3: Image-J results for spherical granules of fumed silica, SBA-15 silica and commercial zeolite Grace.

SAMPLES	Count	Diameter (mm)				Roundness			
		mean	StdDev	min	max	mean	StdDev	min	max
FS-sph_ 15%A4M_800°C	50	3.33	0.12	3.00	3.56	0.92	0.05	0.83	0.99
FS-sph_ 20%A4M_800°C	50	3.24	0.13	2.98	3.50	0.92	0.04	0.81	0.99
Commercial Zeolite Grace	50	2.24	0.19	2.78	9.97	0.93	0.03	0.84	0.99

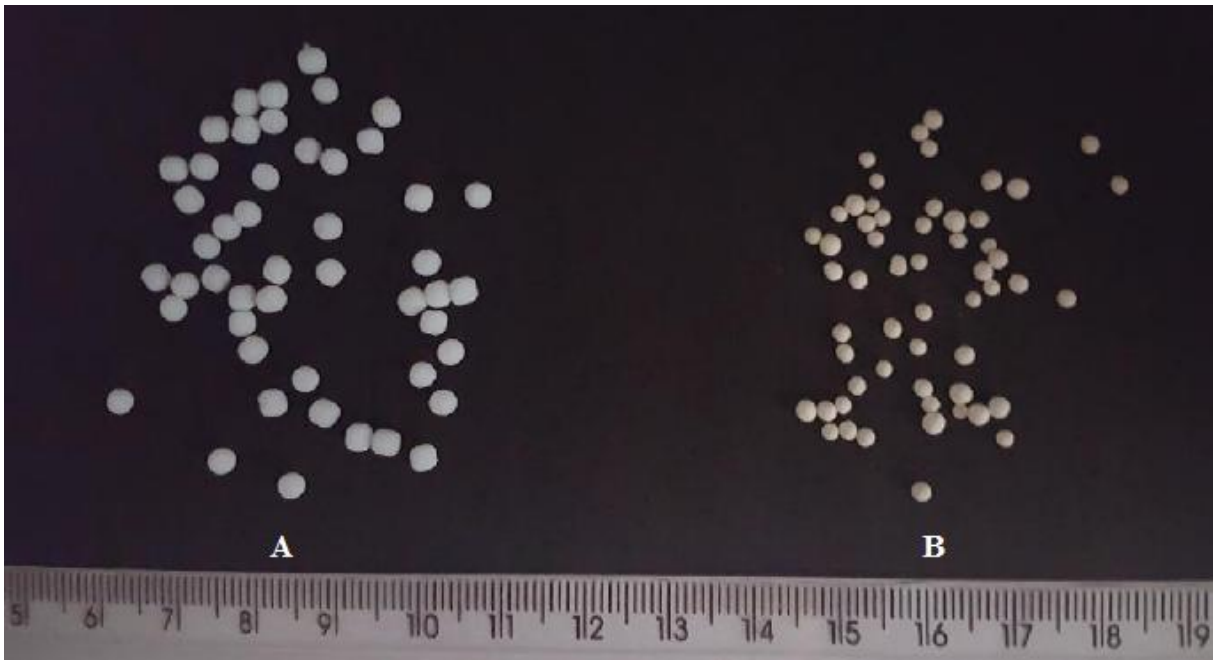

Figure 35: Photo of final fumed silica spherical granules prepared with 15 % of binder (A) and commercial zeolite granules.

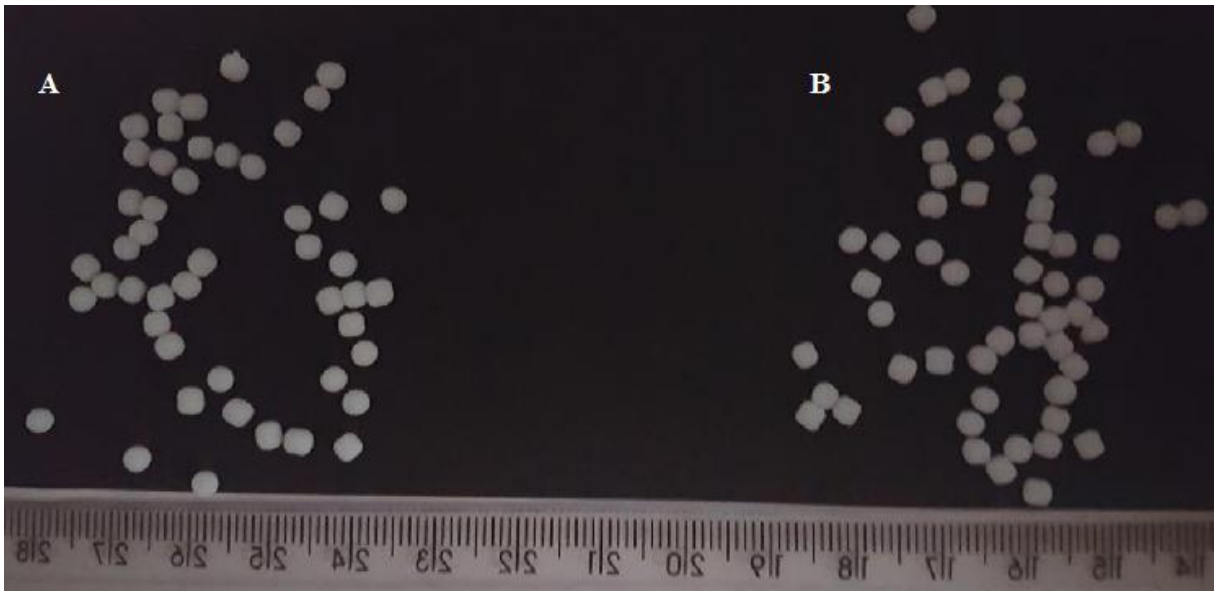

Figure 36: Uniformity between final fumed silica spherical granules prepared with 15 % (A) and 20 % (B) of binder

5.1. Absence of binder

The absence of binder used (Methocel A4M) was analysed comparing green body samples and calcinated of both fumed silica and mesoporous SBA-15 silica samples.

5.1.1. Thermogravimetry

The thermogravimetry analysis of methocel A4M was carried from 30 to 500 °C. The TG and DTG curves obtained are presented in Figure 37. The DTG curve shows two distinct stages of weight losses. The first weight loss occurred around 60 °C and it is attributed to desorption of gases and absorbed water. The second major weight loss occurred around 340 °C and it is due to decomposition of methocel. The final weight is zero, which indicates the complete decomposition of the methocel A4M. Therefore, the dried extrudates were calcinated above this temperature to remove the methocel, hence, producing polymer free granules.

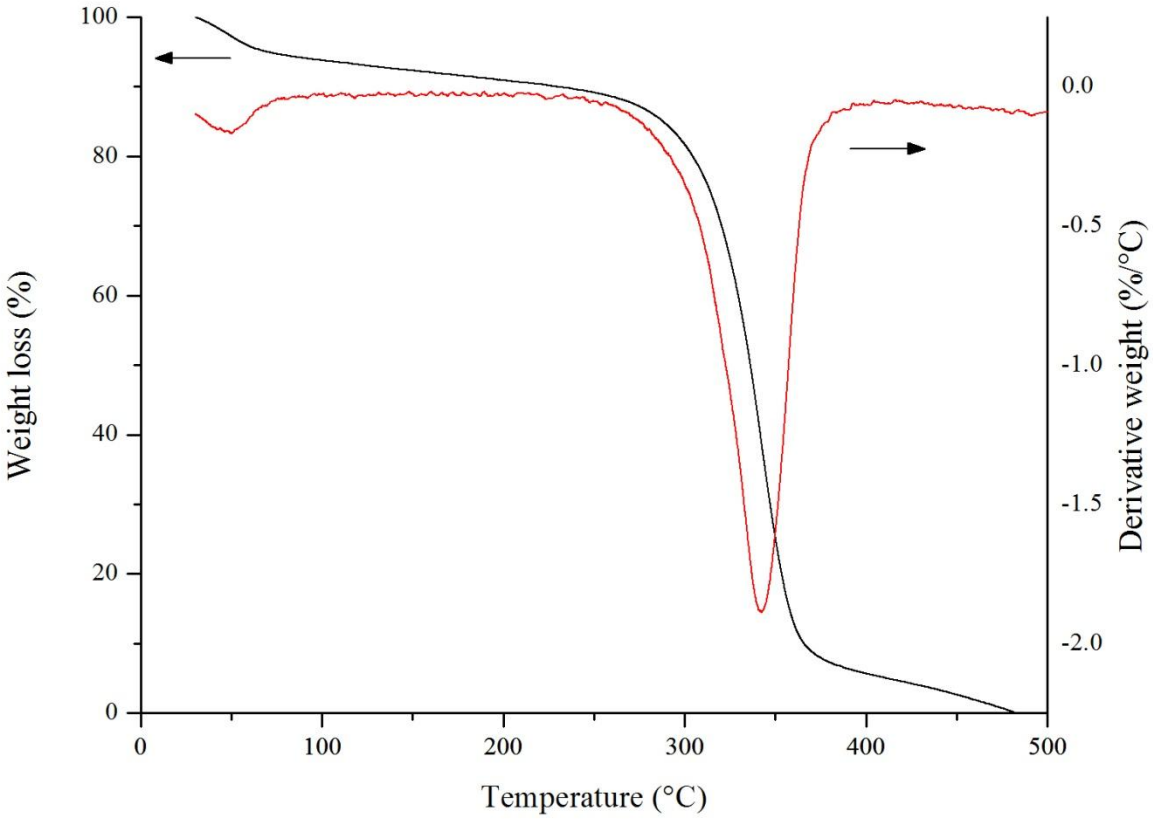

Figure 37: TG and DTG curves of Methocel A4M.

Figure 38 shows the thermogravimetry curves, carried out from between 30 to 800 °C of the green body of fumed silica extrudates. The DTG curve shows three distinct stages of weight losses. The first weight loss occurred around 60 °C and it is attributed to desorption of gases and absorbed water. The second major weight loss occurred around 370 °C and it is due to decomposition of methocel. Then, from 400 to 500 °C, the curve presented a steady weight loss, which can be associated with the release of - OH groups (present on the surface of the material) (6).

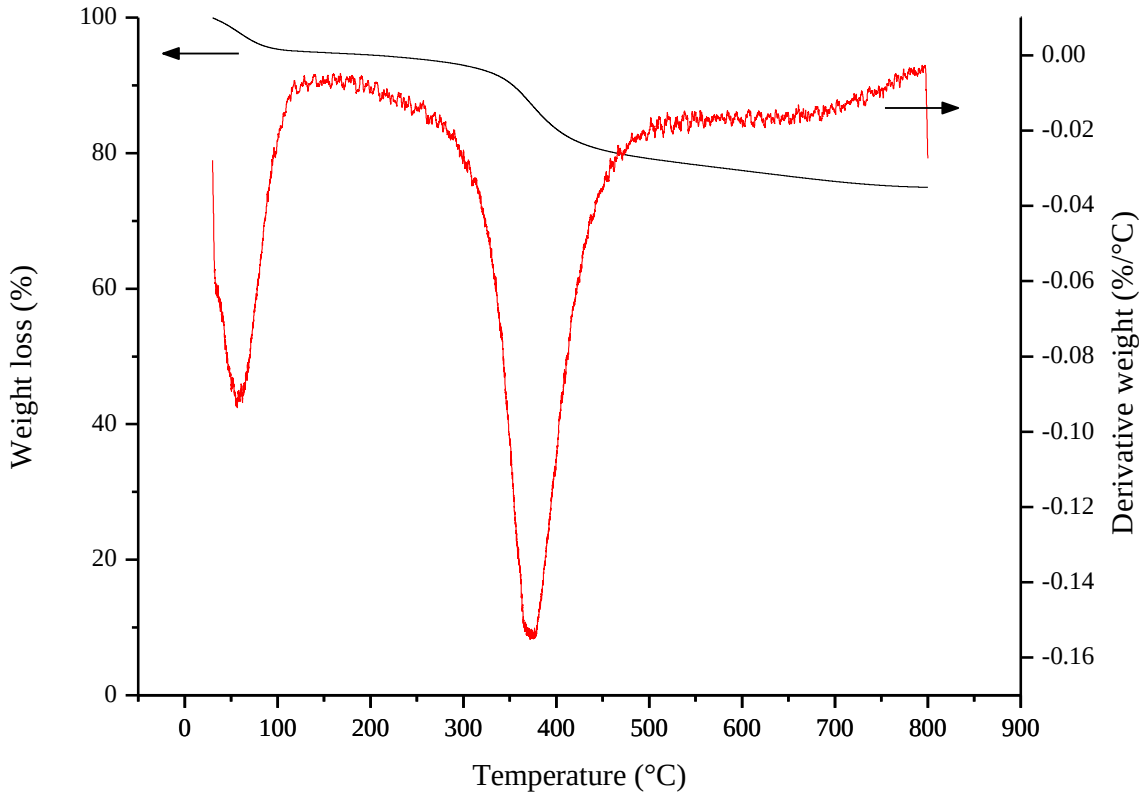

Figure 38: TG and DTG curves of green bodies of fumed silica extrudates.

Figure 39 shows the thermogravimetry curves obtained for the green body of SBA-15 silica extrudates, carried out from between 30 to 800 °C. The DTG curve shows three distinct stages of weight losses. The first weight loss occurred around 60 °C can be attributed to desorption of gases and adsorbed water. The second weight loss occurred around 190 °C and it is due to the release of adsorbed water (68). The third weight loss occurred around 340 °C, indicating the decomposition of methocel, confirmed by TG of methocel, and the decomposition of Pluronic 123 surfactant (P123), as previous studied by Almeida et al (69). It is important to emphasise that the SBA-15 powders worked in this research were not previously calcinated, i.e. the P123 surfactant was present in the micro-mesoporous structure during granulation process. Therefore, all the organic binder was removed when the dried extrudates were subjected to heat treatment above 500 °C. From 400 to 800 °C, the curve presents a steady weight loss, which can be associated with the release of -OH groups, present on the surface of the material. This behaviour has been previous described by Ribeiro (2016), namely when she was analysing the SBA-15 silica developed in her research (6).

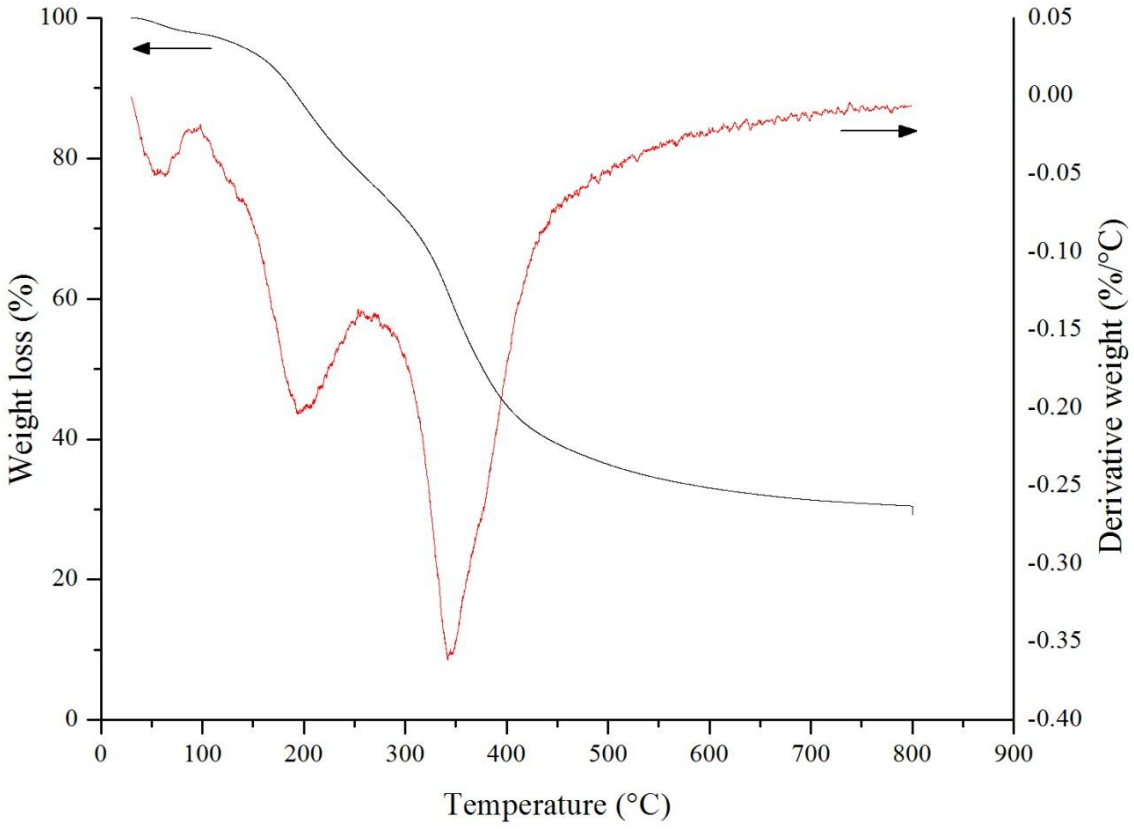

Figure 39: TG and DTG curves of green bodies of SBA-15 silica extrudates.

5.1.2. FTIR

Figure 40 shows the FTIR spectra of the following samples: fumed silica in powder, granule of fumed silica prepared with 20 % of binder after heat treatment at 800 °C, green body granules of fumed silica prepared with 15% of binder, and methocel. The FTIR spectra of pure methocel shows typical peaks, e.g. at 3449 cm^{-1} assigned to O-H stretching, at 1644 cm^{-1} related to sugar ring and 1067 cm^{-1} due to C-O (ether) stretching (70). Concerning silica samples, the main bands are from 3700 to 3200 cm^{-1}, due to O-H stretching, and from 1300 to 1000 cm^{-1}, due to Si-O-Si asymmetric stretching (71). When comparing the FTIR spectrums, one can observe the organic peaks highlighted in methocel spectra were also found in the sample of fumed silica containing 15 % of binder, indicating the presence of the binder in the sample. On the other hand, these peaks were not found in the sample that was calcinated. Additionally, the initial fumed silica powder and the fumed silica granules, calcinated at 800

°C, have similar spectra, proving the complete removal of the methocel (used as an organic binder). However, one can observe a weaker intensity of O-H stretching band in granules of fumed silica (calcinated at 800 °C). This is attributed to the release of -OH groups present on the surface of the material, during granulation process, but mainly because the fact that the granules were heated up to 800 °C. Analogous, the green body granules of fumed silica showed a slightly weaker O-H stretching band than fumed silica powder. This is due to the release of -OH groups present on the surface of the material during the granulation process.

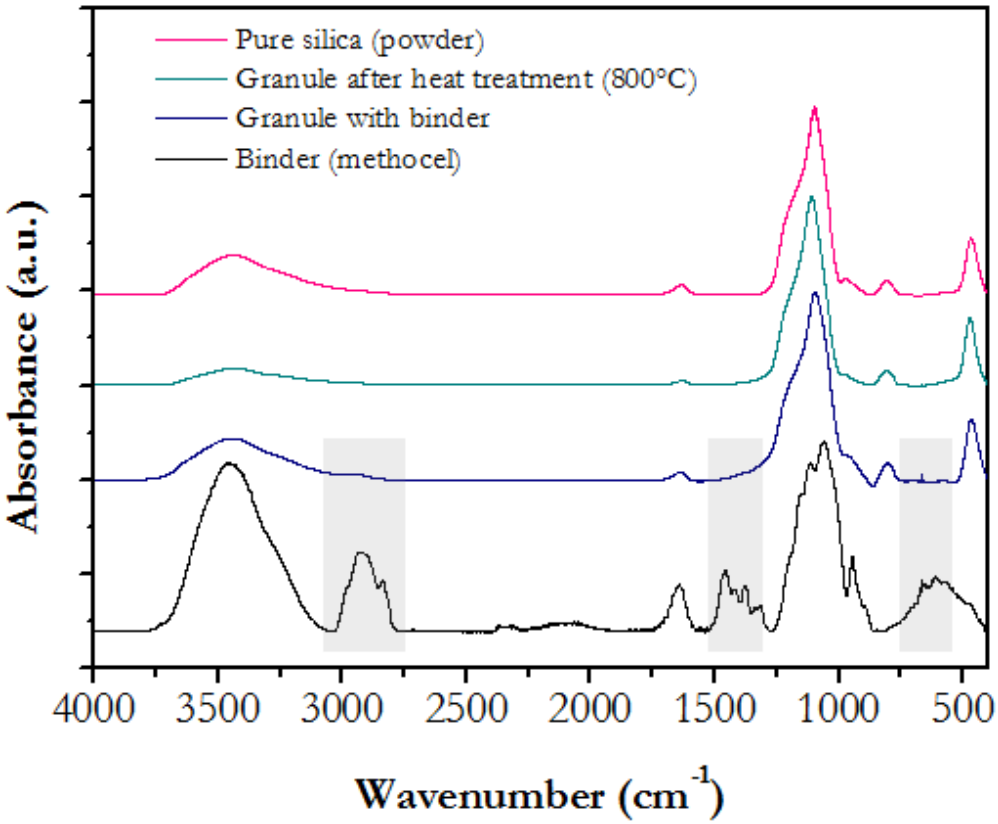

Figure 40: FTIR absorption spectra of fumed silica powder, granules of fumed silica after calcination at 800 °C, green body granules of fumed silica containing 15 % wt of organic binder, and methocel AM4 used as the organic binder.

The FTIR spectra of SBA-15 silica samples are shown in Figure 41. Concerning the SBA-15 silica samples, the main bands are from 3700 to 3200 cm^{-1}, caused by O-H stretching, and from 1300 to 1000 cm-1, due to Si-O-Si asymmetric stretching, exactly as described in the FTIR analysis of fumed silica samples. This result was expected, since both are made of silica. Moreover, these similar curves indicate that both the fumed silica powder and the SBA-15 powder are lack impurities. Comparing the FTIR spectrums of SBA-15 samples, one can observe that organic peaks present in the methocel spectra, are also found in the sample of

SBA-15 containing 20 % of binder, indicating the presence of the binder in the sample. On the other hand, these peaks were not found in the calcinated sample, demonstrating the removal of the organic binder used. Additionally, the characteristic O-H stretching band (3700 to 3200 cm^{-1}) is less intensive in the SBA-15 powder, calcinated at 800 °C, and the SBA-15 granule also, calcinated at 800 °C, than in the un-calcinated green body SBA-15 granules. This is due to the fact that both calcinated samples had the –OH group released from the surface during the heat procedure.

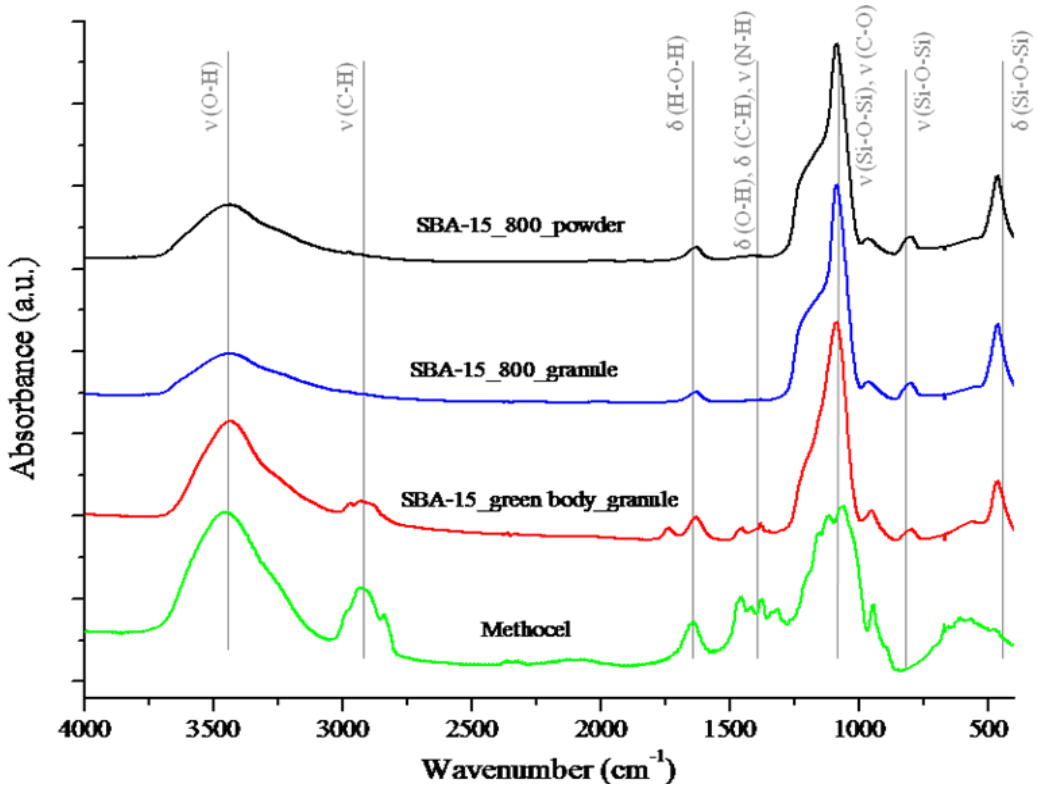

Figure 41: Fourier transform infrared (FTIR) absorption spectra of SBA-15 samples, before and after heat treatment at 800 °C, and methocel used as the organic binder.

Finally, based on all these FTIR absorption spectra results, it is strongly believed that pure granules of fumed silica and SBA-15 silica were produced, using methocel A4M as the organic binder.

5.2. Evaluation of porosity and water absorption capacity

The influence of the granulation process and the calcination temperature on the final surface area, porosity and water absorption capacity was analysed by comparing the different SBA-15 samples, by N_2 sorption and water sorption analyses.

5.2.1. Nitrogen adsorption

Nitrogen adsorption isotherms of SBA-15 mesoporous silica samples are shown in Figure 42, while the pore size distribution is shown in Figure 43. Finally, the surface area and pore volume are listed on Table 4. One can observe the shape of all isotherms exhibit type IV of IUPAC classification and an H1-type hysteresis loop (10), characteristic of mesoporous materials. This means that the mesoporous structure was not changed by the granulation process. However, there are important changes that should be pointed out. The main difference observed is the better adsorption performance of SBA-15 silica powder, calcinated at 550 °C, i.e. the sample showed a higher adsorbed volume for low and high relative N_2 pressures. The surface area decreased almost by half, i.e. from 757 m^2/g (in SBA-15 powder calcinated at 550 °C) to 386 m^2/g (in SBA-15 powder calcinated at 800 °C). It is believed that the reduction of the surface area is due to the elimination of some micropores, as shown in the pore size distributions graph. This result confirms that the porosity and surface area are strongly depended on the calcination temperature, rather than the granulation process (8). The increase of temperature decreases the concentration of -OH groups on the surface of the material and enlarges some mesoporous pores. Regarding the SBA-15 silica samples, calcinated at 800 °C, one can notice a slight increase of adsorption volume in the granules samples at higher relative N_2 pressures. The surface area and pore volume of SBA-15 granules calcinated at 800 °C are found to be around 392 m^2/g and 0.53 cm^3/g, respectively. In addition, SBA-15 extrudates showed a narrow distribution pore size, with pore size of 7 nm.

The surface area obtained for samples prepared in this work showed better results when compared to Chandrasekar's (2009) (1) results. In more detail, when the calcination temperature increased from 550 to 750 °C, the surface area of his SBA-15 extrudates decreased from 640 to 400 m^2/g, and only 261 m^2/g, when the temperature was above 750 °C. Chandrasekar's SBA-15 extrudates were prepared with 2.2 % wt of bentonite and 2.2 % wt of methylcellulose, while the samples in this work are clay-free.

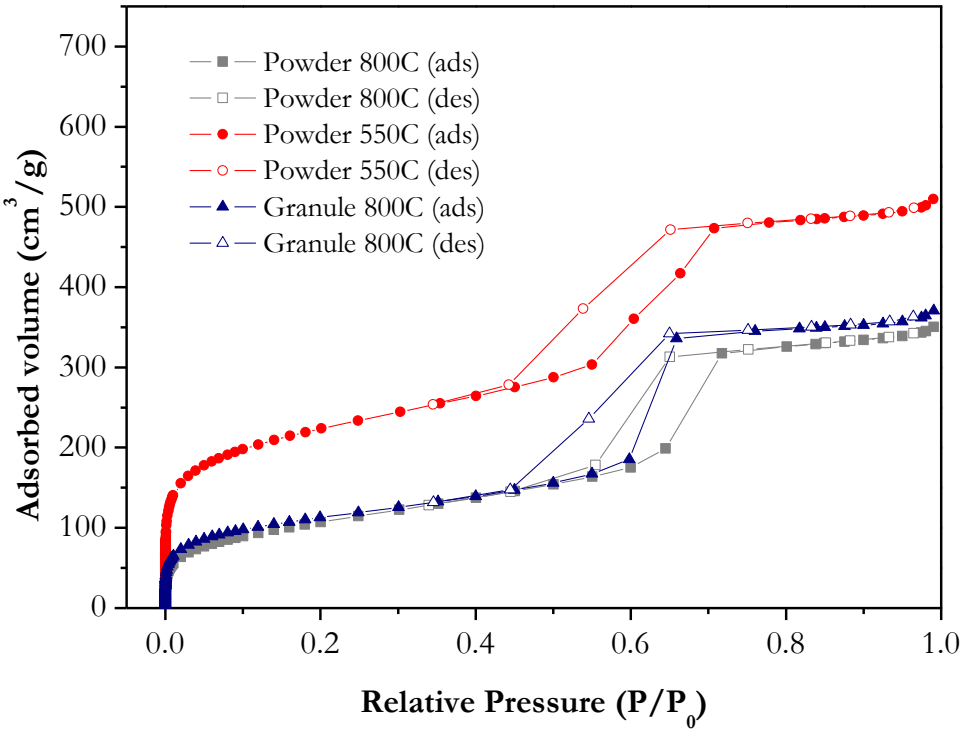

Figure 42: Nitrogen adsorption isotherms of SBA-15 mesoporous silica samples.

Table 4: The surface area and the pore volume results for SBA-15 samples.

SAMPLES	S_A (m^2/g)	V_{pores} (cm^3/g)
SBA-15_powder_550°C	757,80	0.73
SBA-15_powder_800°C	386,21	0.50
SBA-15_granules_800°C	392,24	0.53

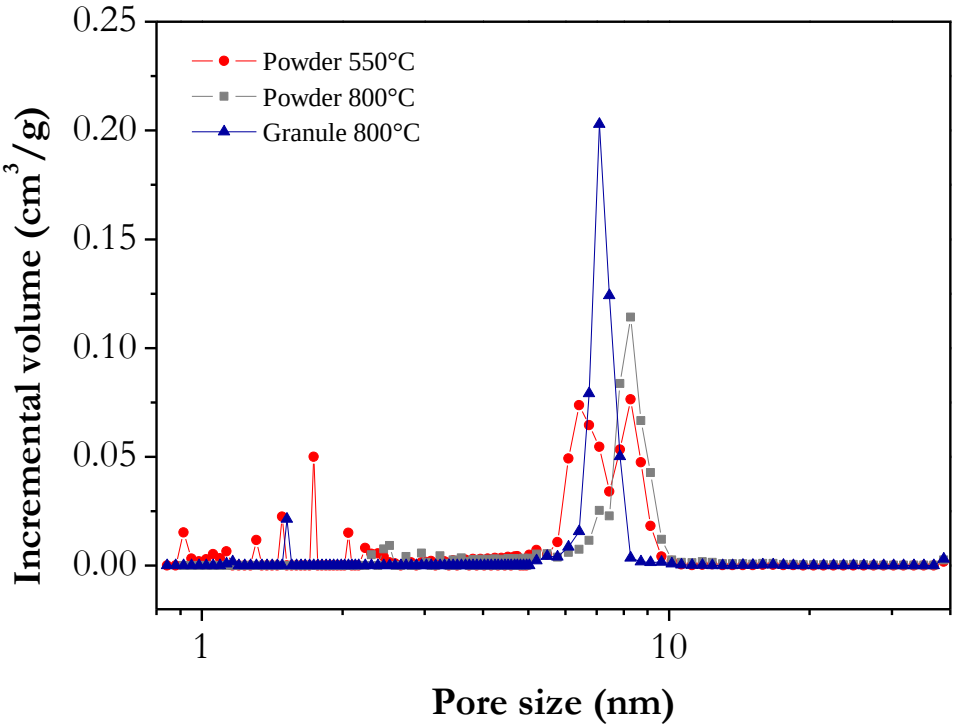

Figure 43: Pore size distribution of SBA-15 silica samples.

5.2.2. Water adsorption

Figure 44 shows the water sorption results for SBA-15 mesoporous silica samples prepared in this work. One can observe that the typical shape of water sorption isotherm for hexagonally ordered silica materials is clearly represented by SBA-15 powder isotherm, calcinated at 550 °C, according to Kocherbitov (2011) (72). The water sorption isotherm consists of four regimes (I - IV), listed below.

- Regime I regards the beginning of water sorption on the silica surface of both intrawall and the main mesopores. At low water contents, the driving force of hydration is adsorption of water molecules to –OH groups on the silica surface.
- Regime II corresponds to the capillary condensation in intrawall pores and adsorption in mesopores, and this isotherm's feature is typical for mesoporous materials.
- Regime III relates to capillary condensation in the mesopores.

- Regime IV corresponds to post-capillary condensation of water.

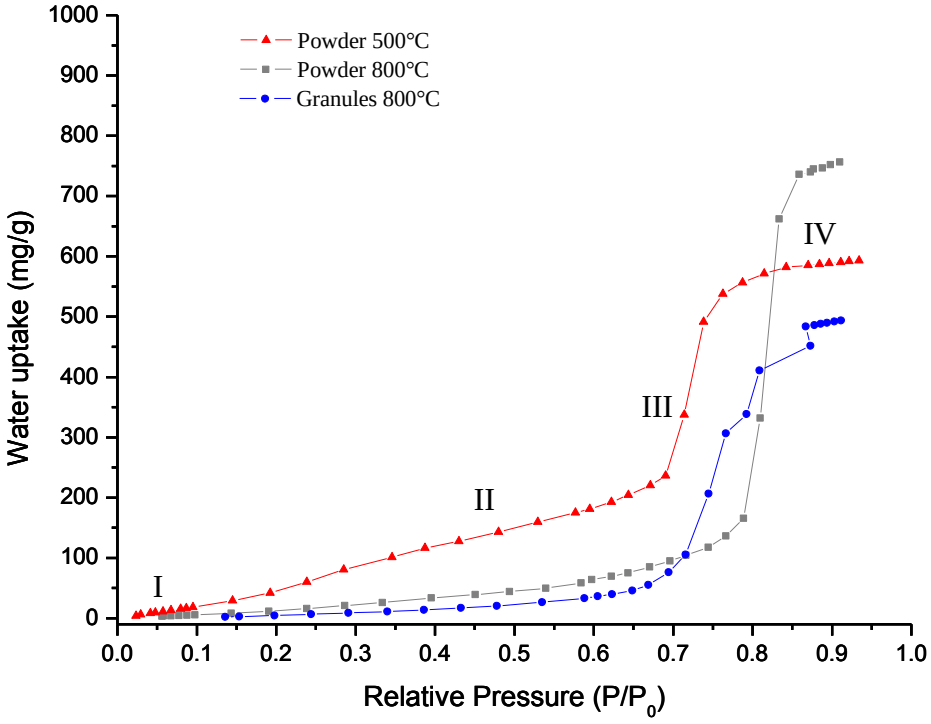

Figure 44: Comparison of water sorption of SBA-15 samples.

Figure 45 illustrates a scheme of 2nd regime of water sorption in SBA-15 mesoporous silica (72), where some micropores are saturated and others not (where spheres of 0.3 nm diameter represent water molecules).

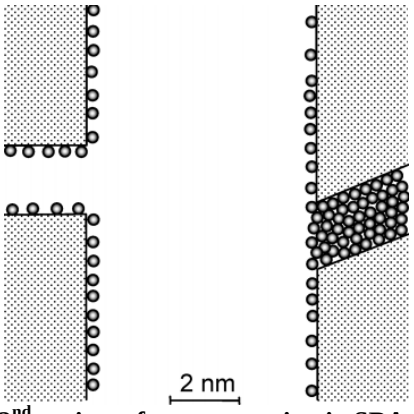

Figure 45: Scheme of the 2nd regime of water sorption in SBA-15 mesoporous materials.

Concerning the Figure 44, the sorption of water molecules at low water activities is less for the calcinated samples at 800 °C. Additionally, the separation between regime I and regime II is not very distinguishable in those water sorption isotherms. This could be explained by the

fact that once the samples are calcinated at high temperatures, the number of micropores and the amount of silanol groups on the surface decrease (as shown in Figure 43) (73). Hence, the presence of micropores and silanol groups on the silica surface are responsible for the early start and more intense water sorption in the SBA-15 powder sample, calcinated at 550 °C. Furthermore, one can observe that the SBA-15 powder calcinated at 550 °C reaches the water saturation before the others, with approximately 600 mg/g water sorption capacity.

The SBA-15 powder sample (calcinated at 800 °C) saturated with the most adsorbed water volume as compared to the others (~760 mg/g), at high water activity. This difference could be explained by the greater number of large mesopores present in the sample SBA-15 powder, calcinated at 800 °C. The SBA-15 granules calcinated at 800 °C had a weak performance in water sorption saturation, even though these granules have a slightly higher surface area. The granulation process made the SBA-15 extrudate less hydrophilic. Falkin (2013) (74) also observed that the water sorption rate decreases with the size of granules. However, opposite to his conclusions that the size of granules does not affect the final sorption performance, from Figure 44, it is clear that the SBA-15 granules showed less sorption capacity. To overcome this disadvantage (of the granulation process), as a future work suggestion, one could have an additional procedure to activate the surface of the granules, e.g. by acid attack. Thus, the concentration of -OH groups available on the surface of silica would increase, becoming more hygroscopic. Finally, the volume of water uptaken for SBA-15 granules calcinated at 800 °C in this work (~ 600 mg/g water sorption) was similar to the zeolites granules results (0 to 5 mm) worked by Falkin (2013) (74).

5.3. Crush strength

In order to eliminate the effect of size and shape of extrudates in the crushing strength test, the results are expressed in crushing stress (σ) instead of crushing load. The crushing stress is directly proportional to the applied load on the extrudates. Hence, an increase in crushing stress leads to the increase in the mechanical strength of the extrudates.

To perform the mechanical strength tests, the vertical surface of the extrudates was smoothened by the sandpaper with a fine grit, in order to enhance the uniform distribution of

the load. The axial and diametrical crushing stresses of the extrudates are represented by equations 4.1 and 4.2, respectively (75):

$$\sigma = \frac{4F}{\pi D^2} \qquad \text{(Eq. 4.1)}$$

$$\sigma = \frac{2F}{3.14DH} \qquad \text{(Eq. 4.2)}$$

where, *F* is the load applied at the point of breakage, *D* is the particle diameter and *H* is the particle length.

Each extrudate was inserted in the microtomograph equipment, as shown in Figure 46, and the load was applied along the vertical (axial) and the horizontal (diametrical) directions of the cylindrical extrudates until it exhibited failure. About 10 cylindrical extrudates with 3 mm diameter and 4 mm length were subjected to the crushing strength test from each set of the paste composition. All results are listed in the Appendix II.

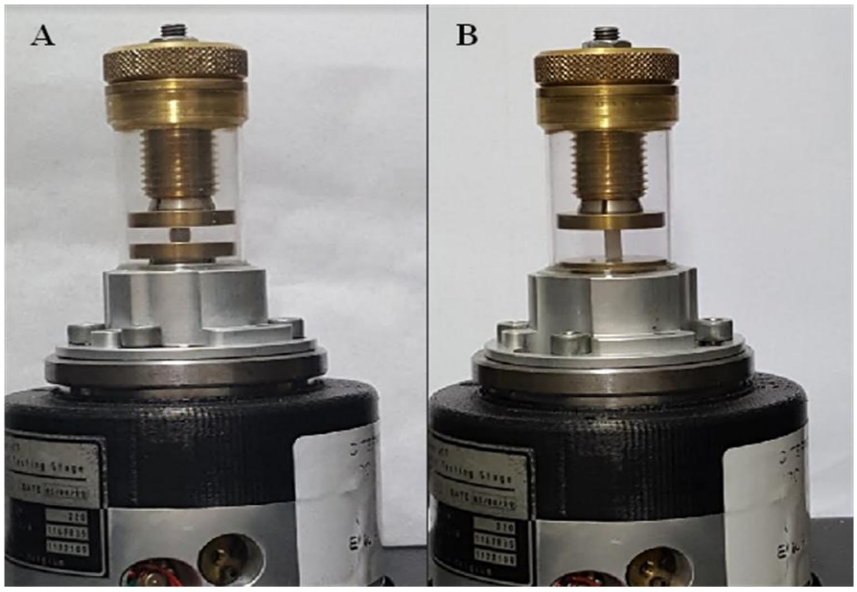

Figure 46: Illustrations of the diametrical (A) and the axial (B) crushing testes of cylindrical extrudates.

Figure 47 shows the results of the clay-free cylindrical extrudates tested (fumed silica prepared with 20 % wt methocel and calcinated at 800 °C and 500 °C, SBA-15 prepared with 20% wt methocel and calcinated at 800 °C). One can observe the significant difference between the samples calcinated at 800 °C and 500 °C. The fumed silica sample calcinated at the temperature of 500 °C demonstrated to be the least resistant, with the lowest crushing

stresses. The increase of the mechanical strength is related to the formation of stronger chemical bonds at a higher temperature. Therefore, more energy is necessary to break them.

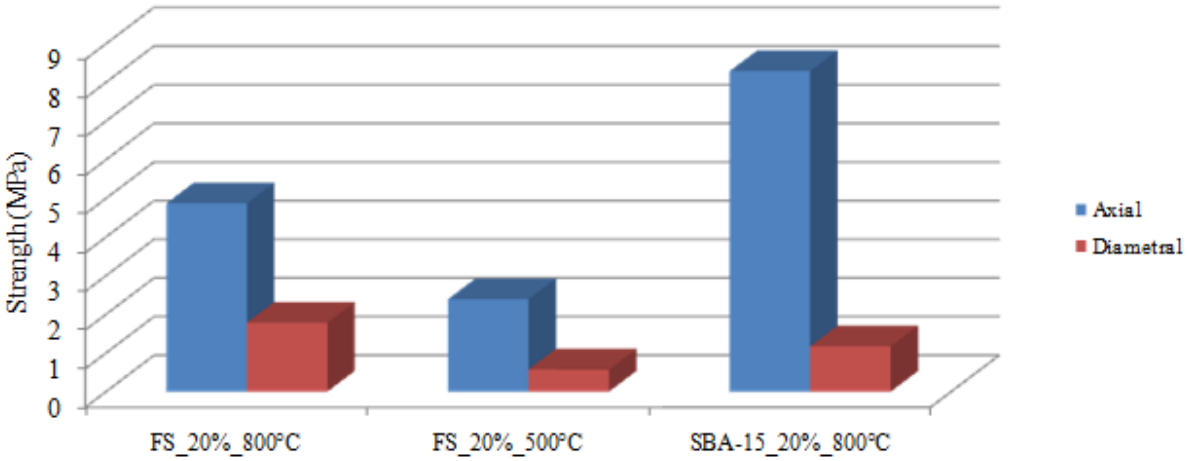

Figure 47: crush strength

In addition, the SBA-15 extrudates's axial crushing stress (obtained in this work) was higher when compared to the Chandrasekar's results (1). The axial crushing stress of SBA-15 extrudates was 8.3 MPa, while the SBA-15 extrudate pellets from Chandrasekar, which they were mixed with bentonite (inorganic binder) and methycellulose (organic binder and plasticizer), varied from 0.4 to 3.4 MPa. Furthermore, the fumed silica extrudate calcinated at the temperature of 500 °C had the axial crushing stress (2.4 MPa) in the range obtained by Chandrasekar. This is an important result, since the clay-free silica granules produced in this work have similar or better mechanical performance compared to the literature.

Due to the spherical particle of commercial zeolite Grace, the tensile stresses were calculated using Equation 4.3:

$$\sigma = \frac{2.8F}{\pi D^2} \qquad \text{(Eq. 4.3)}$$

where, *F* is the load applied at the point of breakage and *D* is the particle diameter. The detailed results are shown in Appendix II.

Figure 48 schematically shows the crush strength results obtained for the clay-free pellets produced in this work. The crush strength value obtained for the zeolite by Equation 4.3 is also given as reference. The results obtained show that the clay-free pellets produced present a

mechanical strength similar to that presented by clay-containing commercial zeolites. Therefore, the granulation process has so far been proven as a promising conformation process for obtaining clay-free pellets.

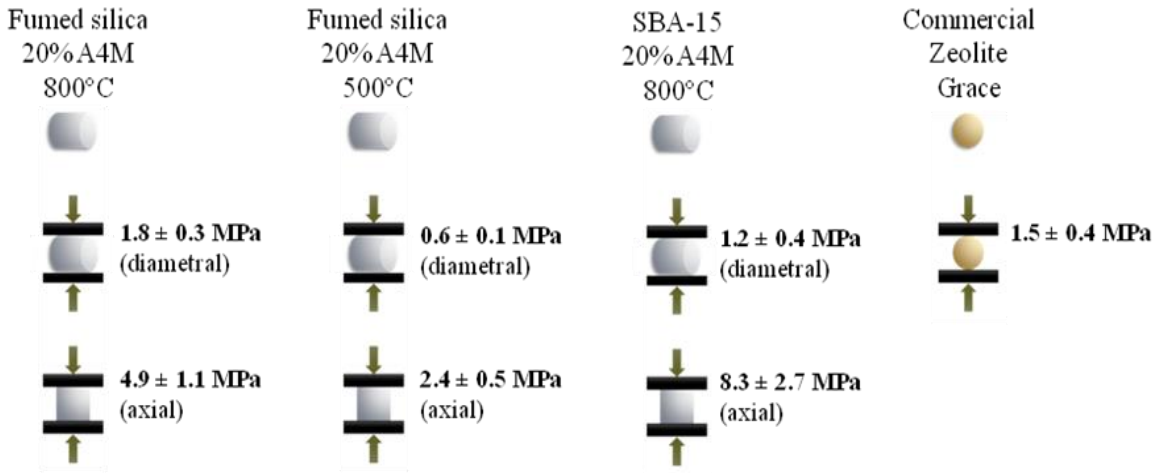

Figure 48: Crush strength results obtained for commercial zeolite Grace and clay-free extrudates of fumed.

5.3.1. Bulk crush strength

In order to evaluate the resistance of a bed of the granules, obtained in this work, under compressive loading, bulk crush strength (BCS) tests were performed. Similar to previous crushing stress tests, the bulk crushing stress is also directly proportional to the applied load on the bed. An illustration of a bulk crush strength test is shown in Figure 49.

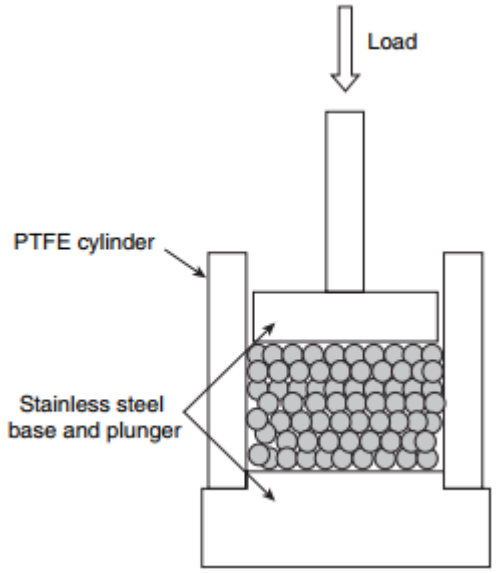

Figure 49: Generic piston-cylinder arrangement used for bulk crush strength tests.

In this test, a bed of a fixed volume of granules is compressed in a cylindrical cup to a specified pressure, for 30s. After unloading, the material is carefully removed from the cup, and the amount of fines produced by crushing at different loads is determined by sieving the total sample. Therefore, the crushing strength is then defined as the required load to produce 1 % wt of fines. For each granular sample obtained in this work, the test was performed in two different pressures (0.97 and 1.94 MPa), and for each pressure, three repetitions were made. The percentage of fines was, then, plotted against the crushing pressure, in a graph to determine the 1 % wt of fines generated. Figure 50 illustrates some stages of the BCS for SBA-15 extrudates.

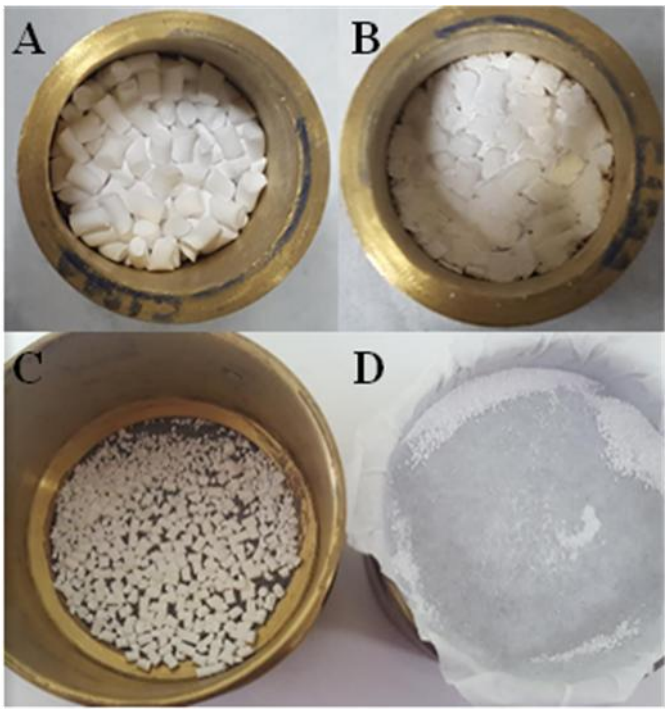

Figure 50: Some stages the bulk crush strength test for SBA-15 silica, where (A) is the initial volume of SBA-15 extrudates, (B) is the volume after unloading the pressure, and (C) e (D) are the broken granules and the fines generated, respectively, after the crushing test.

Appendix III lists all the partial results for the bulk crush strength test obtained in this work. Moreover, Table 5 shows the bulk crushing strength results. One can observe that the fumed silica granules samples (FS_20%A4M_800°C and FS-sph_20%A4M_800°C), prepared with 20% wt of methocel A4M, showed higher bulk crushing strength results among the samples calcinated at 800 °C. In addition, commercial zeolite Grace showed the higher resistance than the clay-free fumed silica samples. This was due to the presence of the clay in their composition. A sample without heat treatment (FS_15%A4M_uncalcined), containing 15% wt of organic binder (methocel) in its composition, showed a higher performance than the commercial Grace zeolites. This performance can be associated to the high weight and high viscosity of the methocel A4M used as the binder, which offers binding and hardness to the green body extrudates of fumed silica.

Table 5: Bulk crush strength results for granules of fumed silica.

Sample	Equation obtained from average of experimental values.	Calculated crush pressure to produce 1 wt% fines (MPa)
FS_20%A4M_800°C	y = 0.09x + 0.80	0.89
FS_15%A4M_800°C	y = 0.08x + 0.56	0.64
FS_20%A4M_500°C	y = 0.05x + 0.77	0.82
FS-sph_20%A4M_800°C	y = 0.13x + 0.86	0.99
FS-sph_15%A4M_800°C	y = 0.09x + 0.77	0.86
FS_15%A4M_GB	y = 3.10x + 0.44	3.54
SBA-15_20%A4M_800°C	y = 0.24x + 0.69	0.93
Commercial Zeolite Grace	y = 1.81x + 0.66	2.47

Moreover, FS_20%A4M_800°C extrudates showed a higher bulk crushing strength at 1 weight percent fines, than FS_15%A4M_800°C. This was expected, because the increase in methocel content can be related to an increase in the viscosity of the paste, by maintaining its uniformity and homogeneity. However, the bulk crush strength for fumed silica, prepared with 15 % wt of methocel and conformed into cylindrical extrudates, was significantly lower than the same samples shaped into spheres. The results should be approximately the same, due to the fact that this test should eliminate the size and geometry effect of the granules. Furthermore, the results of BCS were below the expected, when compared to zeolite. The presence of cracks in the interior of the samples is largely responsible for their low performance.

Regarding Figure 51 to Figure 56, it is possible to analyze the inclination of the curves, rather than the values themselves at 1 weight percent fines.

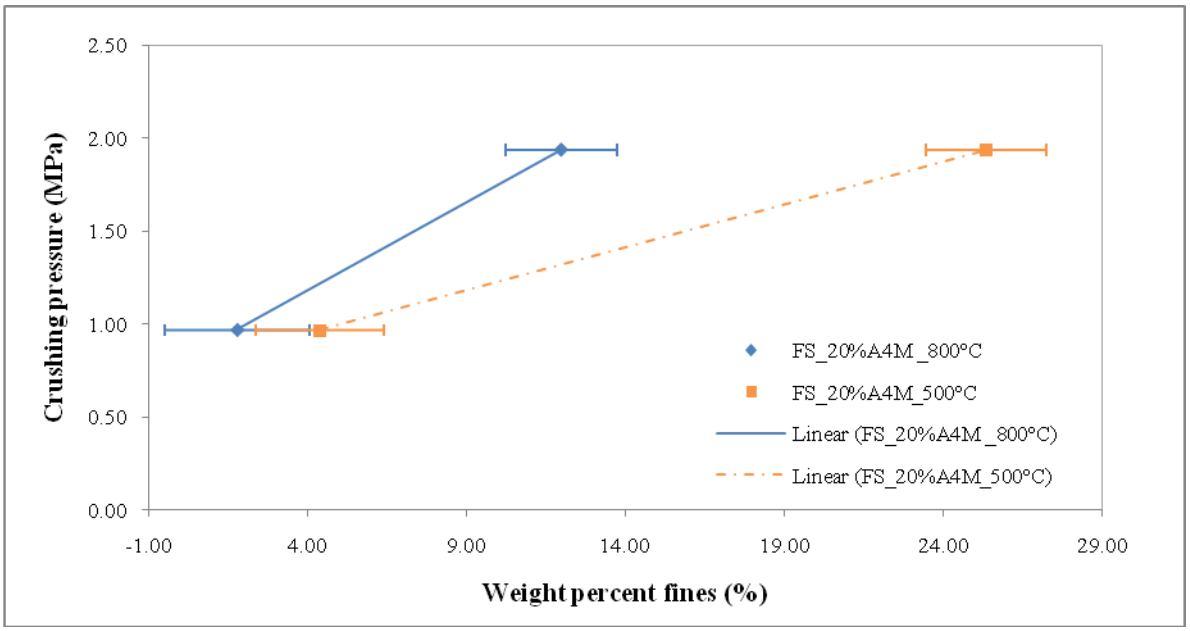

Figure 51: Bulk crushing strength results for fumed silica samples, prepared with 20% wt of binder and calcinated at 800 °C and 500 °C, respectively.

In Figure 51, the fumed silica sample prepared with 20 % of methocel and calcinated at 800 °C presents the highest curve inclination. Thus, the sample prepared with 20 % of binder has the highest strength.

In addition, in Figure 52, the fumed silica extrudate samples prepared with 20 % of binder presents a slightly bigger inclination than the samples prepared with 15 % of binder. Thus, the sample prepared with 20 % of binder has a highest strength.

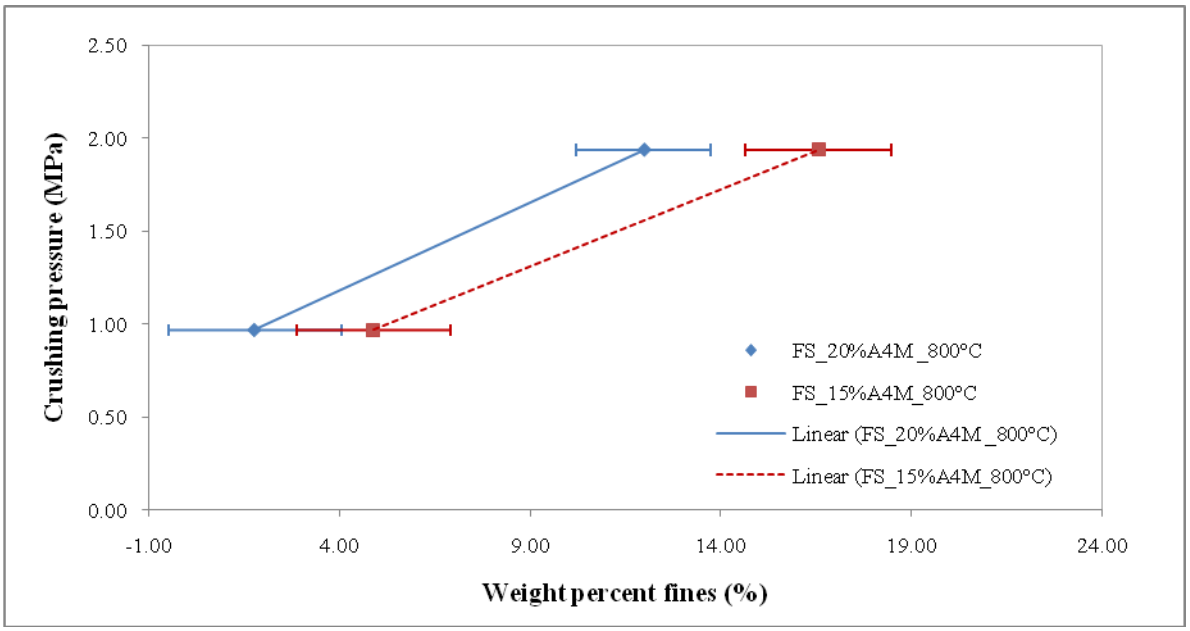

Figure 52: Bulk crushing strength results for fumed silica samples prepared with 20 % and 15 % wt of binder, respectively.

Comparing the geometry of the fumed silica extrudates (prepared with 20 % of binder and calcined at 800 °C), both cylinders and spheres presented competitive resistances, as shown in Figure 53 and Figure 54.

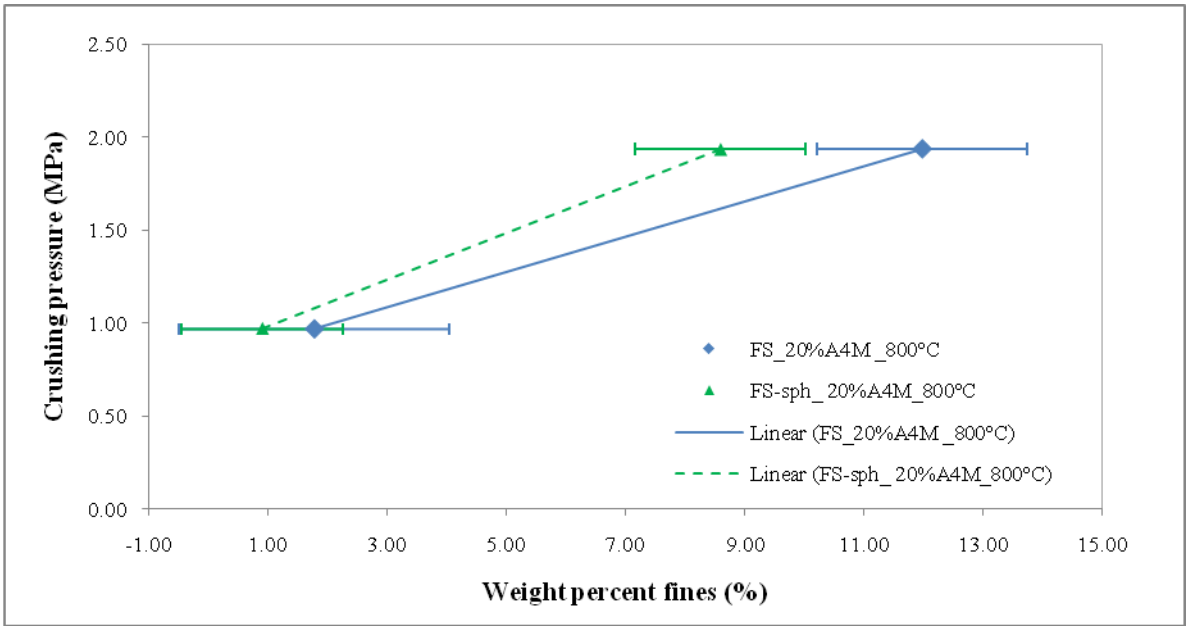

Figure 53: Bulk crushing strength results for cylindrical and spherical fumed silica samples, prepared with 20 % wt of binder and calcined at 800 °C.

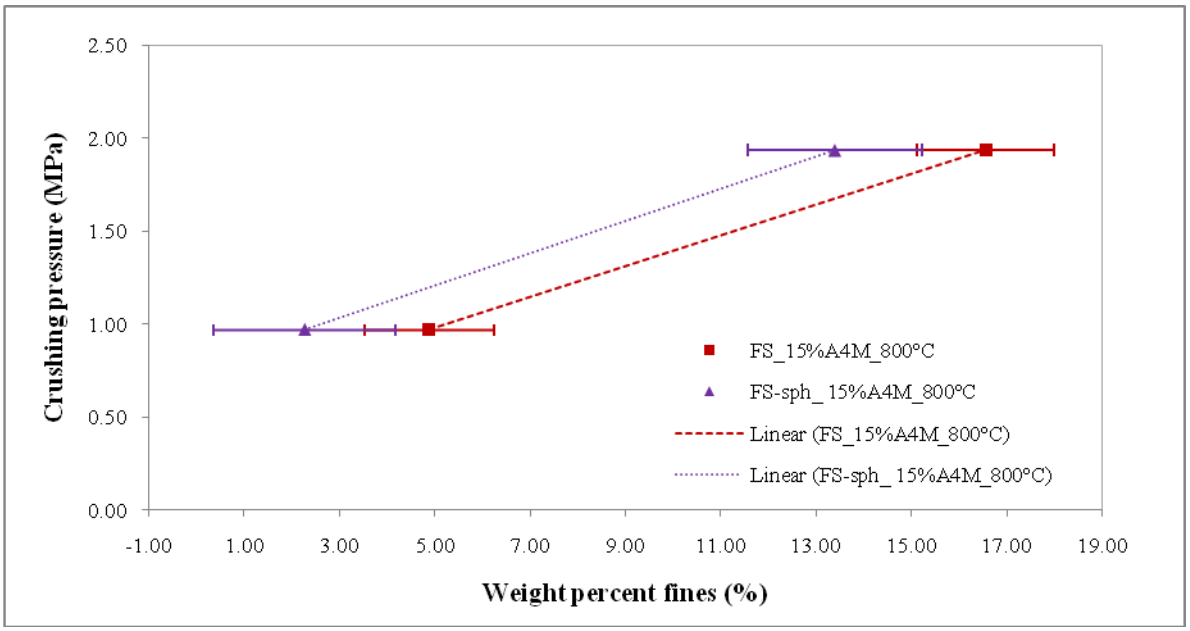

Figure 54: Bulk crushing strength results for cylindrical and spherical fumed silica samples, prepared with 15 % wt of binder and calcined at 800 °C.

In Figure 55, one can notice that the extrudates of SBA-15 show a significant inferior resistance performance compared to zeolite, opposing the single pellet crushing strength test, where the axial crushing stress for SBA-15 extrudate was similar to the crushing stress of zeolite. This could be explained by the fact that the zeolite granules have clay on their composition to increase their strength, as proved in Figure 56. In this graph, green bodies of fumed silica extrudates, prepared with 15 % wt of binder (un-calcinated), show competitive mechanic strength when compared to zeolites. Therefore, it is important to highlight that the presence of binder (inorganic or organic) strongly increases the crush strength of the material. The curves for samples containing binder are more inclined when compared to binder-free fumed silica samples.

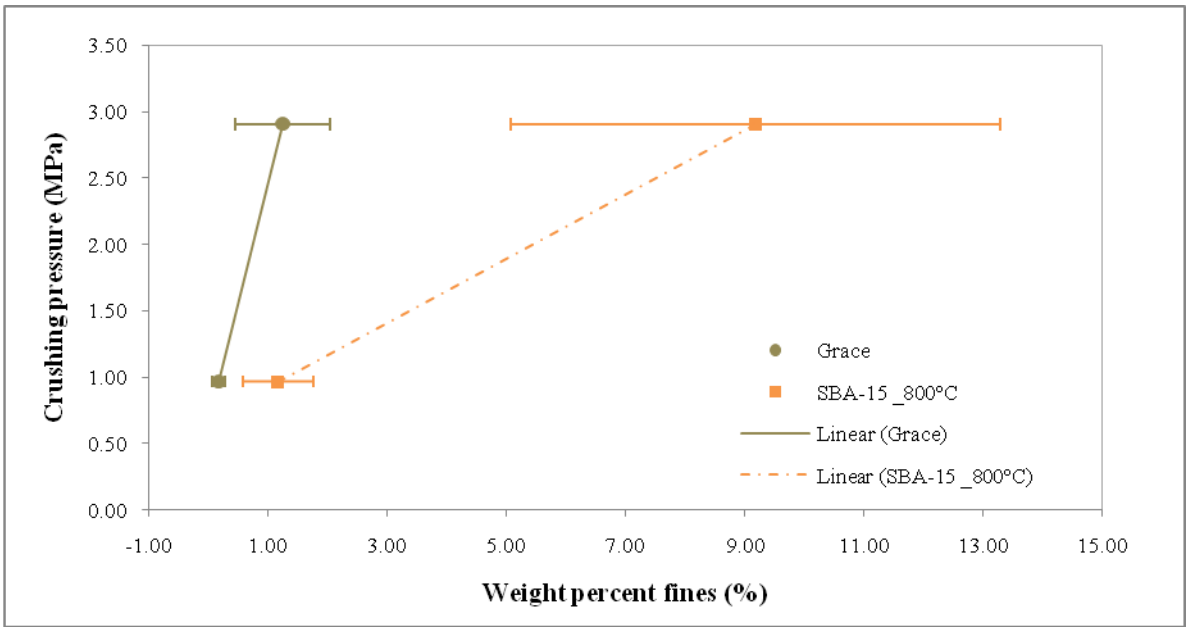

Figure 55: Bulk crushing strength results for commercial zeolite Grace granules and for SBA-15 cylindrical extrudates, prepared with 20 % wt of binder and calcinated at 800 °C.

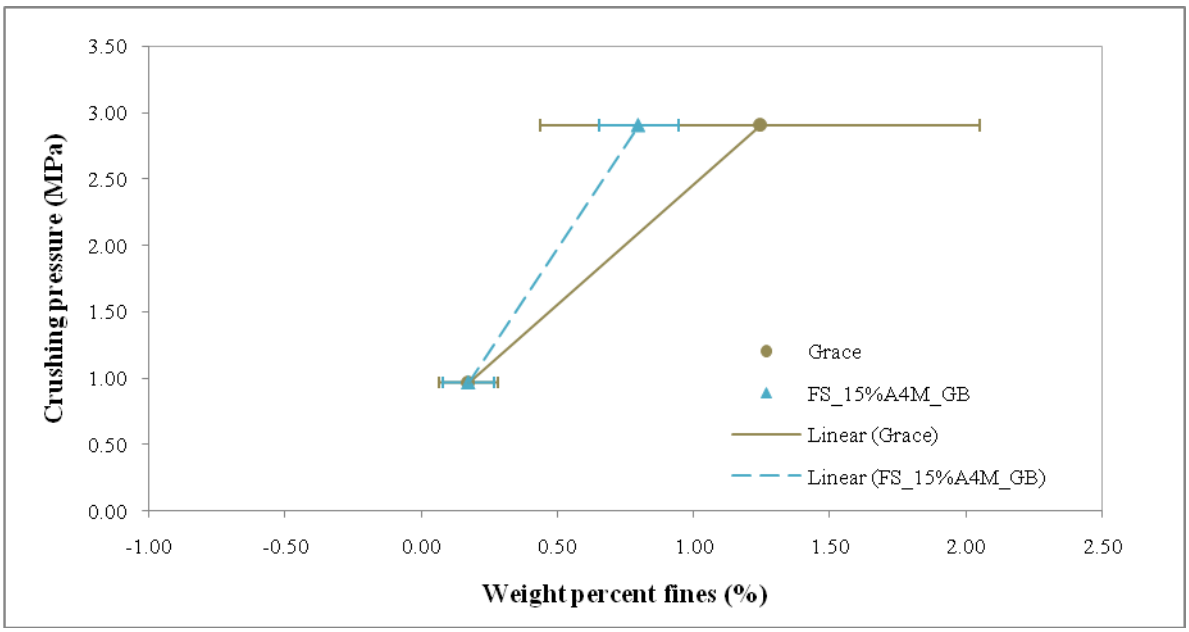

Figure 56: Bulk crushing strength results for commercial zeolite Grace granules and for green body cylindrical fumed silica sample, prepared with 15 % without heat treatment.

5.4. Microtomography images

In other to analyse the presence of internal cracks and purity of the silica granules produced, the extrudates and spheres of fumed silica (prepared with 20 % of methocel and calcinated at 500 and 800 °C) were scanned in the microtomograph. The granule of the commercial zeolite Grace was also scanned to use as reference. The slices generated in the analysis are shown in Figure 57 to Figure 59.

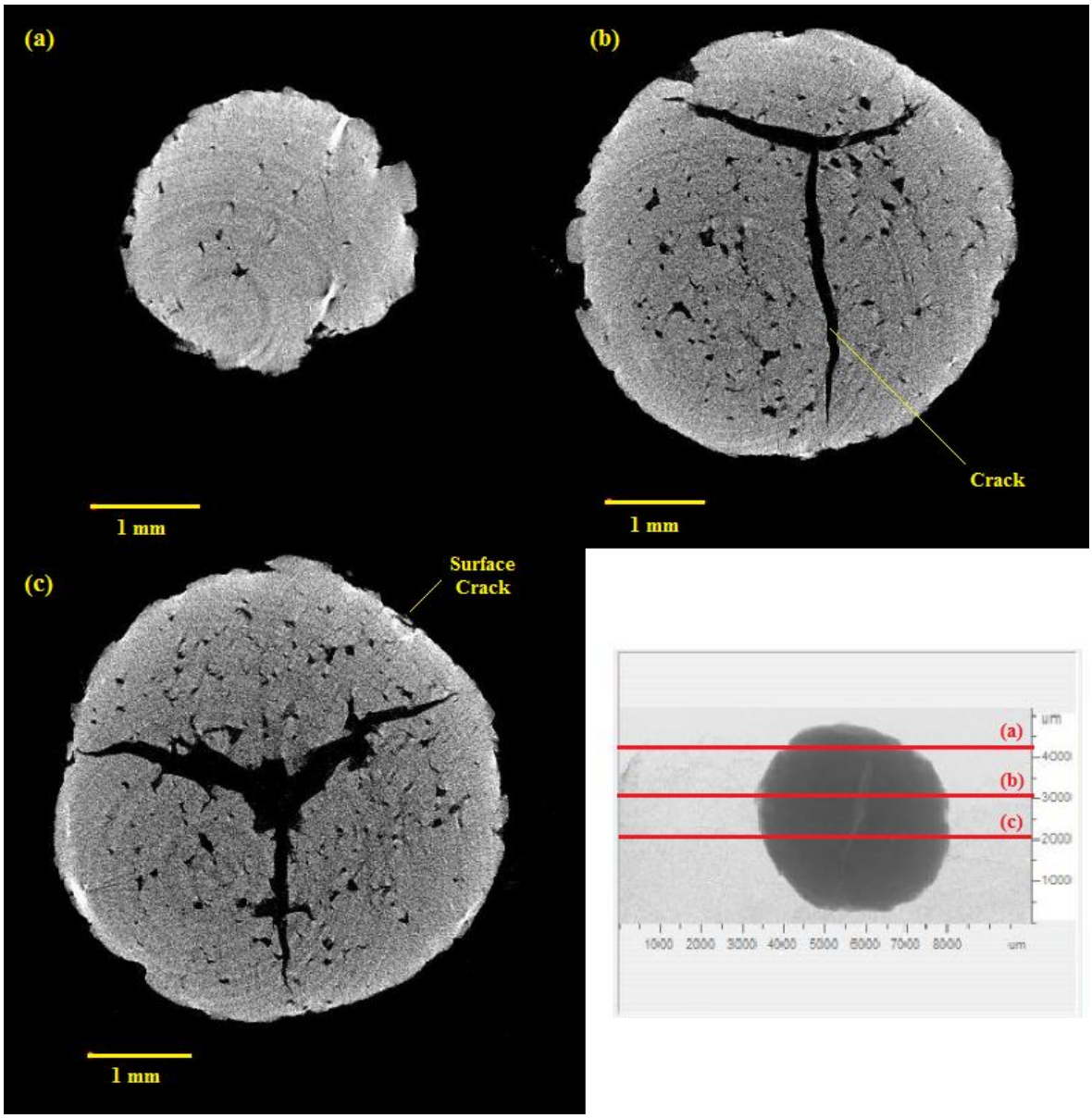

Figure 57: Slices of fumed silica sphere, prepared with 20 % wt of methocel and calcinated at 500 °C, obtained through microtomography. The last image on the bottom right is an X-ray vertical projection upon which are marked the positions of the horizontal slices from (a) to (c)

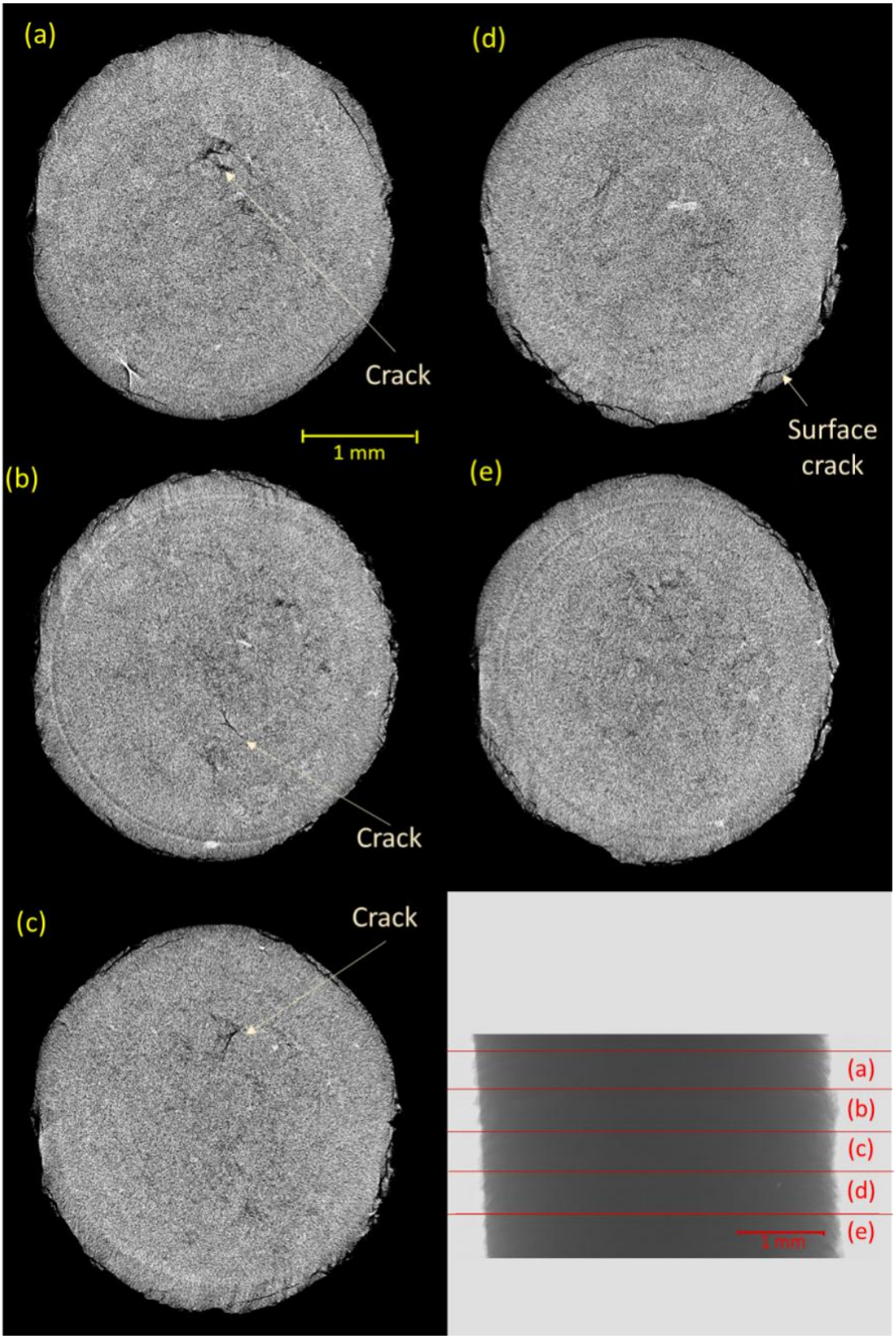

Figure 58: Slices of fumed silica cylindrical extrudate, prepared with 20 % wt of methocel and calcinated at 800 °C, obtained through microtomography. The last image on the bottom right is an X-ray vertical projection upon which are marked the positions of the horizontal slices from (a) to (e).

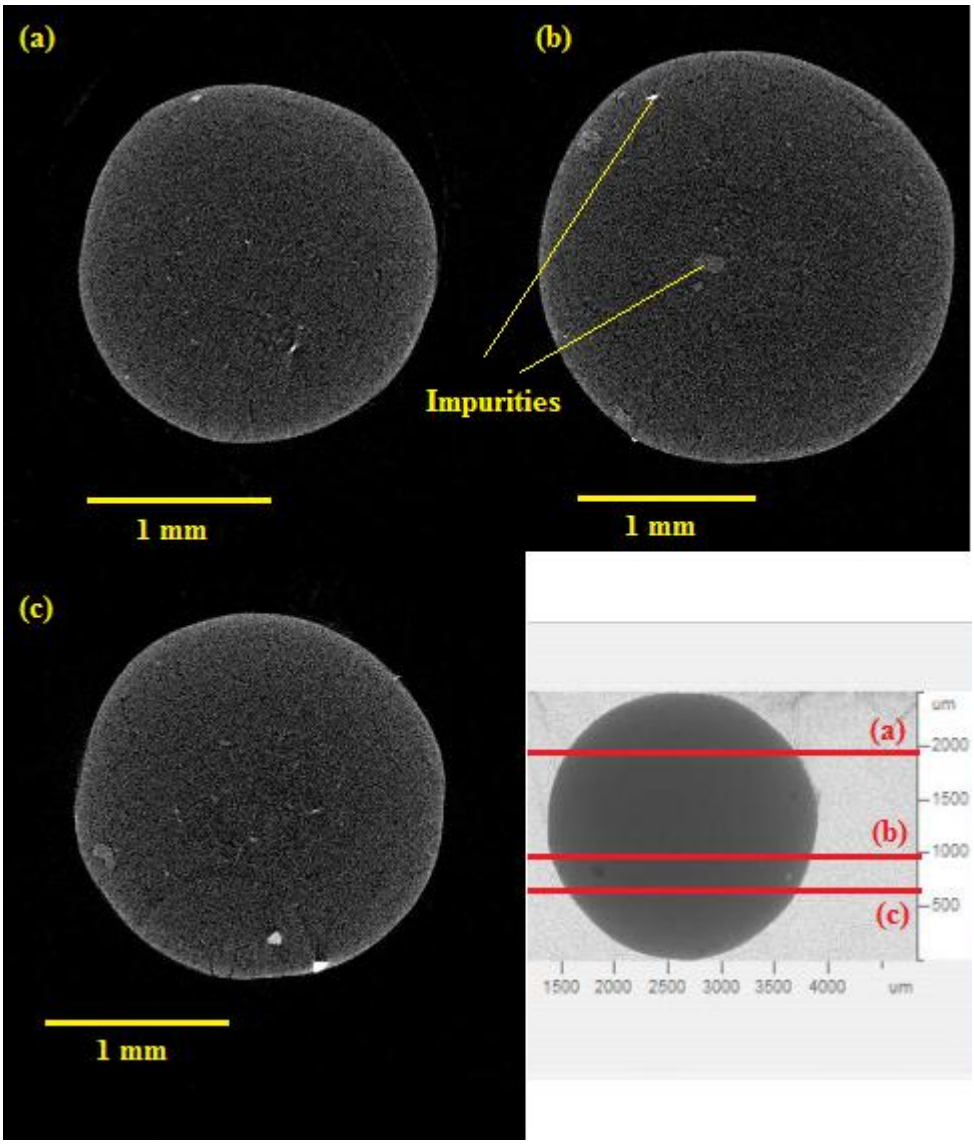

Figure 59: Slices of commercial zeolite Grace granule obtained through microtomography. The last image on the bottom right is an X-ray vertical projection upon which are marked the positions of the horizontal slices from (a) to (c).

To start with, one can observe from the microtomographic images obtained, that no impurities or distinct phases were detected in the images of fumed silica, as found for the commercial zeolite. This was expected, because the organic binder used (methocel) was removed after heat treatment, producing clay-free granules.

The shrinkage, cracks and micro-holes present in the samples were created by the expulsion of water and binder during the drying or the calcination processes.

Concerning the sphere of fumed silica calcinated at 500 °C, cracks of 0.1 – 0.5 mm wide and 4 mm long were detected inside of the granule. The presence of a major crack inside the

material decreases drastically its mechanical strength. One can assume that this crack is probably due to spheronization process, where one small crack grew up with the motion of the plate. This can be proven by the increase of the fracture in radial direction. Major cracks were not detected in the silica fumed cylindrical extrudates, which reinforces the idea that the cracks increased during spheronization process. In addition, for both granules of fumed silica, the presence of cracks on the surface was also observed, indicating that the extrusion process can be improved. The ideal would be to do an extrusion under vacuum, minimizing the probability of the formation of cracks and voids in the final extrudates.

Concerning the commercial zeolite Grace, no significant macro cracks were detected inside of the pellets of fumed silica. However, impurities were found among the material. These impurities are from the clay, which the zeolite was prepared with, and remained in the structure to increase the strength of the material.

These microtomographic results could explain the poor performance of the fumed silica granules produced in this work compared to the commercial zeolite Grace. The lack of clay as binder and cracks inside the granules are responsible for make the fumed silica granules less resistant.

6. CONCLUSIONS AND FINAL REMARKS

In this work, clay-free granules of fumed silica and SBA-15 mesoporous silica were produced. They were analysed using TG, FTIR, Image-J, N2 adsorption, water adsorption, axial and diametrical crushing tests, bulk crush test and microtomograph images. The relationship between the granulation process, geometry, adsorbent capacity and mechanical performance was studied for these materials.

The main outcome of this research is that granules free of impurities of fumed silica and SBA-15 mesoporous silica, in size of millimetres (2 to 4 mm), were successfully produced. This was achieved by the wet granulation procedure, using methocel as organic binder, followed by extrusion or extrusion-spheronization procedures, and then the granules were calcinated for 1h at 800 °C. The extrusion process was improved by enhancing the viscosity of the paste, by increasing the methocel content (15 to 20 % wt). However, the paste became

thicker and harder to extrude, as the water absorption capacity of methocel is high. Hence, it was necessary to evaluate the correct composition of methocel and water, to get a soft paste. This addition of water was the critical step in the extrusion process. The extrusion process has shown to be more successfully than the extrusion-spheronization process, because fewer losses and cracks were generated. The microtomograph image showed a giant crack after the spheronization process, i.e. compromising the integrity and the resistance of the final spheres.

Regards to mechanical strength, all samples calcinated at 800 °C showed higher resistant than the granules calcinated at 500 °C. The axial crushing stress of fumed silica extrudates calcinated at 800 °C was 4.9 ± 1.1 MPa, against 2.4 ± 0.5 MPa at 500 °C. The axial crushing stress of SBA-15 extrudates calcinated at 800 °C was 8.3 ± 2.7 MPa. Even though the axial and diametrical crushing test showed competitive values of crushing stress, the bulk crushing test for the commercial zeolite Grace and un-calcinated fumed silica extrudates (containing 15 % wt of binder over the clay-free silica samples) showed a superior performance than clay-free granules. This is due to the presence of binder (clay or methocel) in the composition.

Regards to sorption capacity, granules and powders of SBA-15 mesoporous silica samples calcinated at 800 °C had a significant decrease in surface area and pore volume. In more detail, the surface area decreased almost by half, i.e. from 757 m^2/g (in SBA-15 powder calcinated at 550 °C) to 386 m^2/g (in SBA-15 powder calcinated at 800 °C, while the pore volume decreased from 0.73 cm^3/g to 0.50 cm^3/g. Regards to SBA-15 granules calcinated at 800 °C, the surface area and pore volume are found to be around 392 m^2/g and 0.53 cm^3/g, respectively. In addition, SBA-15 extrudates showed a narrow distribution pore size, with pore size of 7 nm. These results are explained by the fact that once the samples are calcinated at high temperatures, the number of micropores and the amount of silanol groups on the surface decrease. Moreover, it confirms that the porosity and surface area are strongly depended on the calcination temperature, rather than the granulation process (18). Therefore, the water sorption also decreased in the granules produced. To overcome to this effect, future surface activation, by acid attack for examples, is recommended to increase water sorption capacity.

Finally, the granules produced in this work have high potential to be used as adsorbents and desiccants. Also this work contributes to clay-free granulation producing final pure granules of nanomaterials.

7. REFERENCES

1 Chandrasekar, G.; Hartmann, M.; et al. Preparation of SBA-15 extrudates: Evaluation of textural and mechanical properties. **Journal of Porous Materials**, v. 16, n. 2, p. 175–183, 2009.

2 Dongyuan Zhao, Ying Wan, W.Z. 8 - Mesoporous Nonsilicia Materials. In: **Ordered Mesoporous Materials**. 2013, p. 293–428.

3 Xing, Bao-Lin; Guo, Hui; Chen, L.-J. Lignite-derived high surface area mesoporous activated carbons for electrochemical capacitors. **Fuel Processing Technology**, v. 138, p. 734–742, 2015.

4 Systems, C.P. Oil and Gas Blog. **https://www.croftsystems.net/oil-gas-blog/why-should-you-dehydrate-natural-gas, accessed in 3/Dec/2016.**,

5 Zhao, D.; Huo, Q.; et al. Tri-, Tetra-, and Octablock Copolymer and Nonionic Surfactant Syntheses of Highly Ordered, Hydrothermally Stable, Mesoporous Silica Structures. **J. Am. Chem. Soc.**, v. 120, n. 24, p. 6024–6036, 1998.

6 Ribeiro, J. de O.N. Synthesis, Characterization and Performance Evaluation of Mesoporous Silica Functionalized with Amine for Adsorption of CO2 from Natural Gas. **Master dissertation - Belo Horizonte - UFMG**, p. 1–104, 2016.

7 CHOI, H.; Kim, Y.H.; et al. Granular mesoporous silica and preparation method thereof. **US Patente 20130095025 A1**, p. 1, 2013.

8 Kresge, C.T.; Leonowicz, M.E.; et al. Ordered mesoporous molecular sieves synthesized by a liquid-crystal template mechanism. **Nature**, v. 359, n. 6397, p. 710–712, 1992.

9 Akhtar, F.; Andersson, L.; et al. Structuring adsorbents and catalysts by processing of porous powders. **Journal of the European Ceramic Society**, v. 34, n. 7, p. 1643–1666, 2014.

10 Sing, K.S.W.; Everett, D.H.; et al. Reporting physisorption data for gas / solid systems with special reference to the determination of surface area and porosity (Recommendations 1984). **Pure & Appl. Chem.**, v. 57, n. 4, p. 603–619, 1985.

11 Alothman, Z.A. A Review: Fundamental Aspects of Silicate Mesoporous Materials. **Materials**, v. 5, n. 12, p. 2874–2902, 2012.

12 Avnir, D.; Everett, D.H.; et al. Guidelines for the Characterization of Porous Solids. **Studies in Surface Science and Catalysis**, v. 87, n. 1, p. 1–9, 1994.

13 Horikawa, T.; Do, D.D.; et al. Capillary condensation of adsorbates in porous materials. **Advances in Colloid and Interface Science**, v. 169, n. 1, p. 40–58, 2011.

14 Crossland, E.J.W.; Noel, N.; et al. Mesoporous TiO2 single crystals delivering enhanced mobility and optoelectronic device performance. **Nature**, v. 495, n. 7440, p. 215–9, 2013.

15 Ngamsinlapasathian, S.; Sreethawong, T.; et al. Single- and double-layered mesoporous TiO2/P25 TiO2 electrode for dye-sensitized solar cell. **Solar Energy Materials and Solar**

Cells, v. 86, n. 2, p. 269–282, 2005.

16 Wakefield, G.; Adair, M.; et al. Mesoporous silica nanocomposite antireflective coating for Cu(In,Ga)Se2 thin film solar cells. **Solar Energy Materials and Solar Cells**, v. 134, p. 359–363, 2015.

17 Ariga, K.; Vinu, A.; et al. Nanoarchitectonics for mesoporous materials. **Bulletin of the Chemical Society of Japan**, v. 85, n. 1, p. 1–32, 2012.

18 Yang, P.D.; Zhao, D.Y.; et al. Generalized syntheses of large-pore mesoporous metal oxides with semicrystalline frameworks. **Nature**, v. 396, n. November, p. 6–9, 1998.

19 Ryoo, R.; Joo, S.H.; et al. Ordered Mesoporous Carbons. **Advanced Materials**, v. 13, n. 9, p. 677–681, 2001.

20 Ryoo, R.; Joo, S.H.; et al. 07-O-01 - Ordered mesoporous carbon molecular, sieves by templated synthesis: the structural varieties. **Studies in Surface Science and Catalysis**, v. 135, n. DECEMBER 2001, p. 150–158, 2001.

21 Kruk, M.; Dufour, B.; et al. Synthesis of mesoporous carbons using ordered and disordered mesoporous silica templates and polyacrylonitrile as carbon precursor. **Journal of Physical Chemistry B**, v. 109, n. 19, p. 9216–9225, 2005.

22 Dongyuan Zhao, Ying Wan, W.Z. 2 - Synthesis Approach of Mesoporous Molecular Sieves. In: **Ordered Mesoporous Materials**. Weinheim, Germany: WILEY-VCH Verlag Gmbh & Co, KGaA, 2013, p. 5–51.

23 Berenguer Murcia, Á. Ordered Porous Nanomaterials: The Merit of Small. **ISRN Nanotechnology**, v. 2013, p. 1–29, 2013.

24 Lobo, J.A.C. Heterogeneous asymmetric epoxidation of cis-ethyl cinnamte over Jacobsen's catalyst immobilized in inorganic porous materials. **PHD Thesis - Aachen**, p. 37, 2005.

25 Rhodes, C.J. Properties and applications of zeolites. **Science Progress**, v. 93, n. 3, p. 223–284, 2010.

26 Vaughan, D.E.W. Zeolites and Other Microporous Materials. **Studies in Surface Science and Catalysis**, v. 49, n. C, p. 95–116, 1989.

27 Haag, W.; Lago, R.; et al. The active site of acidic aluminosilicate catalysts. **Nature**, v. 309, n. 30 August 1984, p. 589–591, 1984.

28 Christian Baerlocher, Lynne McCusker, Wei Wan, Xiaodong Zou, C.K. Atlas of zeolite framework types. **http://www.iza-structure.org/databases/Date accessed in 7/Nov/2016**,

29 Flanagan, D.M. U.S. Geological Survey. **Mineral Commodity Summaries, https://www.usgs.gov/ accessed in 7/Nov/2016**,

30 Wünsch, K.G. Zeolites, a really special mineral group. **http://www.mineralien-verkauf.de/zeogallery/zeolithee.html accessed in 07/Nov/2016**,

31 Perot, G.; Guisnet, M. Advantages and disadvantages of zeolites as catalysts in organic chemistry. **Journal of Molecular Catalysis**, v. 61, n. 2, p. 173–196, 1990.

32 Katiyar, A.; Yadav, S.; et al. Synthesis of ordered large pore SBA-15 spherical particles for adsorption of biomolecules. **Journal of Chromatography A**, v. 1122, n. 1–2, p. 13–20, 2006.

33 Jadhav K., Dumbare P., P. V. Mesoporous Silica Nanoparticles (MSN): A Nanonetwork and Hierarchical Structure in Drug Delivery. **Journal of Nanomedicine Research**, v. 2, n. 5, p. 1–8, 2015.

34 Kurdyukov, D.A.; Eurov, D.A.; et al. High-surface area spherical micro-mesoporous silica particles. **Microporous and Mesoporous Materials**, v. 223, p. 225–229, 2016.

35 Kleitz, F. Ordered Mesoporous Materials: Template Removal, Frameworks and Morphology. **Dissertation - Ruhr-Universität Bochum**, p. 1–191, 2002.

36 Lu, H.; Wang, L.; et al. Unusual pH-responsive fluid based on a simple tertiary amine surfactant: the formation of vesicles and wormlike micelles. **RSC Adv.**, v. 4, n. 93, p. 51519–51527, 2014.

37 Chang, F.Y.; Chao, K.J.; et al. Adsorption of CO2 onto amine-grafted mesoporous silicas. **Separation and Purification Technology**, v. 70, n. 1, p. 87–95, 2009.

38 Belmabkhout, Y.; Sayari, A. Effect of pore expansion and amine functionalization of mesoporous silica on CO2 adsorption over a wide range of conditions. **Adsorption**, v. 15, n. 3, p. 318–328, 2009.

39 Rahmat, N.; Abdullah, A.Z.; et al. A review: Mesoporous Santa Barbara amorphous-15, types, synthesis and its applications towards biorefinery production. **American Journal of Applied Sciences**, v. 7, n. 12, p. 1579–1586, 2010.

40 Li, J.; Wang, L.; et al. Different N-containing functional groups modified mesoporous adsorbents for Cr(VI) sequestration: Synthesis, characterization and comparison. **Microporous and Mesoporous Materials**, v. 110, n. 2–3, p. 442–450, 2008.

41 Thielemann, J.; Girgsdies, F.; et al. Pore structure and surface area of silica SBA-15: influence of washing and scale-up. **Beilstein journal of nanotechnology**, v. 2, n. 1, p. 110–118, 2011.

42 Scaramuzzi, K.; Oliveira, D.C.A.; et al. Nanostructured SBA--15 silica as an adjuvant in immunizations which hepatitis B vaccine. **Einstein**, v. 9, p. 436–41, 2011.

43 Voort, P. Van Der; Ravikovitch, P.I.; et al. A new templated ordered structure with combined micro- and mesopores and internal silica nanocapsules. **Journal of Physical Chemistry B**, v. 106, n. 23, p. 5873–5877, 2002.

44 Hiyoshi, N.; Yogo, K.; et al. **Reversible Adsorption of Carbon Dioxide on Amine-Modified SBA-15 from Flue Gas Containing Water Vapor**. Elsevier Masson SAS, 2004.

45 Xunyu Chemical - Professional Silica Fumed Producer. **https://fumed-silica.net/, accessed in 22/Nov/2016**,

46 Katz, H.S., Milewski, J. V. Mineral Fillers. In: **Handbook Of Fillers For Plastics**. New York: VNR, 1988, p. 166–196.

47 EVONIK. **http://www.aerosil.com/product/aerosil/en/products/pages/default.aspx,**

accessed in 29/Nov/2016,

48 Ennis, J.; Litster, B. Principles of size enlargement. **Perry's Chemical Engineer Handbook**, v. 8, p. 21–74, 2008.

49 Litster, J., Ennis, B. The Science and Engineering of Granulation Process. In: **Particle Technology Series**. Dordrecht: Springer-Science+Business Media, 2004, p. 1–258.

50 Köppern Process Technology. **http://www.koeppern-international.com/products/compaction/process-technology/, accessed in 5/Dec/2016.**,

51 Gerteis. **http://www.gerteis.com/en/applications/technology, accessed in 07/Dez/2016**,

52 Iveson, S.M.; Litster, J.D.; et al. Nucleation, growth and breakage phenomena in agitated wet granulation processes: A review. **Powder Technology**, v. 117, n. 1–2, p. 3–39, 2001.

53 Walker, G.M. Chapter 4 Drum Granulation Processes. In: **Handbook of Powder Technology**. Elsevier, 2007, p. 219–254.

54 Mörl, L., Heinrich, S., et al. Chapter 2 Fluidized bed spray granulation. In: **Handbook of Powder Technology**. Elsevier, 2007, p. 21–188.

55 Reynolds, G.K., Le, P.K., et al. Chapter 1 High shear granulation. In: **Handbook of Powder Technology**. Elsevier, 2007, p. 3–19.

56 Vervaet, C.; Baert, L.; et al. Extrusion-spheronisation A literature review. **International Journal of Pharmaceutics**, v. 116, n. 2, p. 131–146, 1995.

57 Wilson, D.I., Rough, S.L. Chapter 3 Extrusion-Spheronisation. In: **Handbook of Powder Technology**. Elsevier, 2007, p. 189–217.

58 Rowe, R.C. Spheronization: a novel pill-making process. **Pharm Int.**, v. 6, p. 119–123, 1985.

59 Baert, L.; Vermeersch, H.; et al. STUDY OF PARAMETERS IMPORTANT IN THE SPHERONIZATION PROCESS. **International Journal of Pharmaceutics**, v. 96, n. 1–3, p. 225–229, 1993.

60 Liew, C.; Chua, S.; et al. Elucidation of spheroid formation with and without the extrusion step. **PharmSciTech**, v. 8, p. E1–E12, 2007.

61 Krueger, C.; Thommes, M.; et al. Spheronisation mechanism of MCC II-based pellets. **Powder Technology**, v. 238, p. 176–187, 2013.

62 Muley, S.; Nandgude, T.; et al. Extrusion-spheronization a promising pelletization technique: In-depth review. **Asian Journal of Pharmaceutical Sciences**, v. 11, n. 6, p. 684–699, 2016.

63 Köster, M.D. Spheronization Process - Particle Kinematics and Pellet Formation Mechanisms. **PhD Dissertation - Düsseldorf**, p. 118, 2012.

64 Soh, J., Sarkar, S., et al. Pelletization Techniques. In: **Encyclopedia of Pharmaceutical Science and Technology**. CRC, 2013, p. 2515–2524.

65 Janney, M. Chapter 6 Plastic forming of ceramics: extrusion and injection moulding. **Ceramic Processing**, p. 174–209, 1995.

66 Dow, Granulation. **https://www.dow.com/en-us/pharma/formulation-technology/granulation accessed in 3/Mar/2018**,

67 Dow, Wet and Dry Granulation Binder. **Granulation Binder - Technical Bulletin**, p. 1–12, 2013.

68 Bogatyrov, V.M.; Borysenko, M.V.; Dubrovin, I.V.; Abramov, M.V.; Galaburda, M.V.; Gorbyk, P.P. Synthesis and Properties of Magnetosensitive Nanocomposites. In: **Nanomaterials and Supramolecular Structures: Physics, Chemistry, and Applications**. 2009, p. 159–168.

69 Almeida, Daniel; Costa, Luelc; Vasconcellos, Luiz; Dias, F. Estudo da remoção do surfactante Pluronic 123 (P123) de organosílicas mesoporosas periódicas (PMOs) por solvente em diferentes condições. **32a Reunião Anual da Sociedade Brasileira de Química**, 2009.

70 Sa, P.; Bs, K.; et al. Formulation and Evaluation of Extended-Release Solid Dispersion of Metformin Hydrochloride. p. 121–129,

71 Preface, S. Infrared Spectroscopy: Fundamentals and Applications. **Analytical Techniques in the Sciences**, p. 71–93, 2004.

72 Kocherbitov, V.; Alfredsson, V. Assessment of Porosities of SBA-15 and MCM-41 Using Water Sorption Calorimetry. **Lanhmuir**, v. 27, p. 3889–3897, 2011.

73 Kocherbitov, V.; Alfredsson, V. Effect of hydration and dehydration on the properties of SBA-15 layer studied by humidity scanning QCM-D. **Microporous and Mesoporous Materials**, v. 230, p. 58–65, 2016.

74 Fakin1, T.; Ristić1, A.; et al. WATER ADSORPTION STUDY ON THE ZEOLITE LTA GRANULES. **Proceedings of the 5 th Serbian-Croatian-Slovenian Symposium on Zeolites**, p. 56–59, 2013.

75 Couroyer, C.; Ghadiri, M.; et al. Methodology for Investigating the Mechanical Strength of Reforming Catalyst Beads. **Oil & Gas Science and Technology**, v. 55, p. 67–85, 2000.

APPENDIX I

Image-J results

- FS-sph_15%A4M_800°C

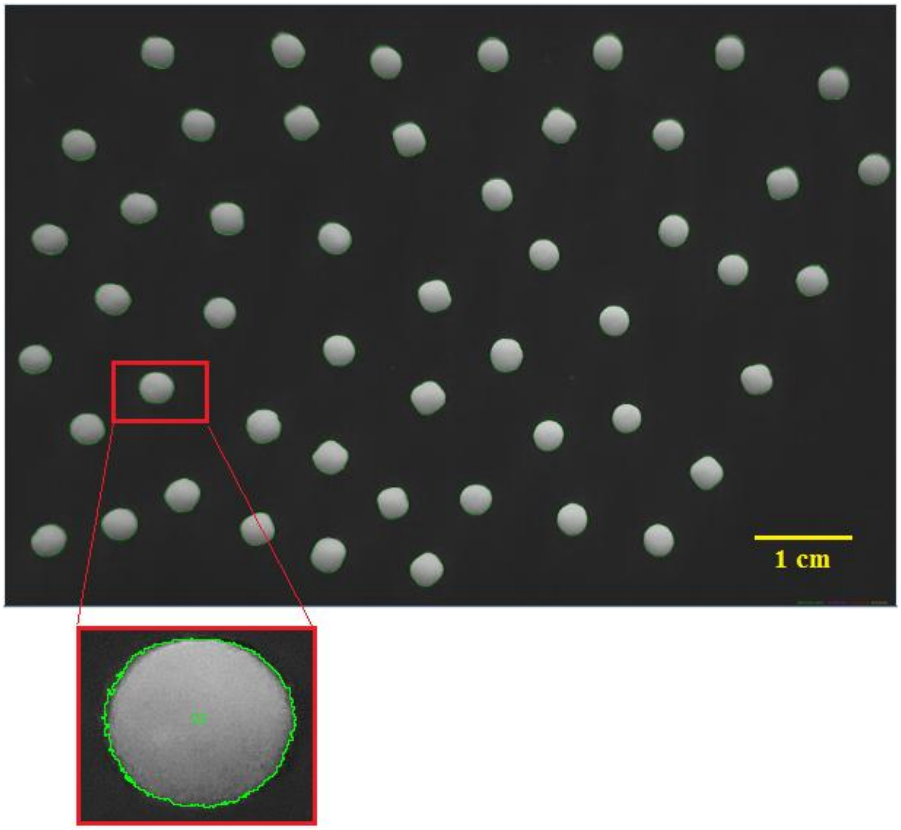

Figure 60: Photo analysed in Image-J software of fumed silica spheres prepared with 15 % of binder and calcinated at 800 °C.

Table 6: Image-J output data for fumed silica spheres prepared with 15 % of binder and calcinated at 800 °C.

#	Round	Diameter (mm)	#	Round	Diameter (mm)	#	Round	Diameter (mm)	#	Round	Diameter (mm)	#	Round	Diameter (mm)
1	0.98	3.08	11	0.94	3.19	21	0.94	3.24	31	0.95	3.32	41	0.99	3.25
2	0.96	3.40	12	0.90	3.17	22	0.94	3.21	32	0.83	3.25	42	0.88	3.40
3	0.98	2.96	13	0.98	3.12	23	0.79	3.30	33	0.94	3.13	43	0.93	3.17
4	0.95	3.10	14	0.94	3.33	24	0.92	3.33	34	0.94	3.18	44	0.98	3.21
5	0.94	3.41	15	0.98	3.37	25	0.95	3.14	35	0.83	2.97	45	0.84	3.34
6	0.95	3.17	16	0.88	3.19	26	0.90	3.26	36	0.94	3.16	46	0.93	3.35
7	0.85	3.30	17	0.97	3.14	27	0.78	3.15	37	0.89	3.31	47	0.93	3.17
8	0.88	3.23	18	0.91	3.31	28	0.93	3.09	38	0.94	3.36	48	0.82	3.27
9	0.91	3.15	19	0.81	3.12	29	0.97	3.11	39	0.98	3.48	49	0.92	3.48
10	0.86	3.17	20	0.93	3.12	30	0.94	3.16	40	0.87	3.25	50	0.95	3.32

- FS-sph_20%A4M_800°C

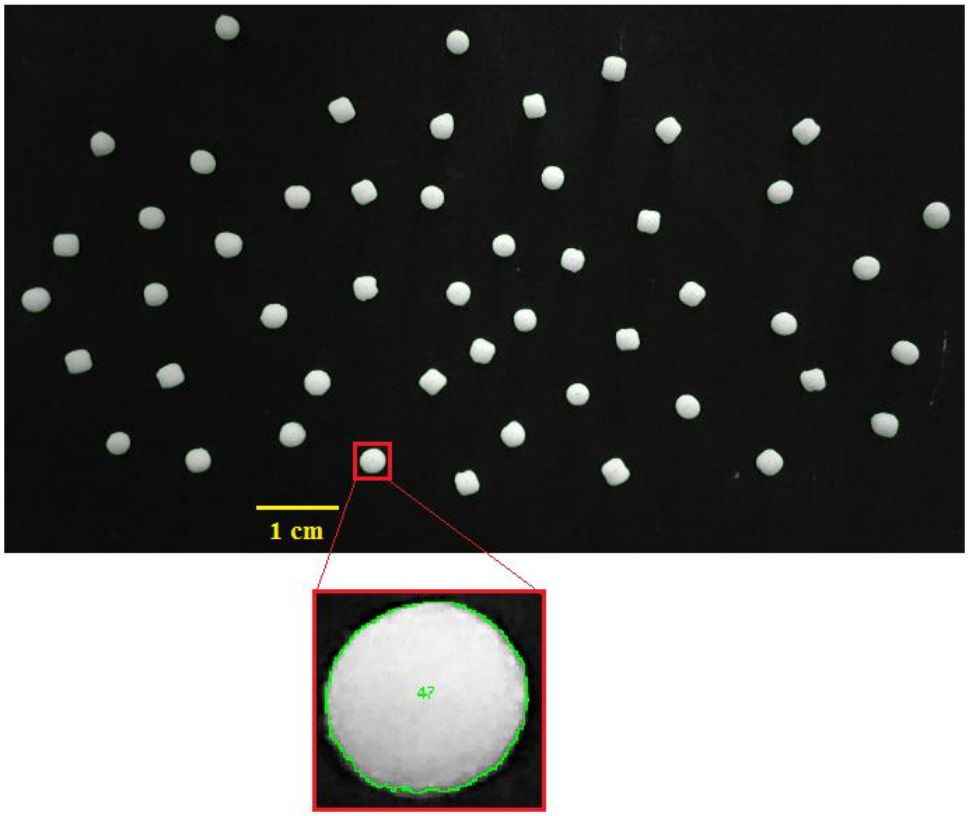

Figure 61: Photo analysed in Image-J software of fumed silica spheres prepared with 20 % of binder and calcinated at 800 °C.

Table 7: Image-J output data for fumed silica spheres prepared with 15 % of binder and calcinated at 800 °C.

#	Round	Diameter (mm)	#	Round	Diameter (mm)	#	Round	Diameter (mm)	#	Round	Diameter (mm)	#	Round	Diameter (mm)
1	0.86	3.25	11	0.95	3.31	21	0.88	3.11	31	0.80	3.33	41	0.88	3.14
2	0.89	3.33	12	0.90	3.17	22	0.96	3.16	32	0.89	3.35	42	0.96	2.96
3	0.96	3.19	13	0.91	3.29	23	0.90	3.46	33	0.98	3.01	43	0.82	3.36
4	0.96	3.07	14	0.93	3.22	24	0.86	3.26	34	0.87	3.20	44	0.92	3.30
5	0.97	2.99	15	0.89	2.93	25	0.98	3.10	35	0.91	3.10	45	0.87	2.93
6	0.95	3.38	16	0.87	3.19	26	0.89	3.32	36	0.98	3.26	46	0.93	3.20
7	0.89	3.18	17	0.94	3.07	27	0.97	3.24	37	0.80	3.27	47	0.94	3.32
8	0.95	3.22	18	0.85	3.17	28	0.98	3.15	38	0.87	3.25	48	0.95	3.36
9	0.91	3.04	19	0.91	3.24	29	0.95	3.22	39	0.86	3.28	49	0.92	3.46
10	0.93	3.04	20	0.98	3.41	30	0.94	3.04	40	0.92	3.24	50	0.93	3.22

- Commercial Zeolite Grace

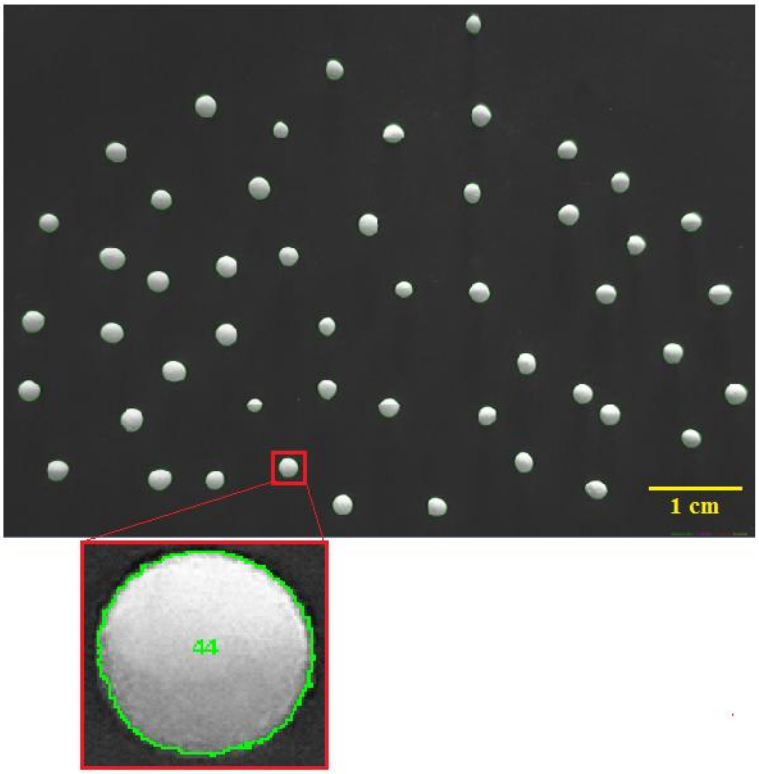

Figure 62: Photo analysed in Image-J software of commercial zeolite Grace.

Table 8: Image-J output data for commercial zeolite Grace.

#	Round	Diameter (mm)	#	Round	Diameter (mm)	#	Round	Diameter (mm)	#	Round	Diameter (mm)	#	Round	Diameter (mm)
1	0.94	2.38	11	0.92	2.12	21	0.95	2.17	31	0.85	2.40	41	0.92	1.73
2	0.96	2.15	12	0.95	2.27	22	0.97	2.18	32	0.92	2.44	42	0.97	2.29
3	0.89	2.38	13	0.94	2.37	23	0.93	2.11	33	0.96	1.98	43	0.91	1.99
4	0.96	2.50	14	0.93	1.83	24	0.88	2.09	34	0.92	2.35	44	0.86	1.94
5	0.87	2.52	15	0.98	2.31	25	0.97	2.18	35	0.92	2.17	45	0.92	2.24
6	0.97	2.27	16	0.94	2.01	26	0.84	2.52	36	0.94	2.29	46	0.91	2.28
7	0.93	2.65	17	0.87	2.19	27	0.96	2.47	37	0.93	2.34	47	0.93	2.46
8	0.99	2.21	18	0.95	2.11	28	0.94	2.27	38	0.88	2.33	48	0.89	2.04
9	0.94	2.14	19	0.93	2.29	29	0.99	1.82	39	0.92	2.18	49	0.86	2.25
10	0.91	1.92	20	0.95	2.07	30	0.92	2.26	40	0.97	2.32	50	0.92	2.10

APPENDIX II

Compression Test

Table 9: Axial Compression Test (Brazilian Test) for extrudates of fumed silica calcinated at 800 °C and 500 °C, and SBA-15 silica calcinated at 800 °C.

SF_20%A4M_800°C

	H1 (mm)	H2 (mm)	D1 (mm)	D2 (mm)	Ḣ (mm)	Ḋ (mm)	F (N)	σ (MPa)
1	3.31	3.31	2.94	2.94	3.31	2.94	33.06	*4.87*
2	3.34	3.27	2.96	2.96	3.31	2.96	33.55	*4.88*
3	3.95	3.93	2.98	2.91	3.94	2.95	23.13	*3.40*
4	3.22	3.22	3.08	3.09	3.22	3.09	42.60	*5.70*
5	3.32	3.36	3.01	2.83	3.34	2.92	41.14	*6.15*
6	5.95	5.92	2.99	2.92	5.94	2.96	28.87	*4.21*
7	3.36	3.30	2.88	2.90	3.33	2.89	36.29	*5.54*
8	3.24	3.22	3.01	3.02	3.23	3.02	21.06	*2.95*
9	3.48	3.46	2.83	2.81	3.47	2.82	27.72	*4.44*
10	3.38	3.35	2.94	2.87	3.37	2.91	24.90	*3.76*

	F (N)	σ (MPa)
SF_20%A4M_800°C	34.70	4.87
Standard deviation	7.35	1.05

$$\sigma = \frac{4F}{\pi D^2}$$

SF_20%A4M_500°C

	H1 (mm)	H2 (mm)	D1 (mm)	D2 (mm)	Ḣ (mm)	Ḋ (mm)	F (N)	σ (MPa)
1	3.75	3.72	2.89	2.91	3.74	2.90	17.61	*2.67*
2	3.98	3.99	3.00	3.05	3.99	3.03	15.10	*2.10*
3	3.70	3.71	3.04	3.05	3.71	3.05	9.76	*1.34*
4	4.17	4.20	3.03	3.05	4.19	3.04	15.32	*2.11*
5	3.65	3.62	3.01	3.05	3.64	3.03	13.33	*1.85*
6	3.77	3.79	3.05	3.09	3.78	3.07	31.78	*4.30*
7	3.97	4.02	3.10	3.13	4.00	3.12	10.51	*1.38*
8	4.04	4.07	3.08	3.06	4.06	3.07	12.14	*1.64*
9	3.67	3.65	3.05	3.05	3.66	3.05	12.62	*1.73*
10	3.65	3.66	3.01	3.09	3.66	3.05	22.16	*3.03*

	F (N)	σ (MPa)
SF_20%A4M_500°C	14.22	2.39
Standard deviation	7.63	0.48

SBA-15_20%A4M_800°C

	H1 (mm)	H2 (mm)	D1 (mm)	D2 (mm)	Ḣ (mm)	Ḋ (mm)	F (N)	σ (MPa)
1	2.94	2.93	2.60	2.63	2.94	2.62	37.48	*6.98*
2	2.70	2.71	2.43	2.49	2.71	2.46	61.31	*12.91*
3	2.72	2.65	2.46	2.49	2.69	2.48	46.61	*9.69*
4	2.62	2.62	2.49	2.54	2.62	2.52	42.82	*8.62*
5	2.80	2.82	2.95	2.83	2.81	2.89	39.55	*6.03*
6	2.94	2.89	2.48	2.52	2.92	2.50	31.69	*6.46*
7	3.40	3.42	2.54	2.58	3.41	2.56	39.79	*7.73*
8	3.21	3.22	2.51	2.54	3.22	2.53	44.69	*8.93*
9	2.55	2.52	2.70	2.62	2.54	2.66	32.33	*5.82*
10	3.39	3.29	2.54	2.56	3.34	2.55	47.34	*9.27*

	F (N)	σ (MPa)
SBA5_20%A4M_800°C	45.55	8.85
Standard deviation	9.46	2.68

Table 10: Diametrical Compression Test (Brazilian Test) for extrudates of fumed silica calcinated at 800 °C and 500 °C, and SBA-15 silica calcinated at 800 °C.

SF_20%A4M_800°C

	H1 (mm)	H2 (mm)	D1 (mm)	D2 (mm)	Ḣ (mm)	Ḋ (mm)	F (N)	σ (MPa)
1	3.47	3.41	2.93	2.92	3.44	2.93	31.36	*1.99*
2	3.29	3.32	2.95	2.92	3.31	2.94	26.07	*1.71*
3	3.89	3.81	2.96	2.94	3.85	2.95	24.61	*1.38*
4	3.83	3.80	3.00	3.02	3.82	3.01	32.73	*1.82*
5	3.39	3.36	2.91	2.93	3.38	2.92	34.37	*2.22*
6	3.30	3.23	2.96	2.97	3.27	2.97	24.12	*1.59*
7	3.64	3.67	2.92	2.97	3.66	2.95	26.20	*1.55*
8	2.90	2.95	2.85	2.74	2.93	2.80	30.88	*2.41*
9	2.59	2.69	2.95	2.93	2.64	2.94	23.46	*1.93*
10	3.07	3.07	2.95	2.92	3.07	2.94	21.61	*1.53*

	F (N)	σ (MPa)
SF_20%A4M_800°C	29.83	1.78
Standard deviation	4.47	0.31

$$\sigma = \frac{2F}{3.14DH}$$

SF_20%A4M_500°C

	H1 (mm)	H2 (mm)	D1 (mm)	D2 (mm)	Ḣ (mm)	Ḋ (mm)	F (N)	σ (MPa)
1	3.93	3.96	3.03	3.06	3.95	3.05	13.86	*0.73*
2	3.92	3.91	3.12	3.06	3.92	3.09	13.77	*0.73*
3	3.90	3.96	3.10	3.05	3.93	3.08	11.12	*0.59*
4	4.12	4.10	3.03	3.01	4.11	3.02	10.46	*0.54*
5	3.68	3.72	3.04	3.04	3.70	3.04	7.95	*0.45*
6	3.65	3.68	3.08	3.05	3.67	3.07	7.33	*0.42*
7	3.88	3.86	3.01	3.06	3.87	3.04	8.56	*0.46*
8	3.61	3.63	3.05	3.15	3.62	3.10	7.42	*0.42*
9	3.62	3.68	3.10	3.08	3.65	3.09	7.90	*0.45*
10	3.66	3.67	2.98	3.03	3.67	3.01	6.22	*0.36*

	F (N)	σ (MPa)
SF_20%A4M_500°C	11.43	0.57
Standard deviation	2.78	0.12

SBA-15_20%A4M_800°C

	H1 (mm)	H2 (mm)	D1 (mm)	D2 (mm)	Ḣ (mm)	Ḋ (mm)	F (N)	σ (MPa)
1	3.74	3.74	2.51	2.51	3.74	2.51	16.18	*1.10*
2	3.50	3.47	2.55	2.60	3.49	2.58	24.70	*1.75*
3	3.79	3.78	2.51	2.56	3.79	2.54	10.13	*0.67*
4	3.21	3.20	2.39	2.48	3.21	2.44	14.46	*1.18*
5	3.73	3.74	2.55	2.44	3.74	2.50	23.42	*1.60*
6	3.06	3.04	2.88	2.85	3.05	2.87	9.78	*0.71*
7	3.38	3.39	2.56	2.55	3.39	2.56	14.90	*1.10*
8	3.50	3.49	2.42	2.44	3.50	2.43	13.57	*1.02*
9	3.31	3.23	2.54	2.54	3.27	2.54	15.69	*1.20*
10	3.23	3.23	2.44	2.46	3.23	2.45	21.65	*1.74*

	F (N)	σ (MPa)
SBA5_20%A4M_800°C	17.78	1.26
Standard deviation	6.16	0.43

Table 11: Compression test for spheres of commercial zeolite Grace.

Commercial zeolite Grace						
	Ḋ (mm)	**F (N)**	**f (MPa)**		**F (N)**	**σ (MPa)**
1	2.00	10.37	2.31	SF_20%A4M_800°C	1.64	1.64
2	2.40	11.79	1.83	Standard deviation	0.49	0.38
3	2.40	13.11	2.03	$\sigma = \frac{2.8F}{3.14D^2}$		
4	2.30	7.99	1.35	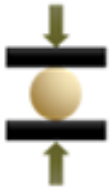		
5	2.30	7.59	1.28			
6	2.30	6.31	1.06			
7	2.30	10.99	1.85			
8	2.40	10.02	1.55			
9	2.30	10.20	1.72			
10	2.20	7.90	1.46			

APPENDIX III

Bulk Crush Strength

Table 12: Bulk crush strength for different samples of fumed silica (made of 15 and 20 % wt of methocel, calcinated at 500 and 800°C), SBA-15 silica calcinated at 800 °C, and commercial zeolite Grace.

	σ (MPa)	Weight percent fines (%)			σ (MPa)	Weight percent fines (%)				
		Grace	SBA-15_20% A4M_800°C	FS_15% A4M_GB		FS_20% A4M_800°C	FS-sph_ 20% A4M_800°C	FS_15% A4M_800°C	FS-sph_15% A4M_800°C	FS_20% A4M_500°C
1	**0.97**	0.15	0.64	0.23	**0.97**	0.62	0.16	3.24	2.28	0.51
2	**0.97**	0.07	1.81	0.07	**0.97**	0.32	0.07	4.25	0.33	0.71
3	**0.97**	0.29	1.05	0.22	**0.97**	4.38	2.45	7.13	4.14	11.89
4	**2.90**	0.33	7.60	0.71	**1.94**	11.78	8.83	15.04	12.91	22.79
5	**2.90**	1.57	13.84	0.72	**1.94**	13.82	9.88	15.91	15.40	27.18
6	**2.90**	1.83	6.10	0.96	**1.94**	10.31	7.04	18.68	11.85	26.03
mean 1	**0.97**	0.17	1.17	0.17	**0.97**	1.77	0.89	4.88	2.25	4.37
mean 2	**2.90**	1.24	9.18	0.80	**1.94**	11.97	8.58	16.54	13.39	25.34
standard deviation 1		0.11	0.59	0.09		2.26	1.35	2.02	1.91	6.52
standard deviation 2		0.80	4.10	0.15		1.76	1.44	1.90	1.82	2.28

F	weight percent fines
PW	weight of fines in pan after sieving
DW	dry weight of sample put into cell
σ (MPa)	crushing pressure

diametro	2.54 cm
raio	1.27 cm
area	5.06 cm²

Load applied	Pressure
50 kgf	0.97 Mpa
100 kgf	1.94 Mpa
150 kgf	2.90 Mpa

Commercial Zeolite Grace

Table 13: BCS calculation for commercial zeolite Grace.

#	Sample	DW (g)	PW (g)	F (%)	σ (MPa)
1	Grace	5.320	0.008	0.15	0.97
2	Grace	5.679	0.004	0.07	0.97
3	Grace	5.275	0.015	0.29	0.97
4	Grace	5.519	0.018	0.33	2.90
5	Grace	5.284	0.083	1.57	2.90
6	Grace	5.245	0.096	1.83	2.90

Mean value	Standard deviation	σ (MPa)	Crush strength for 1% fines generation
0.17	0.11	0.97	2.47 MPa
1.24	0.80	2.90	

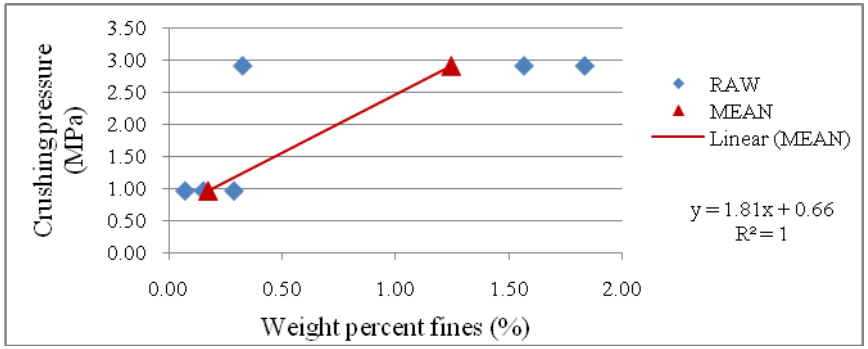

Figure 63: BCS experimental determination for commercial zeolite Grace.

SBA-15_20%A4M_800°C

Table 14: BCS calculation for SBA-15 silica pellets prepared with 20 % of binder and calcinated at 800°C.

#	Sample	DW (g)	PW (g)	F (%)	σ (MPa)
1	SBA-15_20%A4M_800°C	3.121	0.020	0.64	0.97
2	SBA-15_20%A4M_800°C	3.043	0.055	1.81	0.97
3	SBA-15_20%A4M_800°C	3.056	0.032	1.05	0.97
4	SBA-15_20%A4M_800°C	3.013	0.229	7.60	2.90
5	SBA-15_20%A4M_800°C	3.093	0.428	13.84	2.90
6	SBA-15_20%A4M_800°C	2.574	0.157	6.10	2.90

Mean value	Standard deviation	σ (MPa)	Crush strength for 1% fines generation
1.17	0.59	0.97	0.93 MPa
9.18	4.10	2.90	

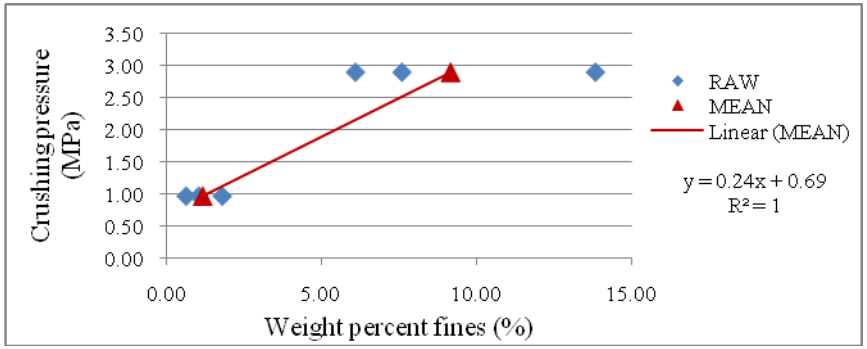

Figure 64: BCS experimental determination for SBA-15 silica pellets prepared with 20 % of binder and calcinated at 800 °C.

FS_20%A4M_800°C

Table 15: BCS calculation for fumed silica pellets prepared with 20 % of binder and calcinated at 800 °C.

#	Sample	DW (g)	PW (g)	F (%)	σ (MPa)
1	FS_20%A4M_800°C	2.712	0.017	0.62	0.97
2	FS_20%A4M_800°C	2.645	0.009	0.32	0.97
3	FS_20%A4M_800°C	2.765	0.121	4.38	0.97
4	FS_20%A4M_800°C	2.794	0.329	11.78	1.94
5	FS_20%A4M_800°C	2.413	0.334	13.82	1.94
6	FS_20%A4M_800°C	2.538	0.262	10.31	1.94

Mean value	Standard deviation	σ (MPa)	Crush strength for 1% fines generation
1.77	2.26	0.97	0.89 MPa
11.97	1.76	2.90	

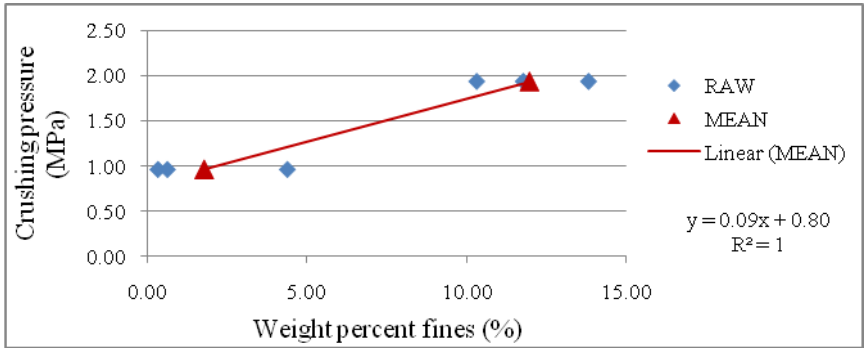

Figure 65: BCS experimental determination of fumed silica pellets prepared with 20 % of binder and calcinated at 800 °C.

FS-sph_20%A4M_800°C

Table 16: BCS calculation for fumed silica spheres prepared with 20 % of binder and calcinated at 800 °C.

#	Sample	DW (g)	PW (g)	F (%)	σ (MPa)
1	FS-sph_20%A4M_800°C	2.735	0.004	0.16	0.97
2	FS-sph_20%A4M_800°C	2.660	0.002	0.07	0.97
3	FS-sph_20%A4M_800°C	2.651	0.065	2.45	0.97
4	FS-sph_20%A4M_800°C	2.729	0.241	8.83	1.94
5	FS-sph_20%A4M_800°C	2.762	0.273	9.88	1.94
6	FS-sph_20%A4M_800°C	2.820	0.199	7.04	1.94

Mean value	Standard deviation	σ (MPa)	Crush strength for 1% fines generation
0.89	1.35	0.97	0.99 MPa
8.58	1.44	2.90	

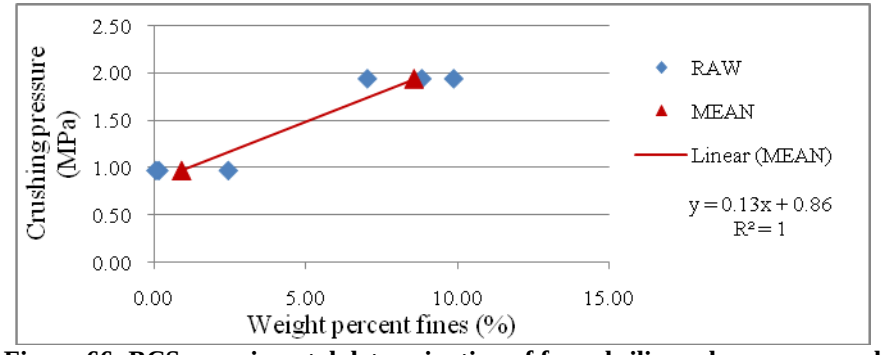

Figure 66: BCS experimental determination of fumed silica spheres prepared with 20 % of binder and calcinated at 800 °C.

FS_15%A4M_800°C

Table 17: BCS calculation for fumed silica pellets prepared with 15 % of binder and calcinated at 800 °C.

#	Sample	DW (g)	PW (g)	F (%)	σ (MPa)
1	FS_15%A4M_800°C	2.580	0.084	3.24	0.97
2	FS_15%A4M_800°C	2.577	0.110	4.25	0.97
3	FS_15%A4M_800°C	2.510	0.179	7.13	0.97
4	FS_15%A4M_800°C	2.567	0.386	15.04	1.94
5	FS_15%A4M_800°C	2.534	0.403	15.91	1.94
6	FS_15%A4M_800°C	2.499	0.467	18.68	1.94

Mean value	Standard deviation	σ (MPa)	Crush strength for 1% fines generation
4.88	2.02	0.97	0.64 MPa
16.54	1.90	2.90	

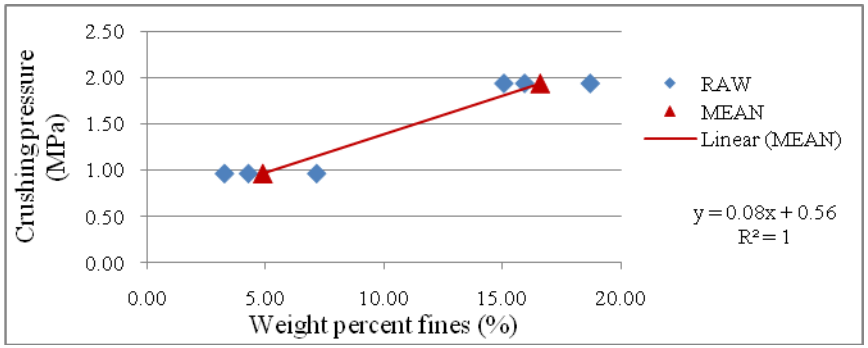

Figure 67: BCS experimental determination of fumed silica pellets prepared with 15 % of binder and calcinated at 800 °C.

FS-sph_15%A4M_800°C

Table 18: BCS calculation for fumed silica spheres prepared with 15 % of binder and calcinated at 800 °C.

#	Sample	DW (g)	PW (g)	F (%)	σ (MPa)
1	FS-sph_15%A4M_800°C	2.836	0.065	2.28	0.97
2	FS-sph_15%A4M_800°C	2.603	0.009	0.33	0.97
3	FS-sph_15%A4M_800°C	2.656	0.110	4.14	0.97
4	FS-sph_15%A4M_800°C	2.594	0.335	12.91	1.94
5	FS-sph_15%A4M_800°C	2.829	0.436	15.40	1.94
6	FS-sph_15%A4M_800°C	2.706	0.321	11.85	1.94

Mean value	Standard deviation	σ (MPa)	Crush strength for 1% fines generation
2.25	1.91	0.97	0.86 MPa
13.39	1.82	2.90	

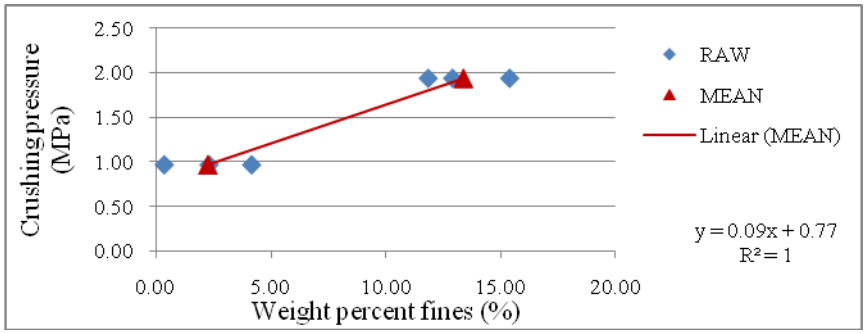

Figure 68: BCS experimental determination of fumed silica spheres prepared with 15 % of binder and calcinated at 800 °C.

FS_20%A4M_500°C

Table 19: BCS calculation for fumed silica pellets prepared with 20 % of binder and calcinated at 500 °C.

#	Sample	DW (g)	PW (g)	F (%)	σ (MPa)
1	FS_20%A4M_500°C	2.454	0.012	0.51	0.97
2	FS_20%A4M_500°C	2.370	0.017	0.71	0.97
3	FS_20%A4M_500°C	2.279	0.271	11.89	0.97
4	FS_20%A4M_500°C	2.396	0.546	22.79	1.94
5	FS_20%A4M_500°C	2.484	0.675	27.18	1.94
6	FS_20%A4M_500°C	2.355	0.613	26.03	1.94

Mean value	Standard deviation	σ (MPa)	Crush strength for 1% fines generation
4.37	6.52	0.97	0.82 MPa
25.34	2.28	2.90	

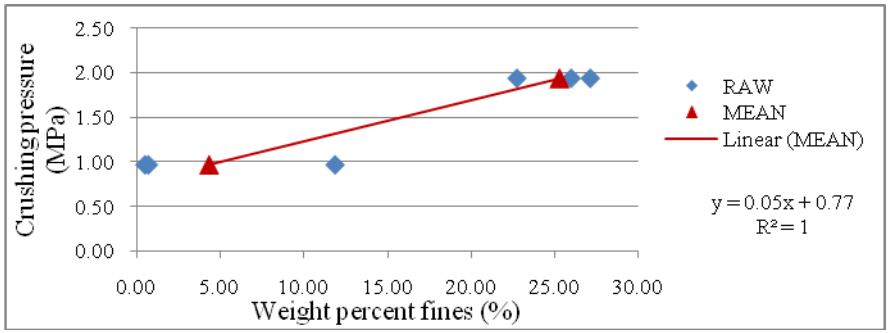

Figure 69: BCS experimental determination of fumed silica pellets prepared with 20 % of binder and calcinated at 500 °C.

FS_15%A4M_GB

Table 20: BCS calculation for green bodies of fumed silica pellets prepared with 15 % of binder.

#	Sample	DW (g)	PW (g)	F (%)	σ (MPa)
1	SF_15%A4M_GB	2.679	0.0062	0.23	0.97
2	SF_15%A4M_GB	2.5988	0.0017	0.07	0.97
3	SF_15%A4M_GB	2.746	0.006	0.22	0.97
4	SF_15%A4M_GB	2.688	0.019	0.71	2.90
5	SF_15%A4M_GB	2.7466	0.0197	0.72	2.90
6	SF_15%A4M_GB	2.6543	0.0256	0.96	2.90

Mean value	Standard deviation	σ (MPa)	Crush strength for 1% fines generation
0.17	0.09	0.97	3.54 MPa
0.80	0.15	2.90	

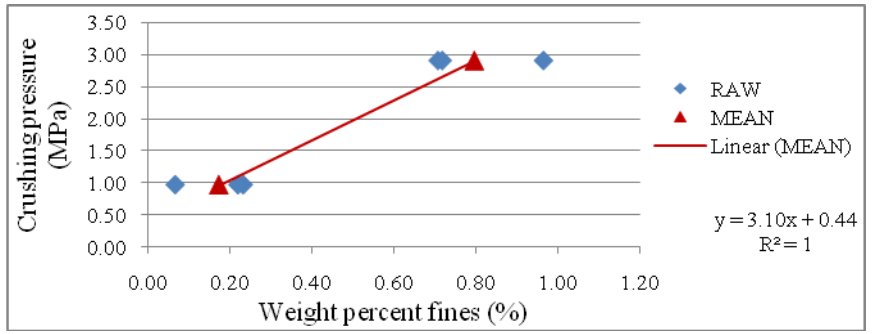

Figure 70: BCS experimental determination of green bodies of fumed silica pellets prepared with 15 %.